

NUREG/CR-4390

SAND85-1967


R3

Printed October 1985

DCC-1/DCC-2 Degraded Core Coolability Analysis

A. W. Reed, K. R. Boldt, E. D. Gorham-Bergeron,
R. J. Lipinski, T. R. Schmidt

Prepared by
Sandia National Laboratories
Albuquerque, New Mexico 87185 and Livermore, California 94550
for the United States Department of Energy
under Contract DE-AC04-76DP00789



8602260121 851031
PDR NUREG
CR-4390 R PDR

Prepared for
U. S. NUCLEAR REGULATORY COMMISSION

SF2900Q(8-81)

NOTICE

This report was prepared as an account of work sponsored by an agency of the United States Government. Neither the United States Government nor any agency thereof, or any of their employees, makes any warranty, expressed or implied, or assumes any legal liability or responsibility for any third party's use, or the results of such use, of any information, apparatus product or process disclosed in this report, or represents that its use by such third party would not infringe privately owned rights.

Available from
GPO Sales Program
Division of Technical Information and Document Control
U.S. Nuclear Regulatory Commission
Washington, D.C. 20555
and
National Technical Information Service
Springfield, Virginia 22161

NUREG/CR-4390
SAND85-1967
E3

DCC-1/DCC-2 DEGRADED CORE COOLABILITY ANALYSIS

A. W. Reed, K. R. Boldt, E. D. Gorham-Bergeron
R. J. Lipinski, T. R. Schmidt

October 1985

Sandia National Laboratories
Albuquerque, NM 87185
Operated by
Sandia Corporation
for the
U.S. Department of Energy

Prepared for
Division of Accident Evaluation, Fuel Systems Research Branch
Office of Nuclear Regulatory Research
U. S. Nuclear Regulatory Commission
Washington, DC 20555
Under Memorandum of Understanding DOE 40-550-75
NRC FIN NO. A-1340

ABSTRACT

The DCC-1 and DCC-2 experiments have provided the first data on dryout and quench behavior of internally heated UO_2 debris in water. The pressure range of this data extends from 1 to 170 atmospheres. Both of the experiments used the Annular Core Research Reactor (ACRR) at Sandia National Laboratories to simulate the effects of radioactive decay heating.

The debris in DCC-1 ranged from 75 microns to in excess of 10 mm in diameter, with a mean diameter of 0.75 mm. The bed depth was 0.5 m and the porosity was 0.345. Dryout heat fluxes ranged from about 41 kW/m^2 (0.012 W/g) at a saturation temperature of 100°C to about 69 kW/m^2 (0.021 W/g) at 340°C . This measured pressure dependence is a factor of two to three lower than predicted by the analytical models. This is believed to be due to the breadth of the debris distribution, but the evidence is inconclusive. Quenches of dried debris took hours to complete. Quench fronts progressed uniformly without the liquid fingers observed in large particle tests.

The debris distribution in DCC-2 was much narrower than in DCC 1, with the majority of particles having diameters between 0.5 and 8 mm. A small amount of "fines" with diameters down to 75 microns was added to the mixture. In DCC-2, thermally stable local dry zones were observed at bed powers below the conventional dryout point. These are believed to be caused by the concentration of fines creating a low permeability zone. Data on global dryout, in which the bed bottom can dry out, agree well with analytical predictions. Quenches of dry zones took about 10 minutes to complete. The quench fronts were not uniform, having a liquid finger which penetrated to the bottom of the bed before the quench was complete.

TABLE OF CONTENTS

	<u>Page</u>
1. INTRODUCTION	1
2. DCC-2 EXPERIMENT DESCRIPTION AND ASSEMBLY	4
2.1 Primary Thermocouples	7
2.2 Fuel Loading	7
2.3 Hot Maximum Allowable Working Pressure (MAWP) Test	12
2.4 Water Loading	12
2.5 Out-of-Pile Systems Tests (OPST) and In-Pile Systems	13
3. PRESENTATION OF DATA	14
3.1 DCC-1 Experiment	14
3.2 DCC-2 Experiment	25
4. ANALYSIS	40
4.1 Bed Power Calibration	40
4.2 Effect of Saturation-Dependent Power Generation on Bed	44
4.3 Data Reduction	52
4.4 DCC-1 Dryout Data	55
4.5 DCC-2 Dryout Data	66
4.6 Error Analysis	67
4.6.1 Drift in Saturation Temperature	68
4.6.2 Saturation Prediction	69
5. QUENCH BEHAVIOR	77
6. CONCLUSIONS	79
7. REFERENCES	81
APPENDIX	83
TABLE A1	84
TABLE A2	92

LIST OF FIGURES

<u>Figure</u>	<u>Page</u>
1.1 Debris Bed Flow Regimes	2
2.1 DCC Experiment Package	5
2.2 DCC Auxiliary Systems	6
2.3 Assembly Procedure Summary for the DCC-2 Experiment	8
2.4 DCC-1 Thermocouple Locations	9
2.5 DCC-2 Thermocouple Locations	10
2.6 DCC Particle Distributions	11
3.1 DCC-1 Dryout #1, $T_{sat} = 100^{\circ}\text{C}$ (Incipient)	15
3.2 DCC-1 Dryout #2, $T_{sat} = 101^{\circ}\text{C}$ (Incipient)	16
3.3 DCC-1 Dryout #5, $T_{sat} = 122^{\circ}\text{C}$ (Incipient)	17
3.4 DCC-1 Dryout #6, $T_{sat} = 141^{\circ}\text{C}$ (Incipient)	18
3.5 DCC-1 Dryout #9, $T_{sat} = 202^{\circ}\text{C}$ (Incipient)	19
3.6 DCC-1 Dryout #18, $T_{sat} = 353^{\circ}\text{C}$ (Incipient)	20
3.7 DCC-1 Dryout #35, $T_{sat} = 142^{\circ}\text{C}$ (Forced and Extended)	22
3.8 DCC-1 Dryout #41, $T_{sat} = 222^{\circ}\text{C}$ (Forced and Extended)	23
3.9 DCC-1 Dryout #42, $T_{sat} = 141^{\circ}\text{C}$ (Incipient and Extended)	24
3.10 DCC-2 Dryouts #7 & 8, $T_{sat} = 200, 219^{\circ}\text{C}$ (Local and Global)	26
3.11 DCC-2 Dryout #22, $T_{sat} = 341^{\circ}\text{C}$ (Local)	28
3.12 Location and Extent of Dryout #22 (DCC-2)	29

LIST OF FIGURES (cont'd)

<u>Figure</u>	<u>Page</u>
3.13 DCC-2 Local Dry Zones	30
3.14 DCC-2 Dryouts #53/54, $T_{sat} = 321^{\circ}\text{C}$ (Global/Local)	33
3.15 DCC-2 Dryouts #63/64, $T_{sat} = 222/221^{\circ}\text{C}$ (Local/Global)	34
3.16 DCC-2 Dryouts #67/68, $T_{sat} = 343^{\circ}\text{C}$ (Local/Global)	35
3.17 DCC-2 Natural Convection Experiment	36
3.18 DCC-2 Dryout #70, $T_{sat} = 158^{\circ}\text{C}$ (Extended Global & Quench)	37
3.19 DCC-2 Dryout #71, $T_{sat} = 148^{\circ}\text{C}$ (Extended Global & Quench)	38
3.20 DCC-2 Dryout #72, $T_{sat} = 185^{\circ}\text{C}$ (Extended Global & Quench)	39
4.1 Predicted Saturation Profiles for DCC-2 at 100°C : Flat Power Profile	45
4.2 Predicted Saturation Profiles for DCC-2 at 100°C : DCC-2 Power Profile	49
4.3 Predicted Saturation Profiles for DCC-1 at 100°C : Flat Power Profile	50
4.4 Predicted Saturation Profiles for DCC-1 at 100°C : DCC-1 Power Profile	51
4.5 Non-dimensional Bed Power Calibration at 100°C	53
4.6 Comparison of DCC-1 Dryout Data with Predictive Models	57
4.7 Non-dimensional Capillary Pressure for Narrow Size Distributions	59

LIST OF FIGURES (cont'd)

<u>Figure</u>		<u>Page</u>
4.8	Non-dimensional Capillary Pressure for DCC-1 Bed	61
4.9	DCC-1 Laminar Relative Permeabilities	63
4.10	DCC-1 Turbulent Relative Permeabilities	64
4.11	Comparison of DCC-1 Dryout Data with Modified Lipinski Model	65
4.12	Comparison of DCC-2 Dryout Data with Predictive Models	67

LIST OF TABLES

<u>Table</u>	<u>Page</u>
4.1 Predicted and Measured Specific Generation for the Saturated DCC-1 Debris Bed	41
4.2 Saturation Dependence of Bed Power	43
4.3 DCC-1 Predictions	46
4.4 DCC-2 Predictions	47
4.5 Reduced DCC-1 Incipient Dryout Powers	56
4.6 Reduced DCC-2 Incipient Global Dryout Powers	68
4.7 DCC-1 Drift Rates	70
4.8 DCC-2 Post-Disruption Drift Rates	71
4.9 DCC-1 Bed Dryout Heat Flux Bounds Based on $S = 0,1$	72
4.10 DCC-2 Bed Dryout Heat Flux Bounds Based on $S = 0,1$	73
4.11 Power Ratios for DCC-1 Configuration	74
4.12 Power Ratios for DCC-2 Configuration	74
4.13 DCC-1 Bed Dryout Heat Flux Bounds Based on $S = 0.2, 0.8$	* 75
4.14 DCC-2 Bed Dryout Heat Flux Bounds Based on $S = 0.2, 0.8$	76
5.1 DCC-1 Quench Cooling Rates	77
5.2 DCC-2 Quench Cooling Rates	78

NOMENCLATURE

SYMBOLS

C	Heat Capacity	[J/kg-K]
DO	Dryout	
F	Dimensionless specific energy generation	
h	Enthalpy	[J/kg]
J	Levrett J function	
k	Laminar permeability	[m ²]
L	Length	[m]
M	Mass	[kg]
P	Power	[W]
p	Pressure	[Pa]
Q	Bed heat flux	[W/m ²]
q	Specific energy generation	[W/g _{fuel} /kW _{reactor}]
S	Saturation	
s	Entropy	[J/kg-K]
T	Temperature	[K]
x	Distance	[m]

GREEK

β	Fitting constants	
κ	Turbulent permeability	[m]
ρ	Density	[kg/m ³]
ψ	Steam quality	

SUBSCRIPTS

b	Breakthrough
c	Capillary
corr	Corrected
d	Drift
DO	Dryout
eff	Effective
exp	Experimental
l	Liquid
pred	Predicted
s	Solid
v	Vapor
w	Water
•	Time Differential
-	Spatial Average

1. INTRODUCTION

Since the accident at Three Mile Island (TMI-2), there has been increased interest in nuclear accidents involving severely damaged fuel in water reactors. However, the study of damaged fuel has been of interest to the fast reactor community since about 1971.^[1] Over this period of time, a large amount of data on the coolability of particulate fuel has been generated. The majority of the data was acquired using bench scale apparatus, simulant materials, and simulant heating techniques. These simulant experiments have been supplemented by a small number of in-pile coolability experiments using prototypic materials.

The obvious approach to the problem of LWR debris coolability is to apply the models developed for the liquid metal fast breeder reactor (LMFBR) coolability program. As in the LMFBR program, it is necessary to generate benchmark data for the coolability of water/uranium debris beds using prototypic materials. The Sandia Laboratories LWR Degraded Core Coolability (DCC) experiments, part of the USNRC's integrated Severe Fuel Damage Research Program, are designed to provide this benchmark data. In addition, the three DCC experiments are designed to examine the effect of parameters which are more typical of LWR debris than LMFBR debris.^[2]

DCC-1 was designed to look at boiling in deep beds with a broad particle size distribution. The diameter range extends from about 0.075 mm to 12 mm, with an average particle diameter (Fair-Hatch^[3]) of 0.310 mm. This size might be expected from an energetic reaction.^[2] The bed depth was 0.5 m. The pressure range of the experiment was from 0.1 MPa to 17 MPa. Dryout powers in DCC-1 corresponded to the laminar flow regime (Fig. 1.1).

DCC-2 was designed to examine boiling in deep beds with larger particles. The size distribution was fairly narrow, with the predominant range being between 1.0 and 8.0 mm. Added to this was a small amount of "fines" in the range of 0.075 to 1.0 mm. The average particle diameter (Fair-Hatch) was 1.42 mm and the bed height is 0.5 m. The planned pressure range of the experiment was from 0.1 MPa to 17 MPa. Dryout powers in DCC-2 corresponded to the transition regime between laminar and "turbulent" flow.

This report presents the analysis of the DCC-1/DCC-2 data. Several new facets of debris coolability have been discovered through these experiments. In DCC-1, the data on dryout did not follow the original predictions of pressure dependence. This led to measurements of capillary pressure in UO₂/water beds,

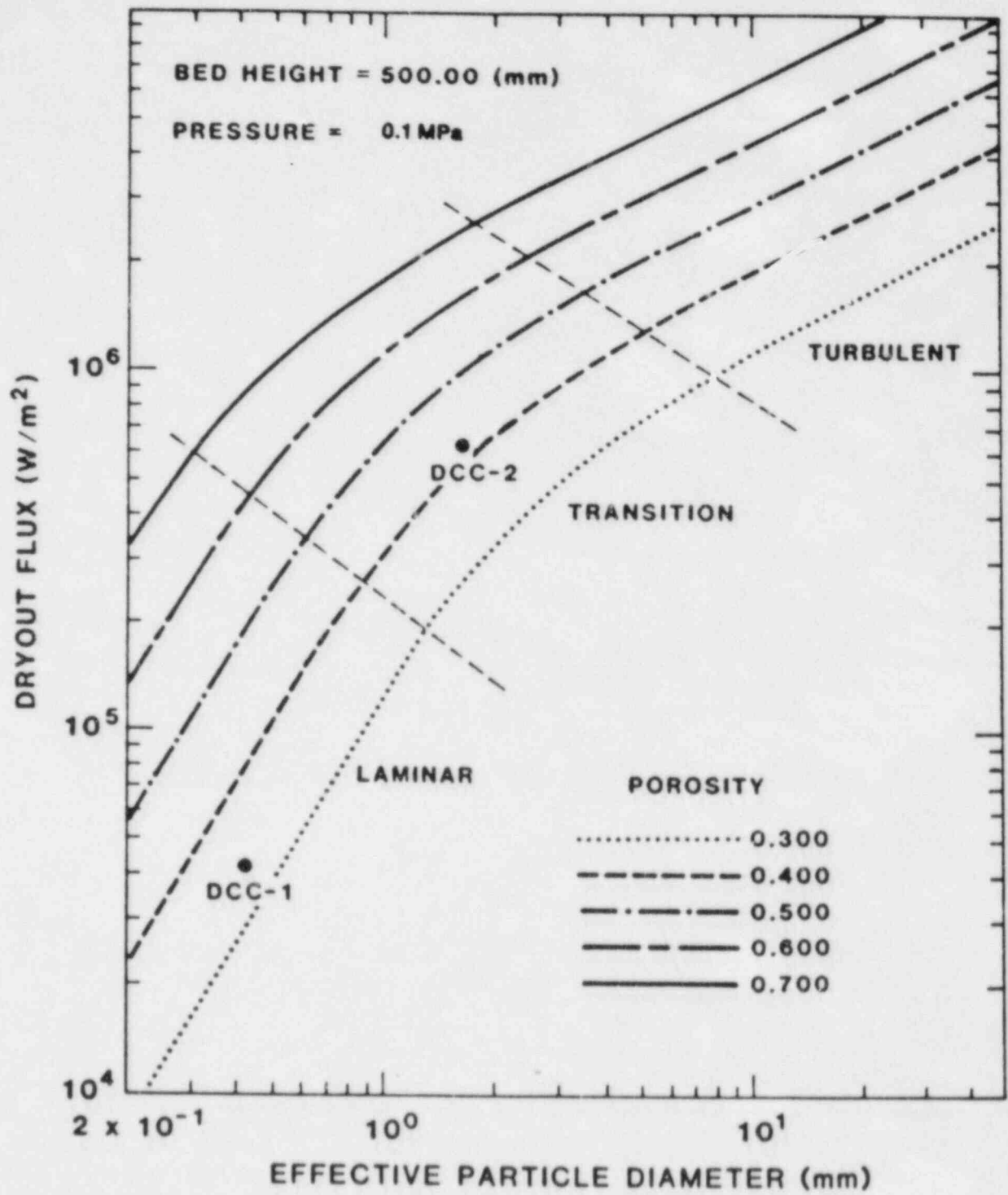


Figure 1.1 Debris Bed Flow Regimes

where it was discovered that beds with broad particle size distributions behaved differently than those with narrow distributions. From a measurement of capillary pressure on a DCC-1 UO₂ bed, and using the method of Brooks and Corey, [4,5] new relative permeabilities were derived for DCC-1. Use of these new properties in the Lipinski model [6] yields predictions of lower pressure dependence. The quench times for DCC-1 are hours long. This suggests that such a bed might be impossible to cool by flooding if formed in a dry state.

In DCC-2, a new phenomenon, "local" dryout, was observed in addition to the anticipated "global" dryouts. Local dryout is characterized by a thermally stable local dry zone surrounded by a boiling zone. This behavior is believed to have been caused by a zone of low permeability formed by the relocation and concentration of small particles at the time of bed construction. Zones of varying permeability are expected to be characteristic of debris formed during reactor accidents. Disruptions of the bed were successful in modifying this zone, but not in eliminating it. Post-disruption data on global dryout are in good agreement with the Lipinski model, displaying the predicted pressure dependence and approximate magnitude. Post-disruption local dryouts display the same predicted pressure dependence. The quench times for DCC-2 are only minutes long, indicating a capability for reflood not observed in DCC-1.

2. DCC-2 EXPERIMENT DESCRIPTION AND ASSEMBLY

The DCC-1 and DCC-2 experiment packages (Fig. 2.1) are nearly identical. The debris bed consists of coarse UO_2 particulate seeded with Gd_2O_3 to decrease thermal neutron sensitivity. The bed has a diameter of 10 cm and a height of about 50 cm, and is contained in a double-wall, insulated crucible. The crucible provides a nearly adiabatic boundary condition on the bed bottom and walls.

The debris bed, crucible, and water bath are enclosed in the primary containment vessel. To prevent fission product release in the event of any primary boundary failure, a secondary containment vessel completely surrounds the primary vessel. The concentric-flow heat exchanger is attached to the secondary vessel. The manifold on the top of the heat exchanger routes cold helium gas down the outside of the secondary containment vessel and receives the return flow from the outer annulus of the package. The primary vessel instrumentation is routed through the secondary containment and enters the primary vessel through the instrumentation pass-thrus.

The DCC auxiliary systems and their interconnection to the experiment package are shown in Fig. 2.2. The debris bed is fission heated in the central irradiation cavity of the Annular Core Research Reactor (ACRR). The experiment package is suspended from a shield plug which contains serpentine instrumentation cables and cooling lines. Cooling lines are connected via an overhead trough to the mobile helium cooling loop located outside of the reactor highbay. The return flow from the loop to the package can be diverted to a heat exchanger in the liquid nitrogen tank to provide additional cooling capacity. Diagnostic instrumentation from the package is monitored by an HP-9845/HP-1000 computer-based data acquisition system. A separate computer-based data acquisition system (HP9845) is used to monitor cooling loop parameters for diagnostic and control functions.

For the DCC-1 and DCC-2 experiments, the most important functional dependence to be investigated is the relationship between the dryout heat flux and pressure. The pressure level is set by controlling the saturation temperature of the water bath in the closed primary vessel. This is achieved by affecting a balance between the heat sources (fission heat and electric heater) and the cooling system. The lowest pressure which can be attained is the fill pressure of the primary containment (initially 10 psia). If non-condensable gases are generated during the course of the experiment, the pressure rises, and the lower pressure limit of the experiment increases. This effect was observed in DCC-1 where the pressure rose from the initial 10 psia to approximately 30 psia. In DCC-2, the pressure rose from 10 psia to about 60 psia.

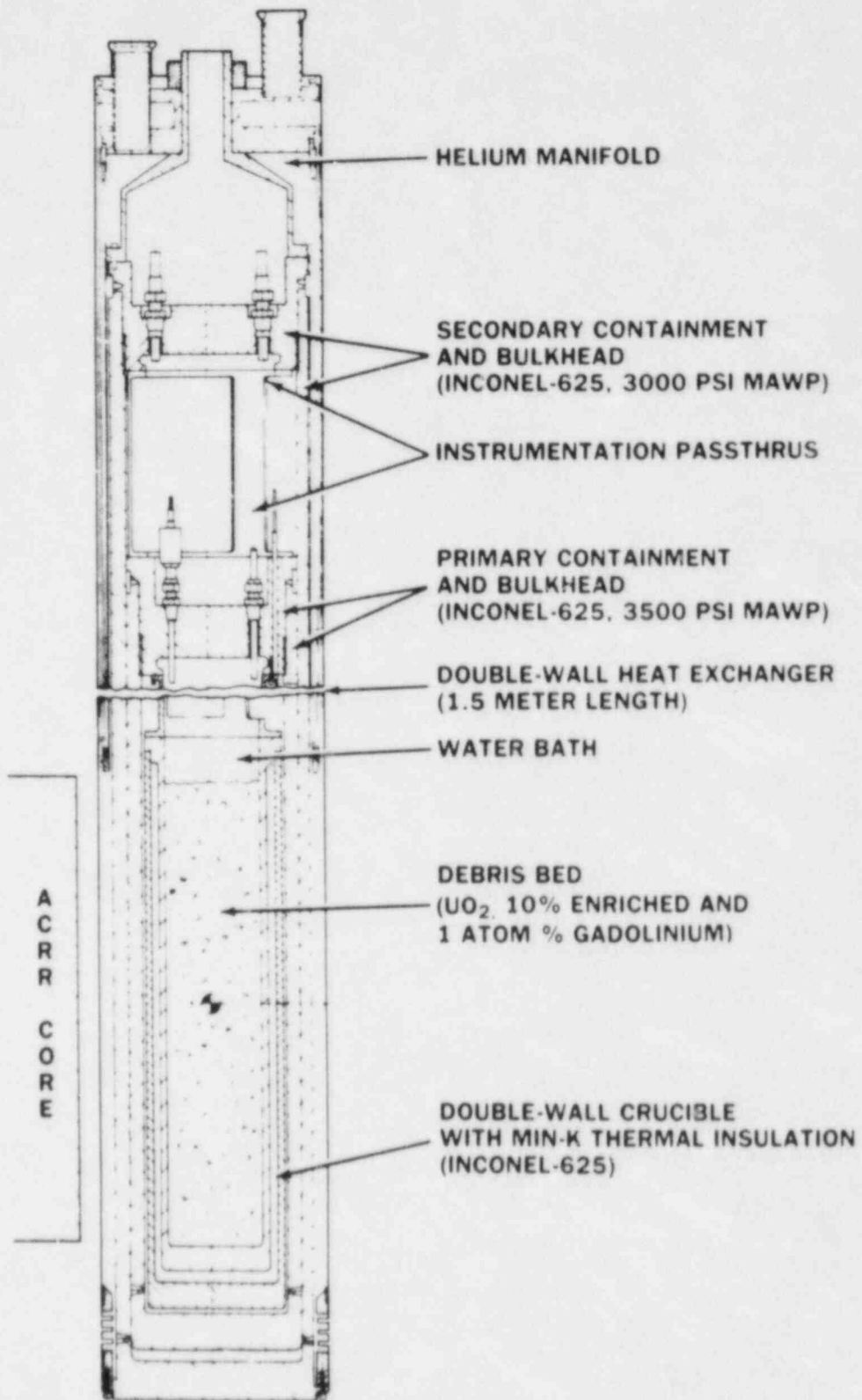


Figure 2.1 DCC Experiment Package

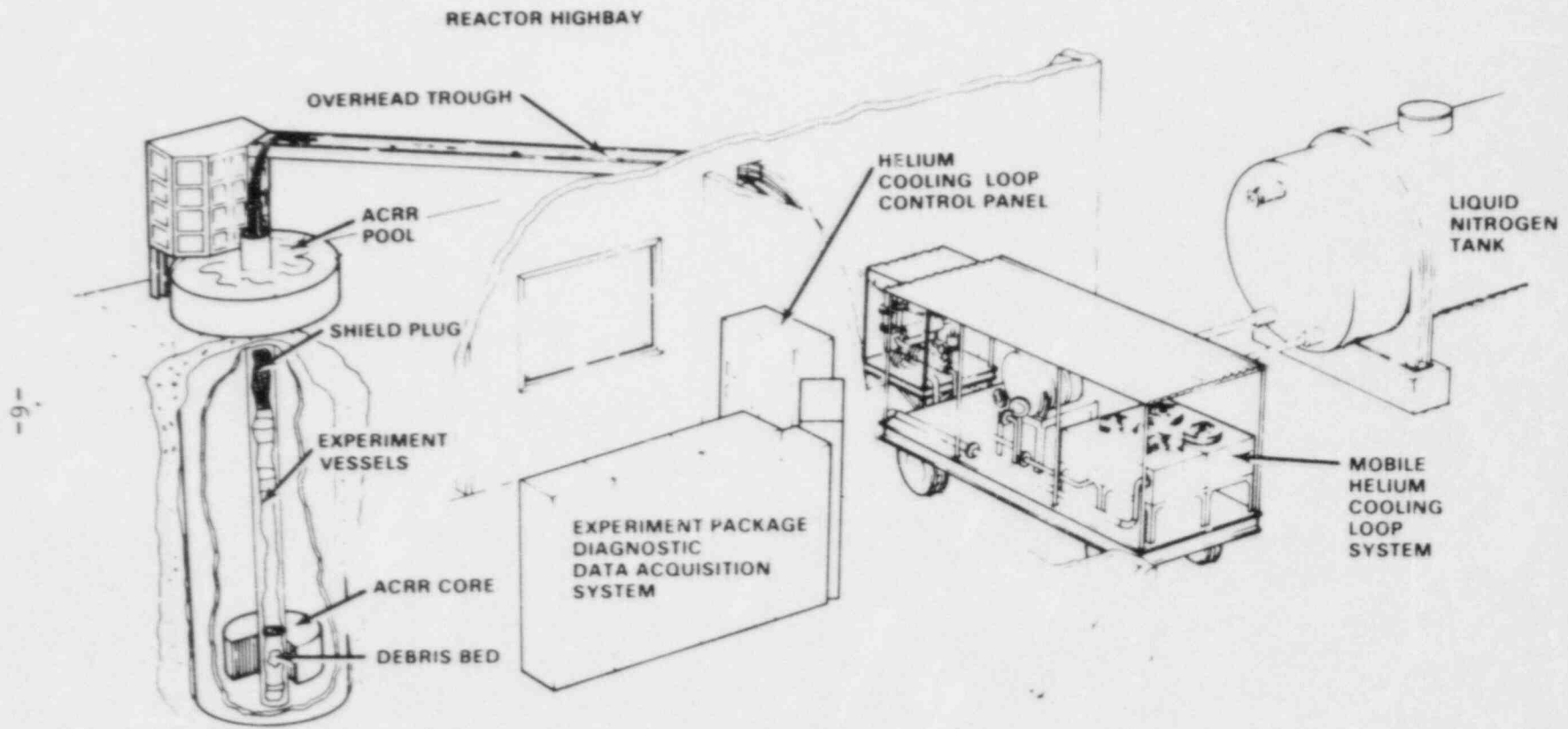


Figure 2.2 DCC Auxiliary Systems

A summary of the assembly procedure detailing the main components and tests is given in Fig. 2.3. To support the discussions of the results, the following assembly steps are described:

1. Primary Thermocouples
2. Fuel Loading
3. Hot MAWP Test
4. Water Loading
5. OPST's and IPST

2.1 Primary Thermocouples Locations

Sheathed K-type thermocouples (chromel-alumel) were used in these experiments. Bed thermocouples were introduced into the primary through seven passthru located in the primary bulkhead. Eight thermocouples were brazed into each passthru.

Of the 56 total thermocouples in the primary system, 36 are located in the bed as shown in Figures 2.4 and 2.5. These thermocouples are positioned vertically along the wall of the primary. The end of each thermocouple is bent horizontally to the correct radial position. The bed thermocouples are axially positioned in 2.5 cm increments along the bed centerline. Around the crucible, another 11 thermocouples are used in determining crucible heat losses, the level of the top of the bed, and water bath temperatures immediately above the bed.

2.2 Debris Bed Fuel Description and Loading

The debris bed consists of 10.6% enriched UO_2 particles with a small fraction of gadolinium in the form of Gd_2O_3 to serve as a thermal neutron poison. The poison decreases the influence of the liquid fraction on the local power density. Because the effect of the gadolinium in DCC-1 (1.0 atom-percent) was not as great as predicted, the concentration for DCC-2 was increased to 3.6 atom-percent. For DCC-2, this was achieved by mixing 6.2 kg of 10.9% Gd-loaded fuel with 17.8 kg of 1.0% loaded fuel to obtain the higher concentration.

The size distribution of the particles composing the DCC-2 debris bed is relatively narrow, having an average diameter of 2.43 mm (Fig. 2.6). By comparison, DCC-1 contained a broad particle distribution with an average diameter of 0.75 mm. The DCC-2 distribution was selected to provide data in the transition and turbulent coolability regimes, whereas DCC-1 operated in the laminar regime. The DCC-2 particle distribution contained a small portion of fine debris (less than 0.1 mm) to closely simulate observed particle distributions in LOCA tests and to emphasize the significance of small particles on bed coolability.

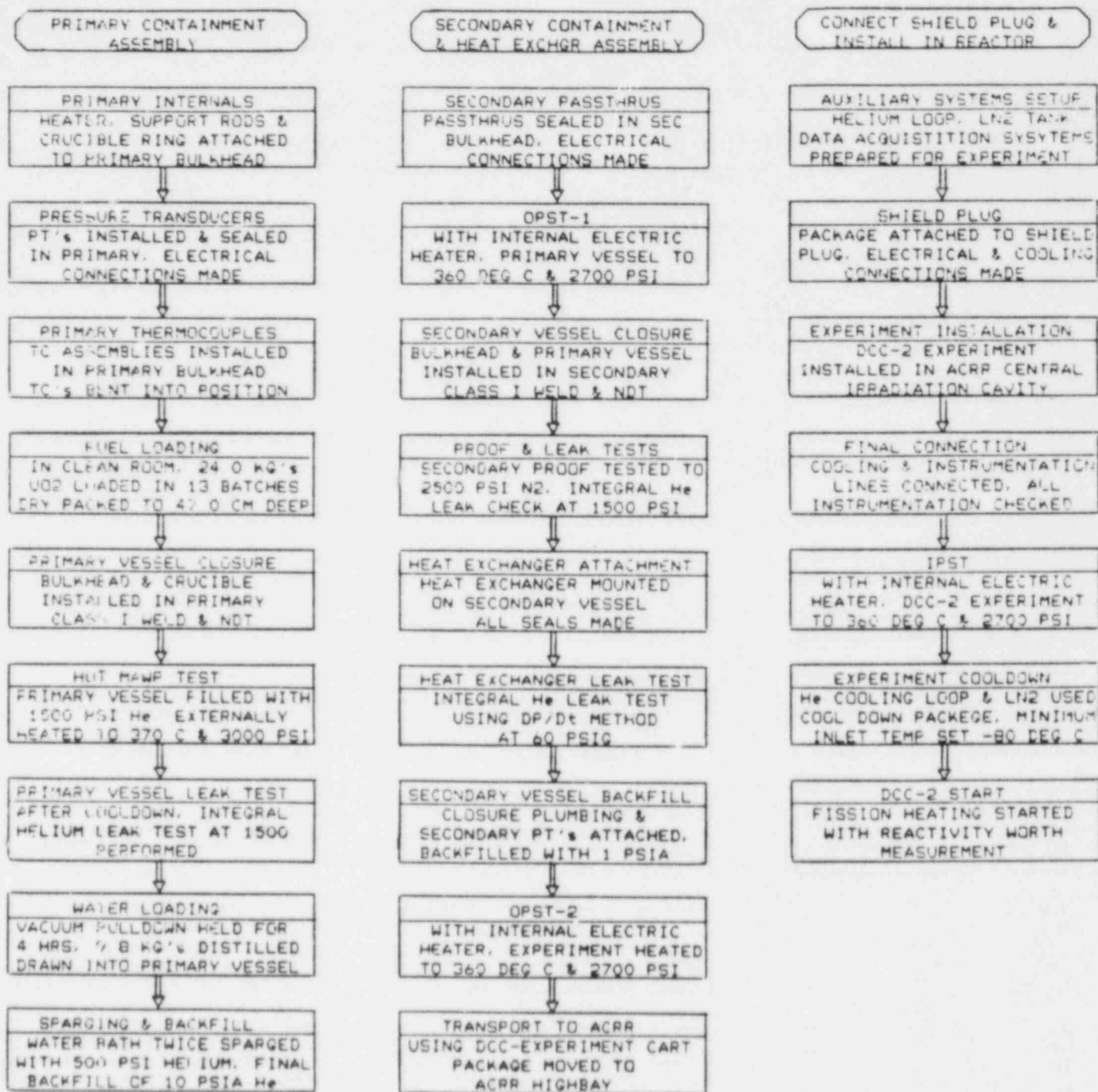


Figure 2.3 Assembly Procedure Summary for the DCC-2 Experiment

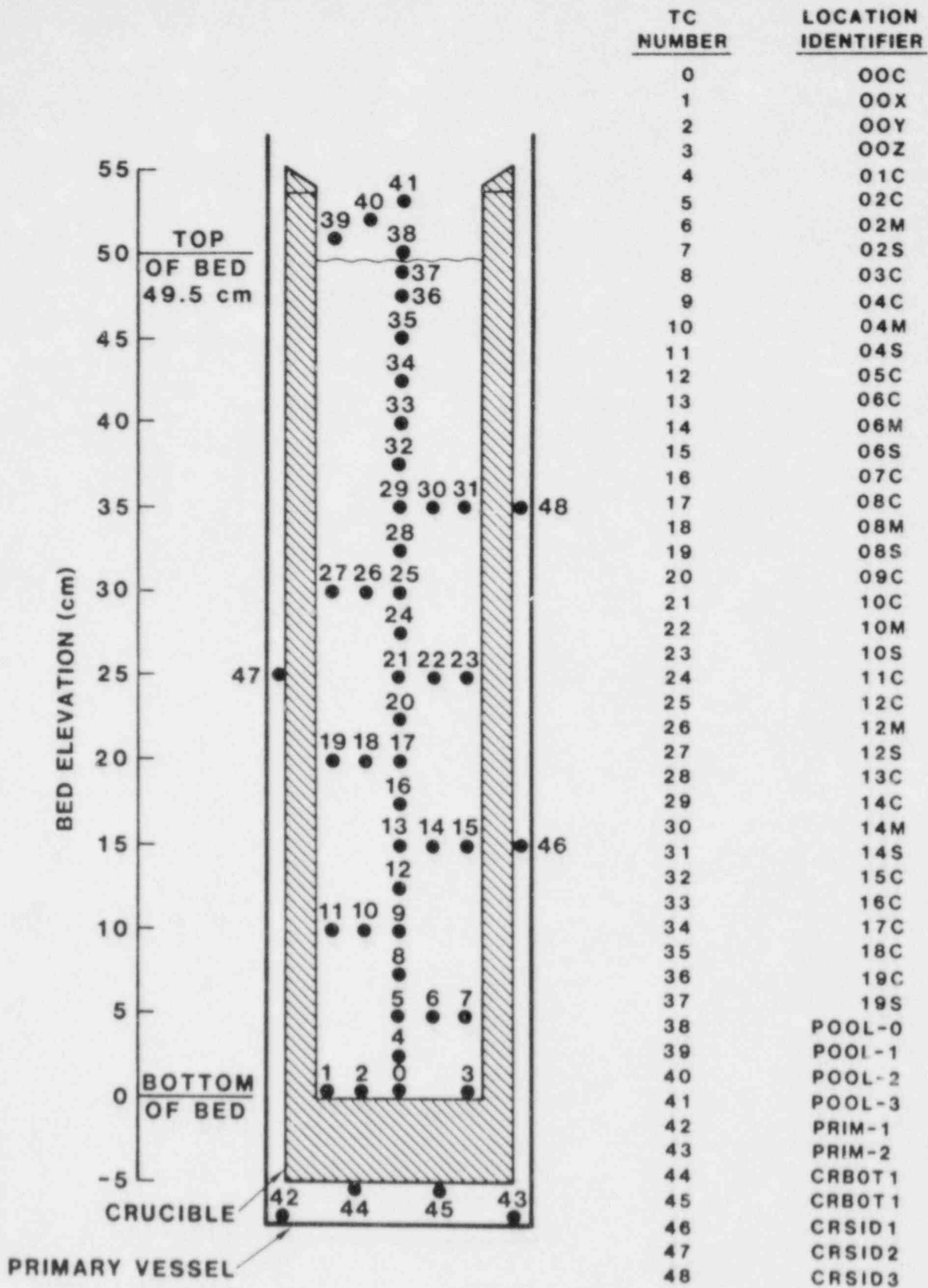


Figure 2.4 DCC-1 Thermocouple Locations

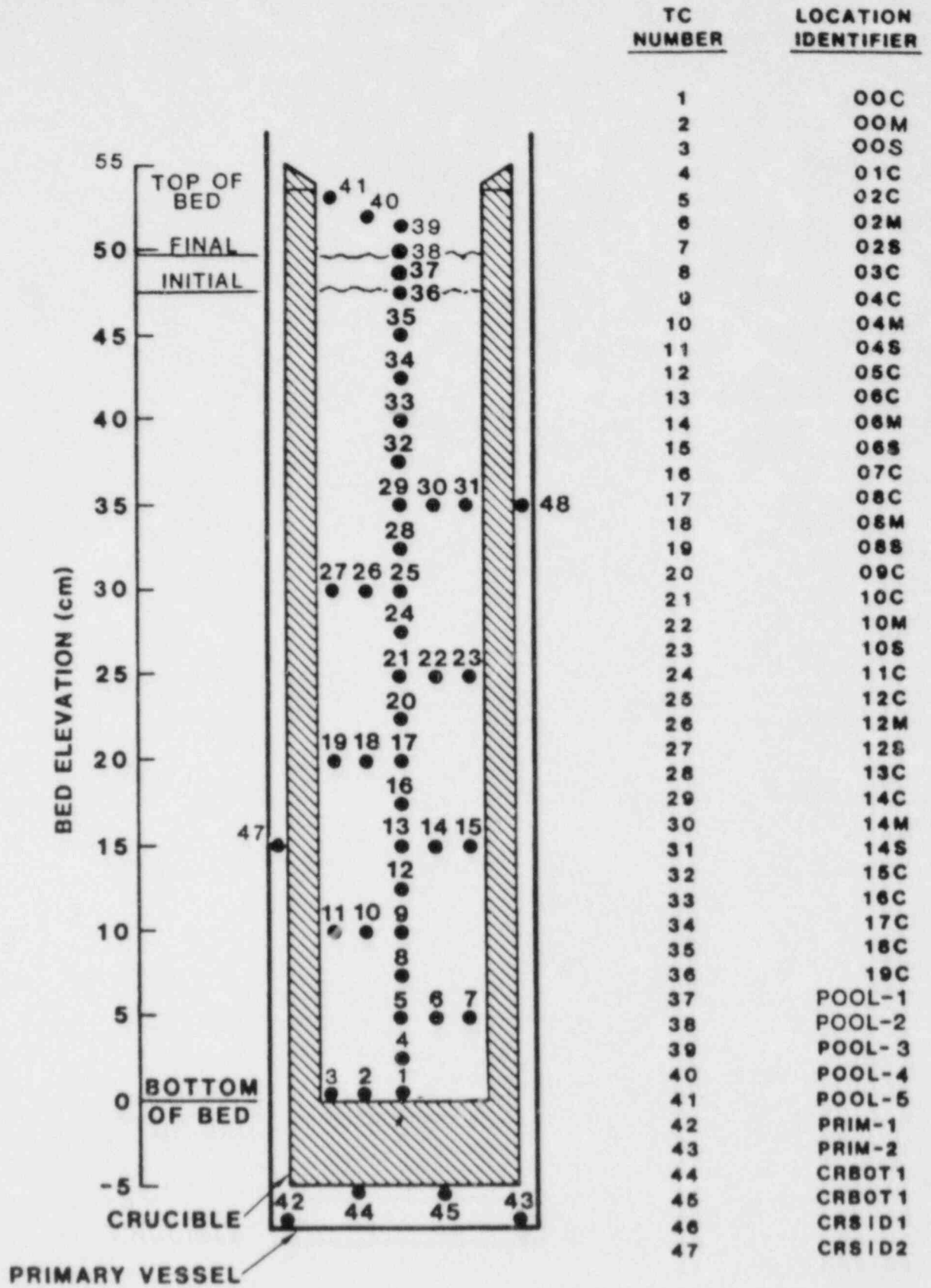
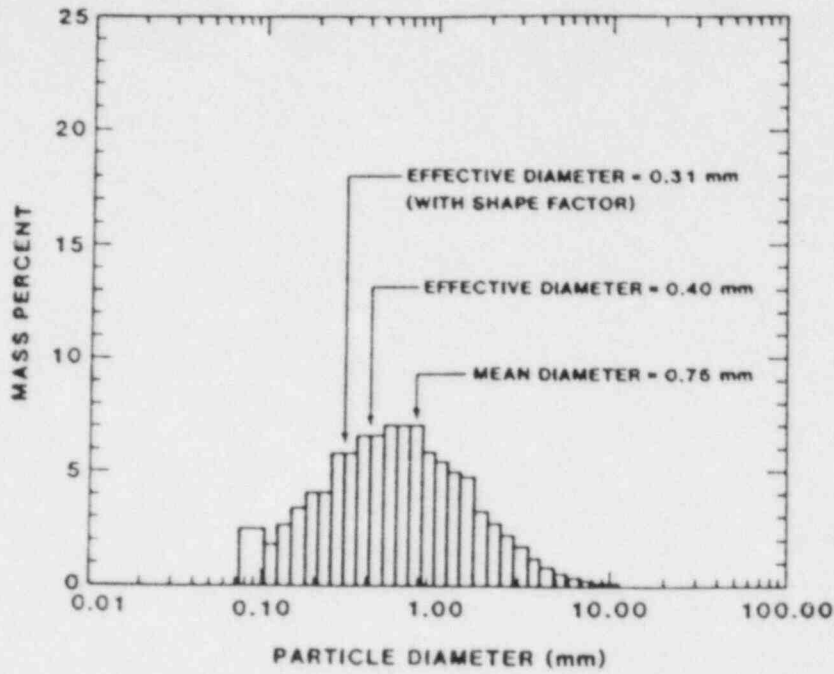


Figure 2.5 DCC-2 Thermocouple Locations

DCC-1 PARTICLE DISTRIBUTION



DCC-2 PARTICLE DISTRIBUTION

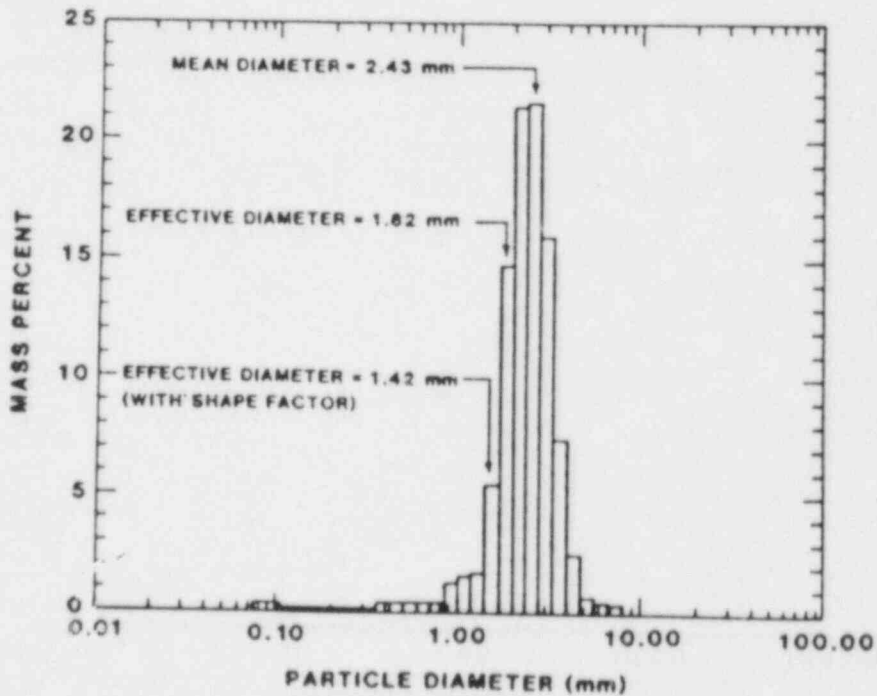


Figure 2.6 DCC Particle Distributions

In DCC-2, the addition of very fine particles to the otherwise logarithmic diameter distribution caused concern about particle migration. To investigate this, a pre-assembly packing test was conducted in which 1 kg of fuel was poured into a graduated cylinder, creating a bed 170 mm high. The fuel was then "packed" by tapping the side of the cylinder. Visual inspection of the fuel revealed that the fines in the upper 40 mm of the bed had settled into the lower portion of the bed. Additional tapping failed to cause further particle migration.

To limit the amount of particle settling observed in the pre-assembly test, the fuel was proportionately weighted and mixed into 13 batches (11 batches each containing 2.0 kg and two batches with 1.0 kg). Fuel loading was performed by thoroughly mixing each batch and pouring it into the crucible while simultaneously tapping the crucible to pack the bed. Based on the pre-assembly test, settling may have occurred within each batch, but inter-batch migration of fines probably did not take place. The total fuel loading for DCC-2 was 24.0 kg, a bed height of 47.0 cm, and an achieved porosity of 38.4%. After fuel loading, the pool thermocouples were repositioned at 1.0 and 2.0 cm above the bed. These thermocouples were later used to detect changes in the bed height. DCC-1 was loaded in a similar manner. The total fuel loading for DCC-1 was 27.0 kg and the porosity was 31.0%.

2.3 Hot Maximum Allowable Working Pressure (MAWP) Test

The hot MAWP test was intended to demonstrate the sealed primary vessel integrity under the most severe accident conditions for the experiment. The test was performed immediately prior to the integral leak test to assure that any leak generated during the hot MAWP test would be detected. The setup for the test consisted of the urania-loaded crucible sealed in a dry primary vessel. The vessel was initially filled with 1500 psi of helium gas and then heated with external heaters to achieve a pressure of 3000 psi at approximately 370°C. The urania particulate in the debris bed was exposed to 3000 psi helium at an average bed temperature of about 250°C for a period of about two hours.

2.4 Water Loading

Following the integral helium leak test, a vacuum was pulled on the primary system and maintained for four hours. With the package still under a vacuum, a water fill tube was connected to the backfill port and 9.8 kg of distilled water was loaded into the vessel. This procedure assured that non-

condensables were not trapped in the interstices of the bed. After the water fill, the primary system was sparged twice with 500 psi helium gas to remove dissolved oxygen from the water bath. The second sparge was depressurized to 10.0 psia and the primary system was sealed. ●

2.5 Out-of-Pile Systems Tests (OPST) and In-Pile Systems Tests (IPST)

Three DCC systems tests were performed prior to nuclear heating to assure that all designed performance specifications for the experiment package and auxiliary systems were satisfied. The tests consisted of two OPST's (OPST-1 and OPST-2) and one IPST. OPST-1 demonstrated the internal electric heater (4 kW cartridge unit) performance and the response of the primary pressure transducers under operating conditions. During this test, the fueled primary vessel was pressurized to 2700 psi by increasing the saturation temperature to 360°C. In OPST-2 the same conditions were achieved with the secondary vessel and heat exchanger assemblies completed. The most important data obtained in the second OPST were the temperatures in the heat exchanger and the natural convection heat loss from the package (approximately 2.9 kW). The IPST was performed prior to the start of fission heating with the package in the reactor and all auxiliary systems connected. Again, the package heater was used to pressurize the primary system to 2700 psi at 360°C. The IPST checked out all instrumentation connections, cooling-loop performance, and data acquisition system operation.

3. PRESENTATION OF DATA

3.1 DCC-1 Experiment

The DCC-1 experiment was initiated on August 23, 1983 (Appendix Table A1). During the first two hours of the experiment, two bed power calibrations were conducted at a temperature of about 40°C, and the first boiling state was established at about 98°C. After the bed had equilibrated, the search for the first dryout point was initiated. Dryout was approached by incrementing the reactor power in 2 kW steps from 7 kW to 18 kW over a period of about 80 minutes. Dryout occurred when the reactor power was increased from 16 to 18 kW (Fig. 3.1). Reactor power was then cut to levels of 15, 10, 5, and 1 kW at times of about 15, 18, 22, and 32 minutes respectively. Fuel temperatures did not stop increasing until the power was reduced to the 1 kW level.

At this time, it was felt that the time interval between power steps may have been too small. The measurement was therefore repeated at 101°C. Dryout occurred after a step from 15 kW to 16 kW (Fig. 3.2).

The pressure dependence of the dryout curve was investigated during the second through the fourth days of the experiment. Saturation temperature ranges from 100 to 353°C (Figs. 3.3-3.6). The increment in saturation temperature was about 20°C. At the end of the fourth day, the incipient dryout point at 151°C (DO 21) was repeated. The lack of change in the dryout power indicated that the bed configuration had not changed during the experiment.

It was apparent at this point that the pressure dependence of the dryout data was not as expected. Therefore, on the fifth day, incipient dryouts were reproduced at 220°C, 303°C, 322°C, and 342°C (DO 23-26). Once again, these measurements coincided with the earlier data.

There was also some concern about the heat losses from the debris bed affecting the dryout data. To check for this, a procedure was instituted which reduced the temperature difference across the crucible wall. Instead of increasing the saturation temperature to obtain the next data point, the saturation temperature was dropped suddenly to the new level. Thermal inertia kept the outer crucible wall at an elevated temperature during the search for dryout, thereby reducing the heat losses to levels lower than those experienced using the standard procedure. Incipient dryout points at 224°C (DO 28) and 133°C (DO 30) were obtained in this manner. These power levels again coincided with the earlier data indicating that heat losses did not significantly affect the data.

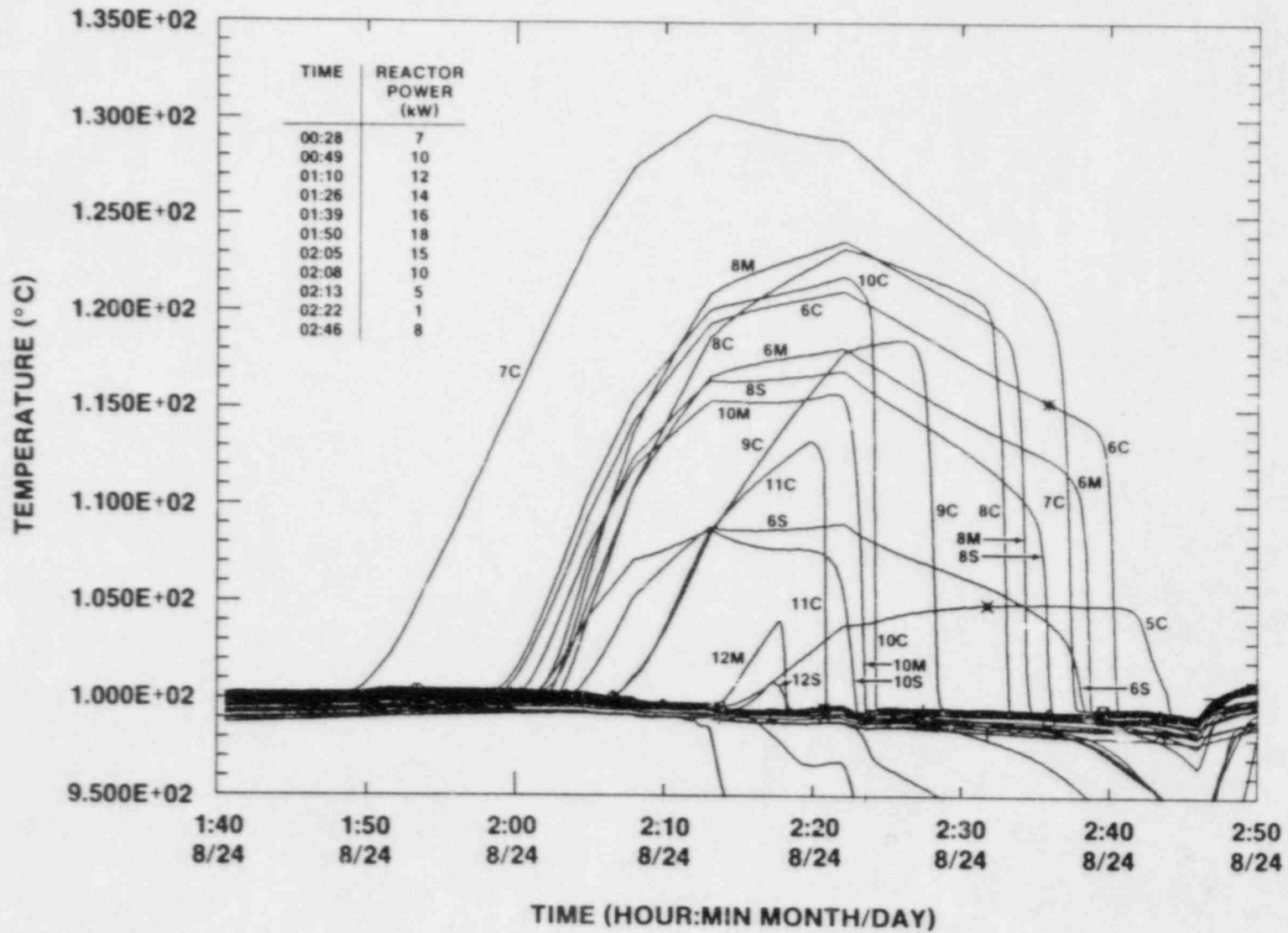


Figure 3.1 DCC-1 Dryout #1, $T_{sat} = 100^{\circ}\text{C}$ (Incipient)

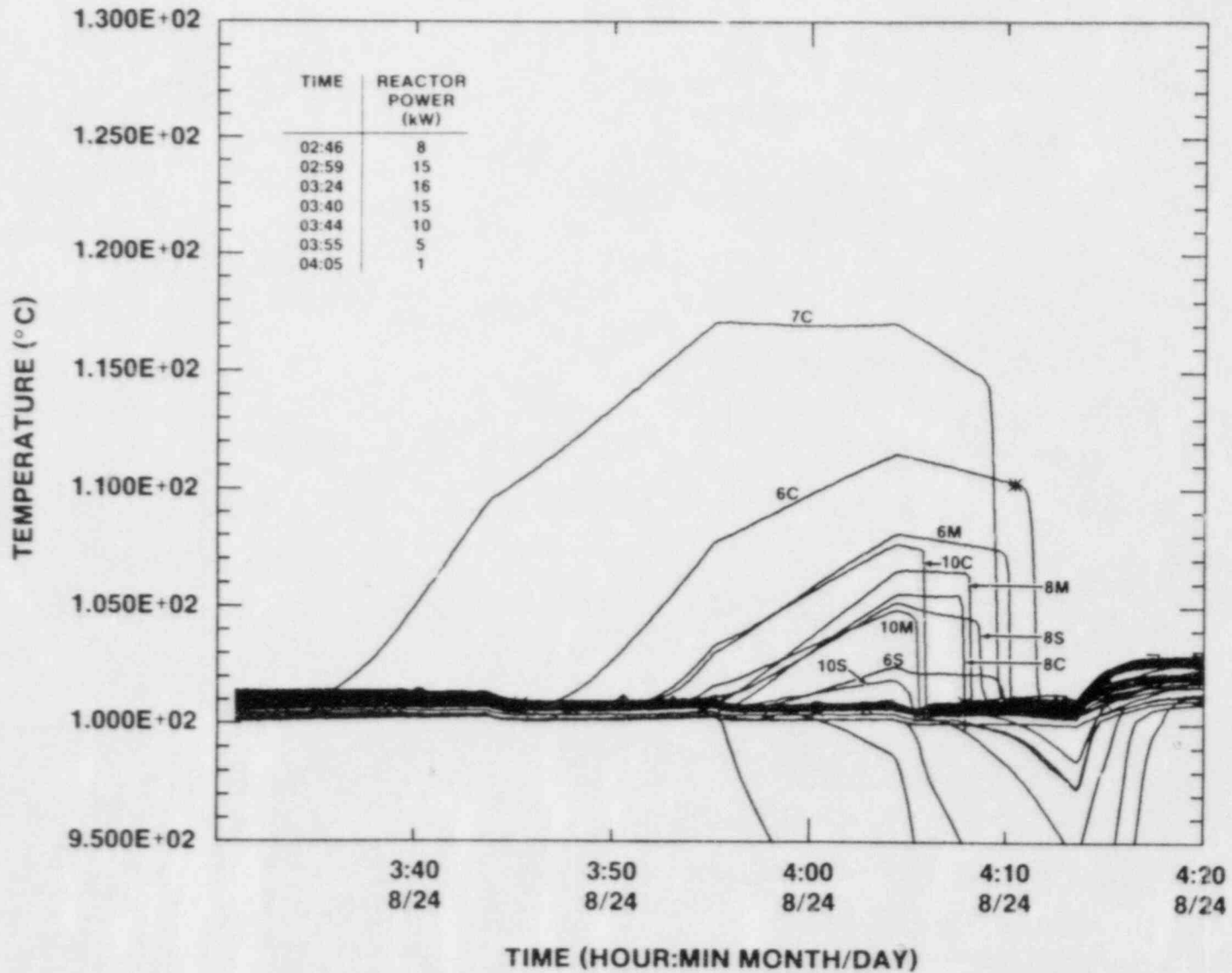


Figure 3.2 DCC-1 Dryout #2, $T_{sat} = 101^{\circ}\text{C}$ (Incipient)

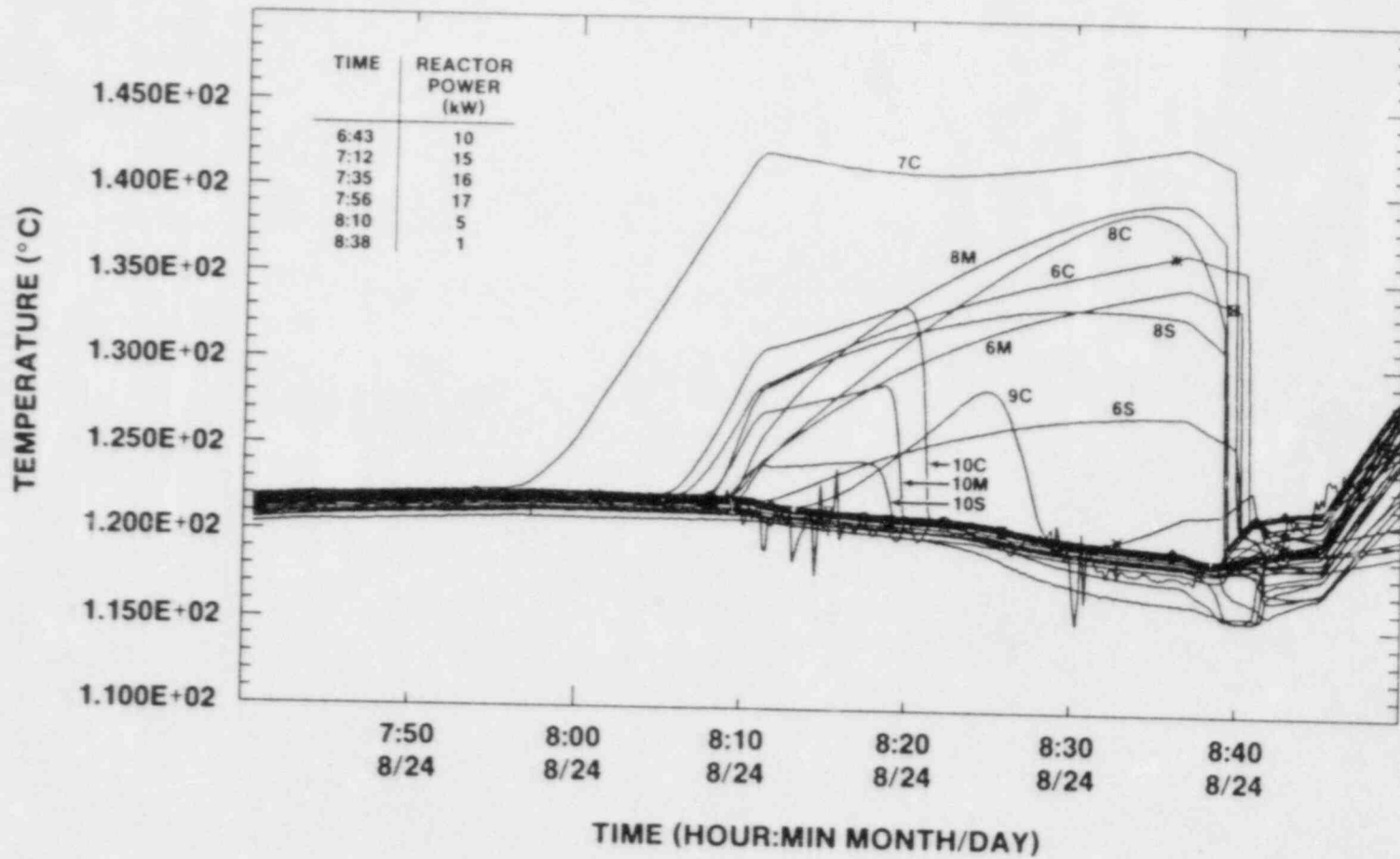


Figure 3.3 DCC-1 Dryout #5, $T_{sat} = 122^{\circ}\text{C}$ (Incipient)

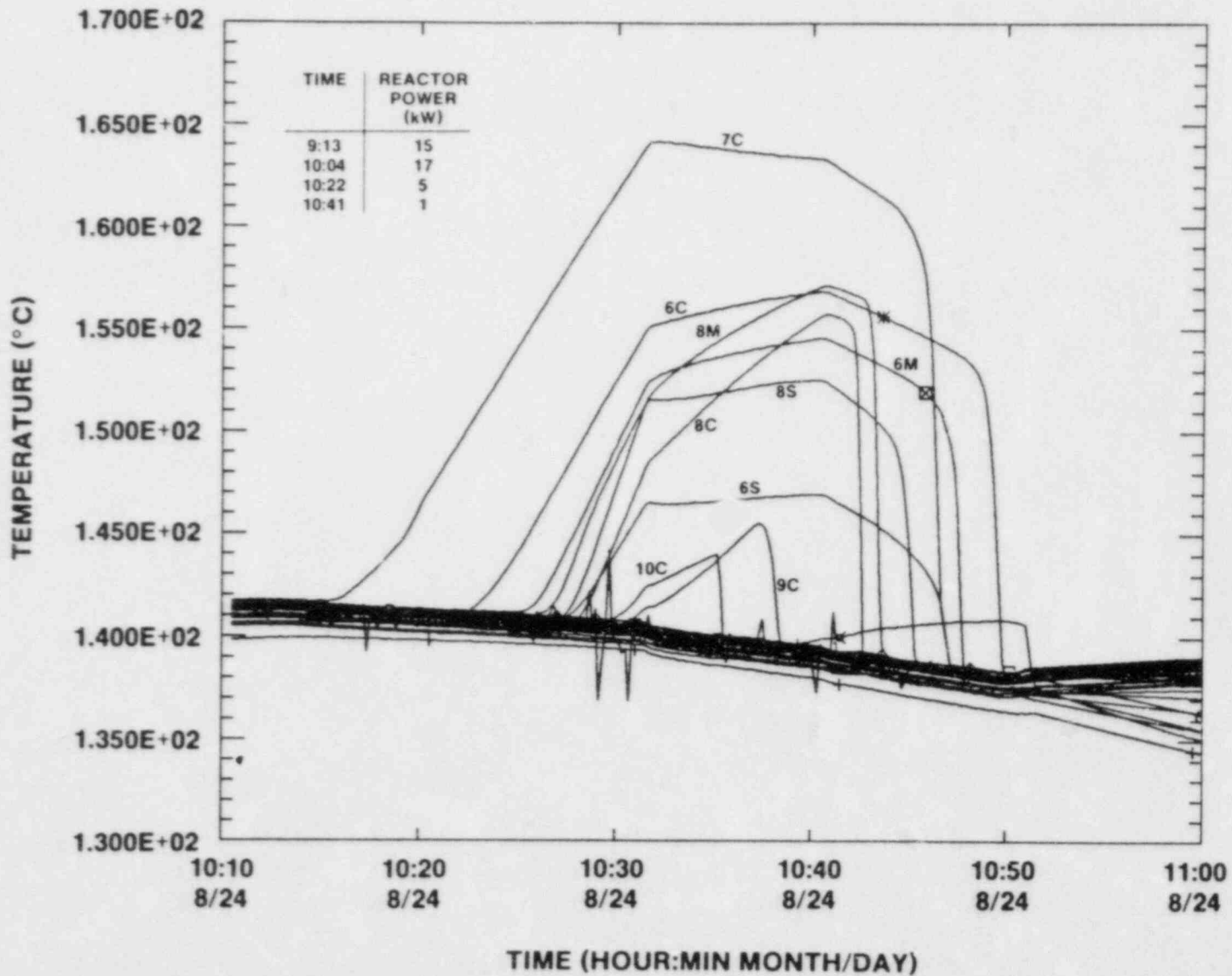


Figure 3.4 DCC-1 Dryout #6, $T_{sat} = 141^{\circ}\text{C}$ (Incipient)

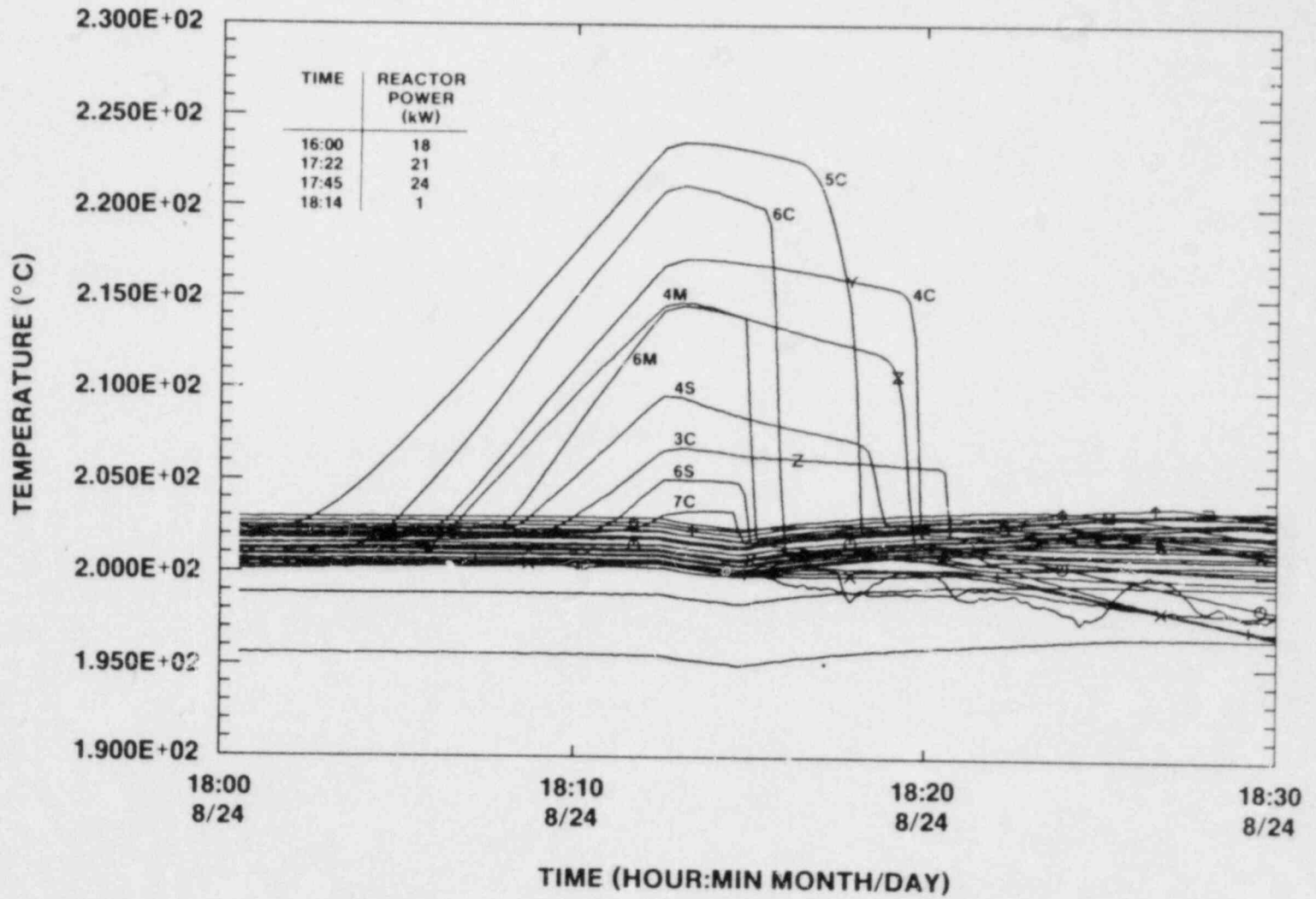


Figure 3.5 DCC-1 Dryout #9, $T_{sat} = 202^{\circ}\text{C}$ (Incipient)

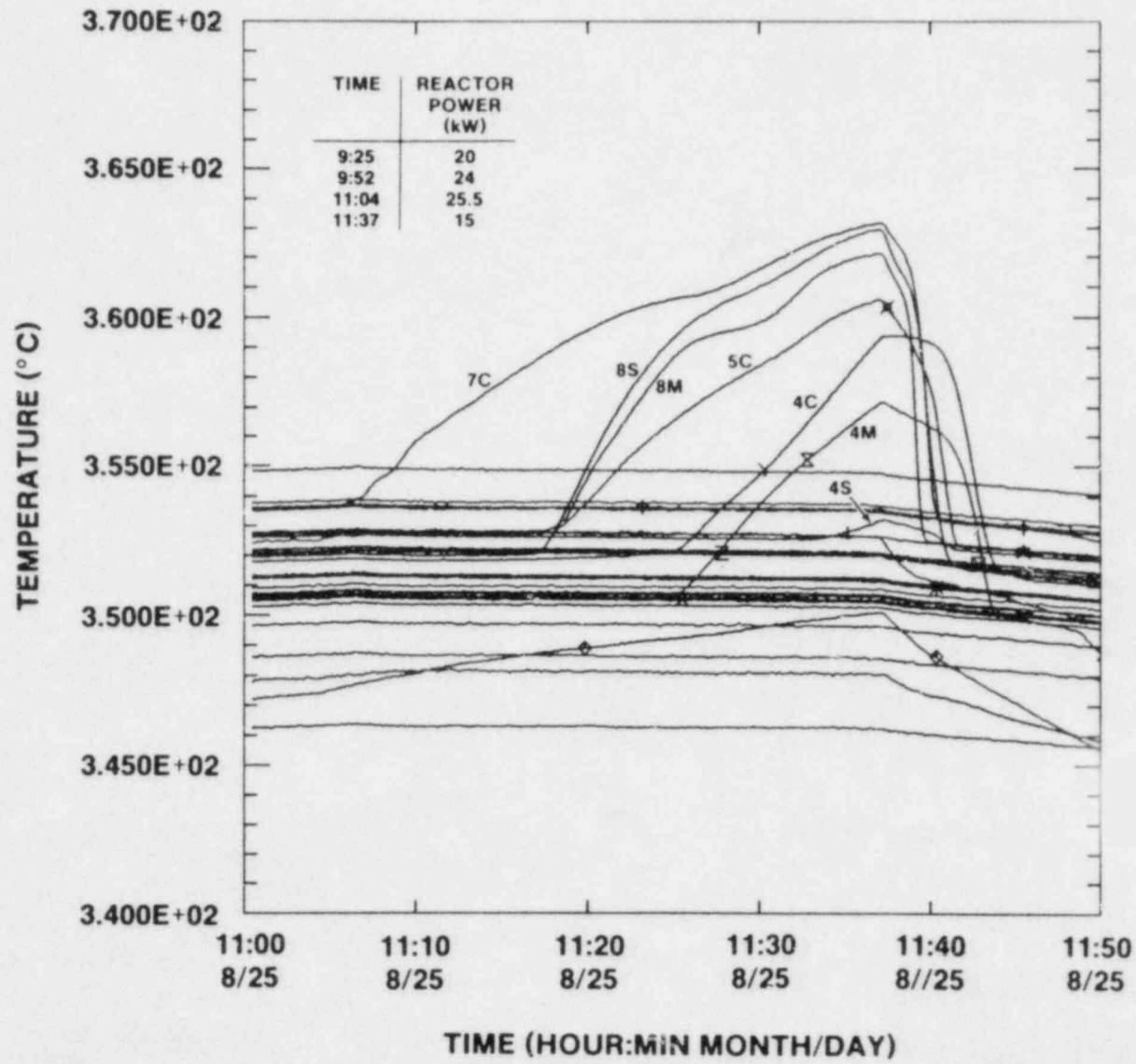


Figure 3.6 DCC-1 Dryout #18, $T_{sat} = 353^{\circ}\text{C}$ (Incipient)

Having obtained and confirmed the pressure dependence of incipient dryout, the transient and post-dryout behavior of the bed was then examined. First, incipient dryout powers at temperatures of 104°C, 122°C, and 141°C were repeated and found to be unchanged. The next two dryouts, conducted at 142°C, were executed by bringing the reactor power from just below incipient dryout power to a preset factor above the known dryout power. This was done to examine changes in the initial location of dryout as a function of reactor power. Incipient dryout was first observed at thermocouple 7C (DO 33). At a reactor power 1.5 times that of incipient dryout, dryout was first observed at thermocouple 5C (DO 34). At a reactor power 2.0 times incipient dryout power, dryout was first observed at the thermocouple 7C (DO 35). This last dryout was extended until a fuel temperature of 330°C was obtained (Fig. 3.7). The quench that followed took about two hours to complete.

This procedure was continued the following day. The incipient dryout power 141°C was found to be unchanged (DO 36). A forced dryout was then conducted with a power step 3 times that of incipient dryout power (DO 37). The initial location of dryout was thermocouple 7C.

On the seventh day of the experiment, the transient dryout behavior was examined at a new temperature of about 222°C. The reactor power at incipient dryout was found to be between 25.5 to 27.0 kW (DO 38). This is slightly higher than the previously measured value of between 24.0 to 25.5 kW (DO 11, DO 23, DO 28). This indicated that the power step taken the previous day had loosened the bed slightly. The first dryout location was at thermocouple 5C. Three forced dryouts were then conducted at levels of 1.4, 2.0 and 3.0 times the incipient levels. Initial locations were at thermocouples 5C, 7C, and 5C/7C respectively. The last of these was extended to a maximum temperature of 850°C (Fig. 3.8). The quench of this extended dryout took about two hours to complete. The increase in saturation temperature initiated in the last hour of the quench reduced the required quench time.

During the final two days of the experiment, the effect of bed disruption was investigated. First, the incipient dryout reactor power at 141°C was found to be between 17 to 18 kW. The increase over the previously measured power to 15 to 17 kW (DO 6, DO 33, DO 36) reflects the same slight loosening of the bed observed the previous day. The dryout was then extended to study the quench behavior (Fig. 3.9). The quench behavior of all the extended dryouts displayed common characteristics. Unlike most out-of-pile experiments, no liquid fingers penetrated the dry zone. The quench began at the top of the dry zone and proceeded in a reasonably uniform manner downward. Quench times were measured in hours.

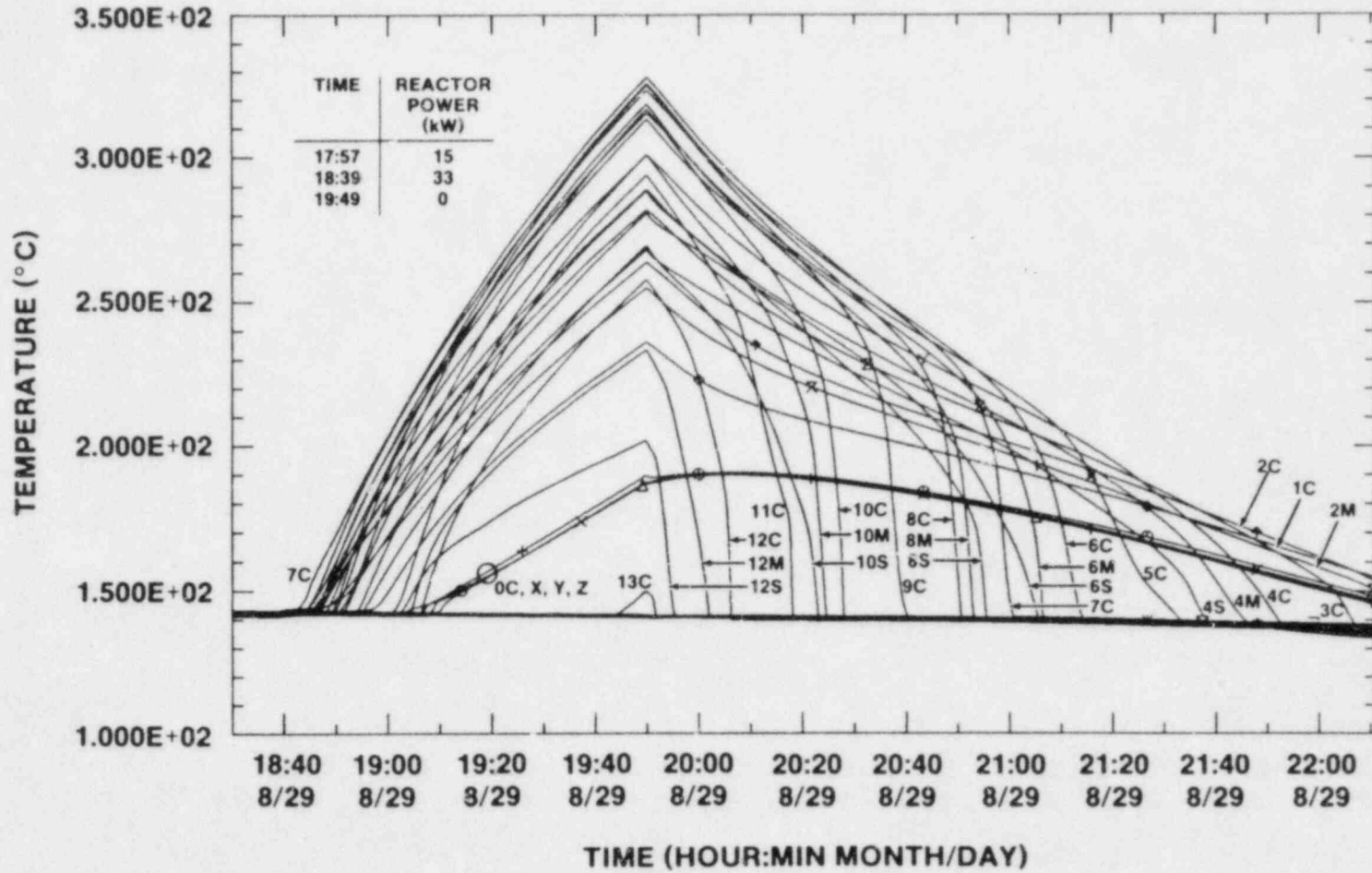


Figure 3.7 DCC-1 Dryout #35, $T_{sat} = 142^{\circ}\text{C}$ (Forced and Extended)

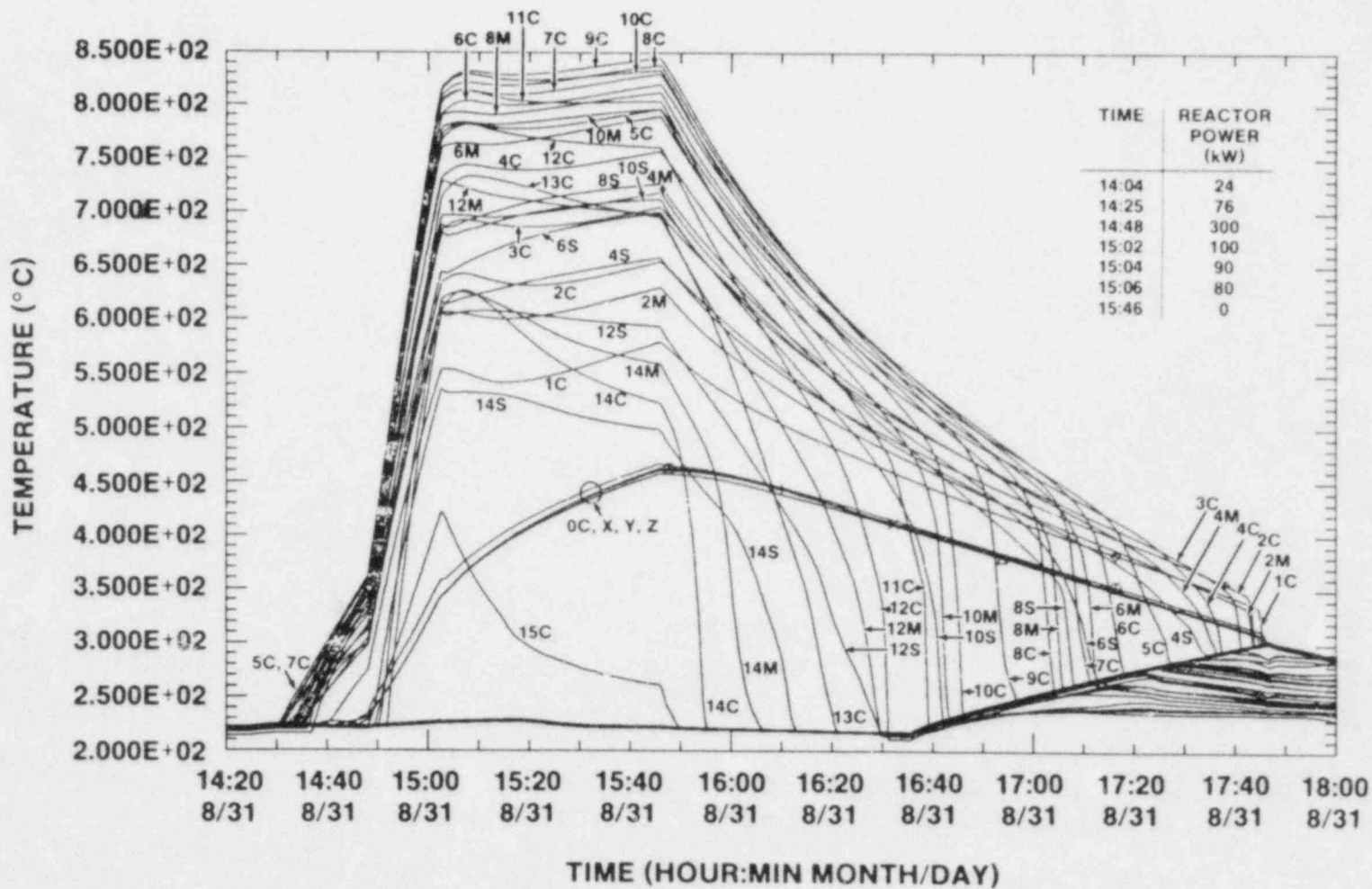


Figure 3.8 DCC-1 Dryout #41, $T_{sat} = 222^{\circ}\text{C}$ (Forced and Extended)

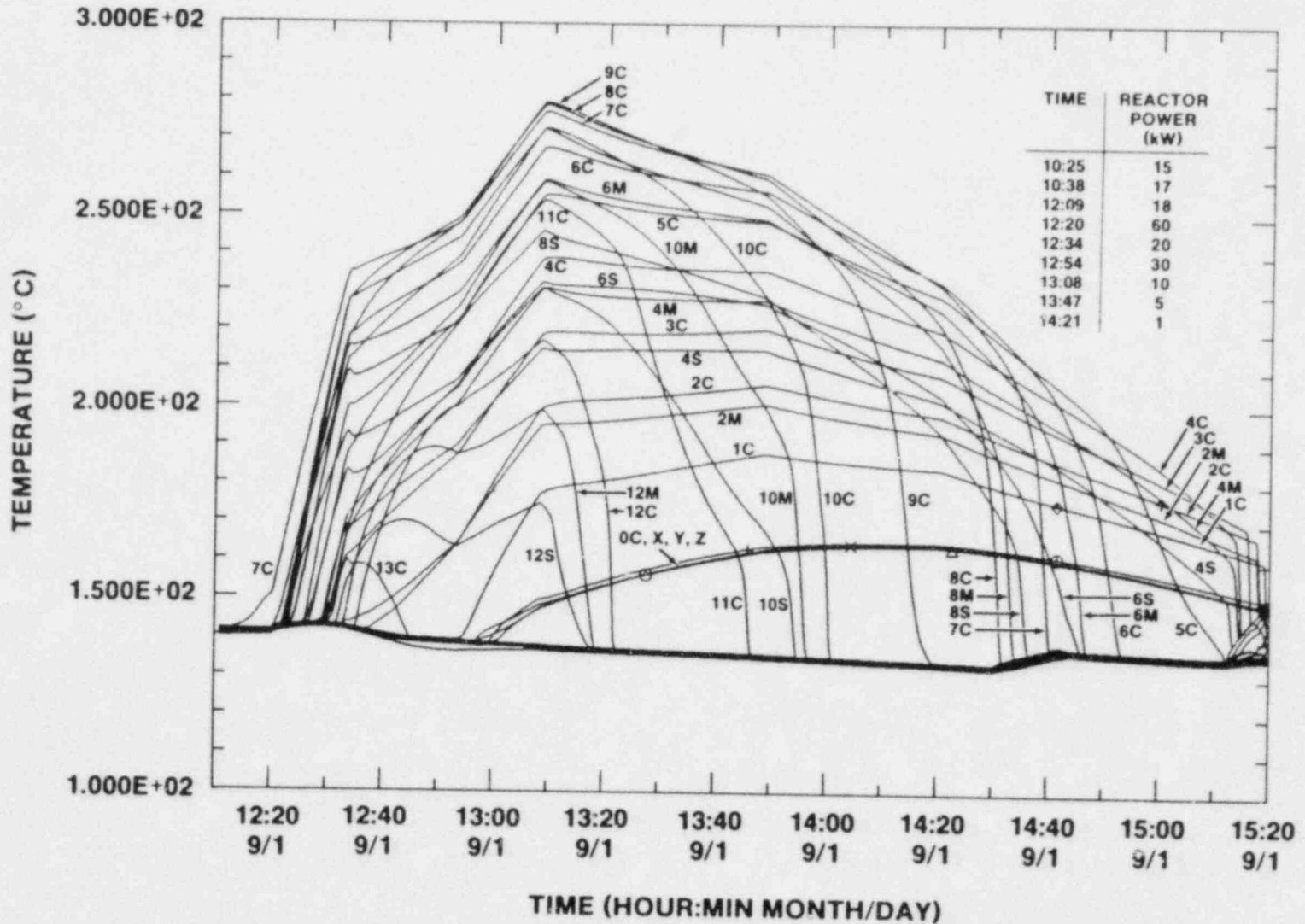


Figure 3.9 DCC-1 Dryout #42, $T_{sat} = 141^{\circ}\text{C}$ (Incipient and Extended)

The measurement of incipient dryout at 141°C served as a baseline for the condition of the bed. Three attempts were then made to disrupt the bed by taking large steps in reactor power (300 kW for dryout 43, and 1000 kW for dryouts 45 and 47). Each of these attempted disruptions was followed by a measurement of incipient dryout powers. Dryouts 44, 46, 48, and 49, taken at temperatures of 169°C, 219°C, 140°C, and 221°C, respectively, displayed increases in reactor power of about 19%, 15%, 44%, and 21%, respectively. On September 1, 1983, the DCC-1 experiment was terminated.

3.2 DCC-2 Experiment

The DCC-2 experiment was initiated on April 6, 1984 (Appendix Table A2). Three bed power calibrations were made while the water was subcooled. The power was then slowly increased until boiling in the bed was initiated. The first bed boiling temperature was 95°C and was obtained with the pool subcooled. This boiling temperature indicated that the initial backfill pressure of 10 psia, with allowance for thermal expansion, was unchanged due to the elevated temperatures and pressures generated during the system tests.

On the first day of operation, dryouts were obtained by increasing the reactor power in small steps and waiting 10 to 20 minutes for incipient dryout. Initially, at the first sign of dryout, the reactor power was dropped on the assumption that the local initiation of dryout would spread across the width of the bed and a global dryout would ensue. The containment pressure was then increased, and the reactor power was incremented until incipient dryout was observed at the new pressure.

On the seventh dryout (Day 1), the reactor power was maintained past the point of incipience. The temperature data for this run indicated that, contrary to expectations, the dry zone stabilized locally without extending across the debris bed (Fig. 3.10), i.e. temperatures within the localized zone leveled off to a steady-state temperature in excess of the saturation temperature. This formation of a stable localized dry zone had not been observed in DCC-1 or the D series^[19] of LMFBR bed experiments.

In order to assure that global dryouts were obtainable in this bed, the next dryout was performed at the same pressure as DO 7 (Figure 3.10). The power was quickly raised to the level set in DO 7, and the local dry zone was established. The power was then increased until the dry zone extended across the width of the bed. This confirmed that global dryouts could be created at sufficiently high powers.

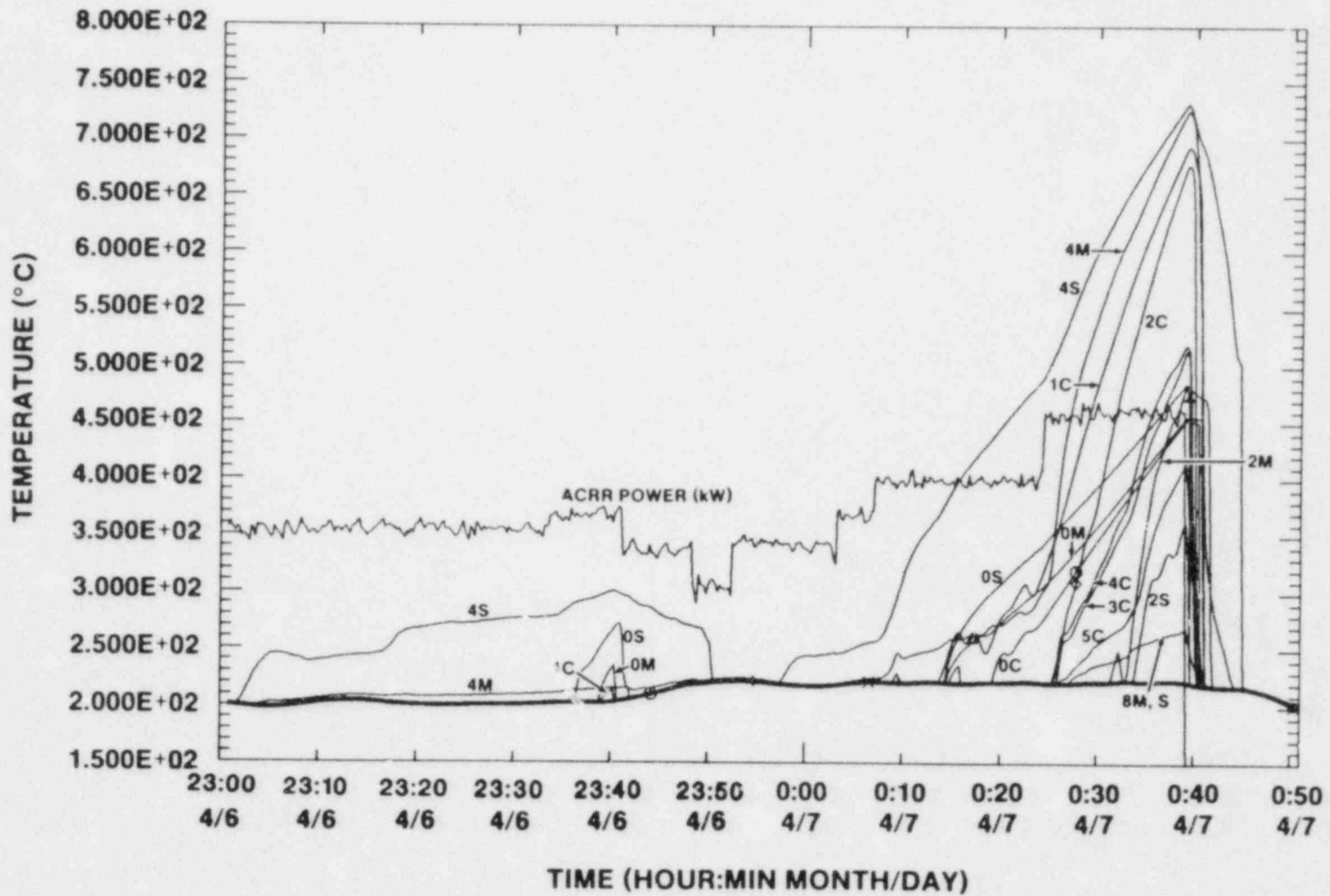


Figure 3.10 DCC-2 Dryouts #7 & 8, $T_{sat} = 200, 219^{\circ}\text{C}$, (Local and Global)

On the second and third days, the nature and extent of the local dryouts were explored. The plan was to search for incipient dryout and then keep increasing the power until global dryout was achieved. Typically, the initial dryout took place at thermocouple 4S or 8S (Fig. 2.5), located at the wall of the vessel, or at 8M. If the power step initiating dryout had been moderate, the temperatures stabilized in a matter of minutes and a local dry zone was quickly established. The size of the dry zone would vary in proportion to the reactor power, and could become quite large without becoming global (Figs. 3.11, 3.12). Frequently, temperatures at the vessel wall in a local dryout reached the 850°C safety limit. This prevented the continued increase of power necessary to reach global dryout.

By this time, a consensus among the program staff had been reached as to the probable cause of the local dryouts. During assembly, some of the fine particles may have segregated. Interpretation of the bed temperatures suggested that some of the fines had concentrated in the region monitored by thermocouples 4S and 8S (Fig. 3.13), creating a zone of low permeability. Reactor powers capable of drying this zone were unable to dry the horizontally adjacent zone which had a higher permeability. Water could flow through this zone of higher permeability to the bottom of the bed. Vapor generated in the boiling zones convected through the dry zone, stabilizing the particle temperatures at some level above the saturation temperature.

On the fifth day of operation, the particle bed was disrupted by applying a 3 MW power step for about 120 s. The rapid generation of vapor during such a step pushes liquid within the bed upward into the overlying pool. The drag on the particles induced by this flow tends to expand the bed and allow it to resettle in an expanded configuration. It was hoped that this procedure would loosen the region of low permeability and help to make the bed more homogeneous. Based on the behavior of the pool thermocouples after the disruption, it was concluded that the particles now covered thermocouple #38, indicating an increase in bed height of about 20 mm.

The next seven dryouts (DO 34 - DO 40) were obtained in the following manner: the reactor power was set just below the pre-disruption dryout power at a given pressure, and equilibrium was achieved. The power was then raised in a single step to between 125% to 200% of the pre-disruption dryout power. In all seven cases, only local dryouts were observed. DO 34 began at thermocouple 0C; the remaining six started at 4S.

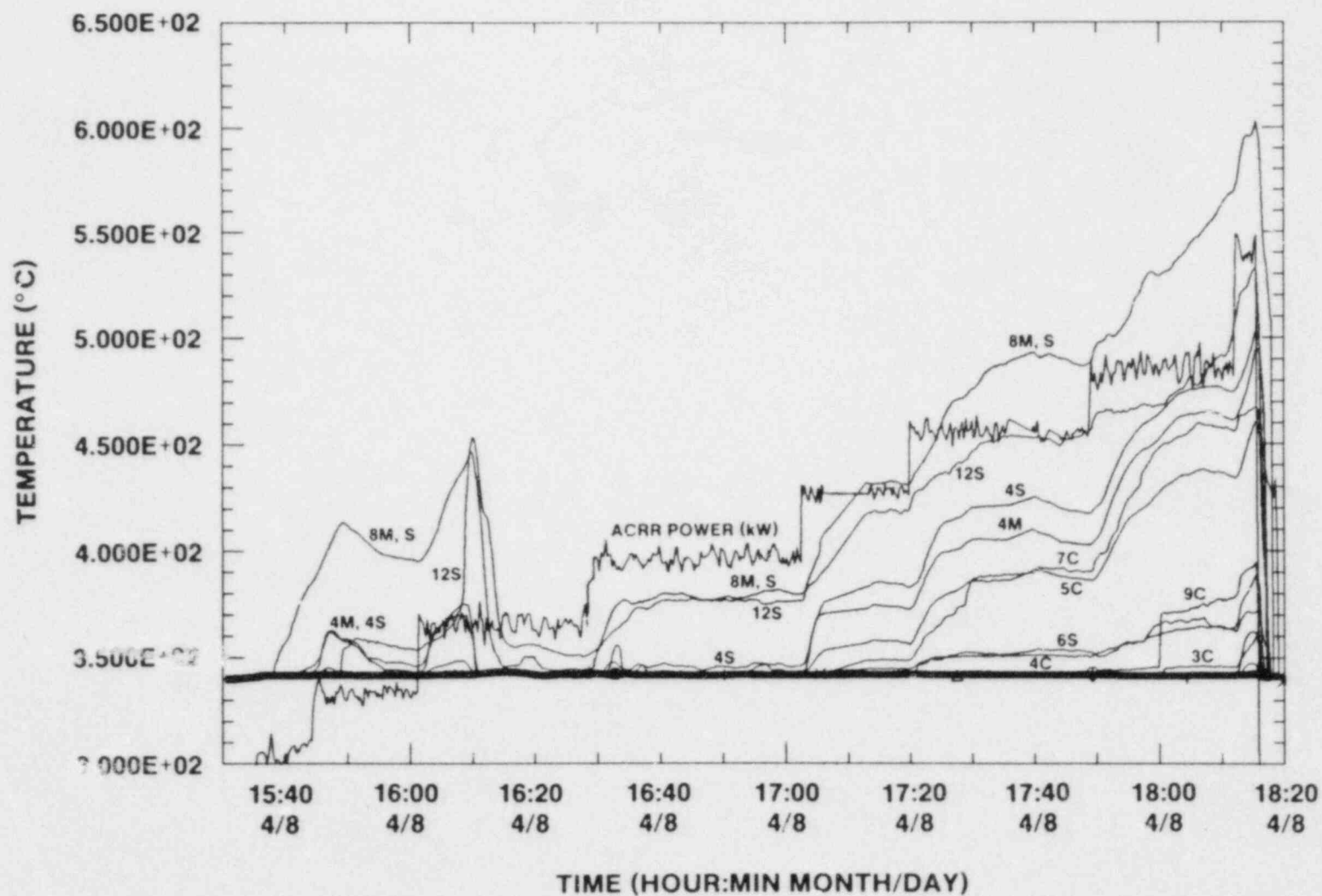


Figure 3.11 DCC-2 Dryout #22, T_{sat} = 341°C (Local)

LOCATIONS of INCIPIENT and EXTENDED LOCAL DRYOUTS

DRYOUT #22

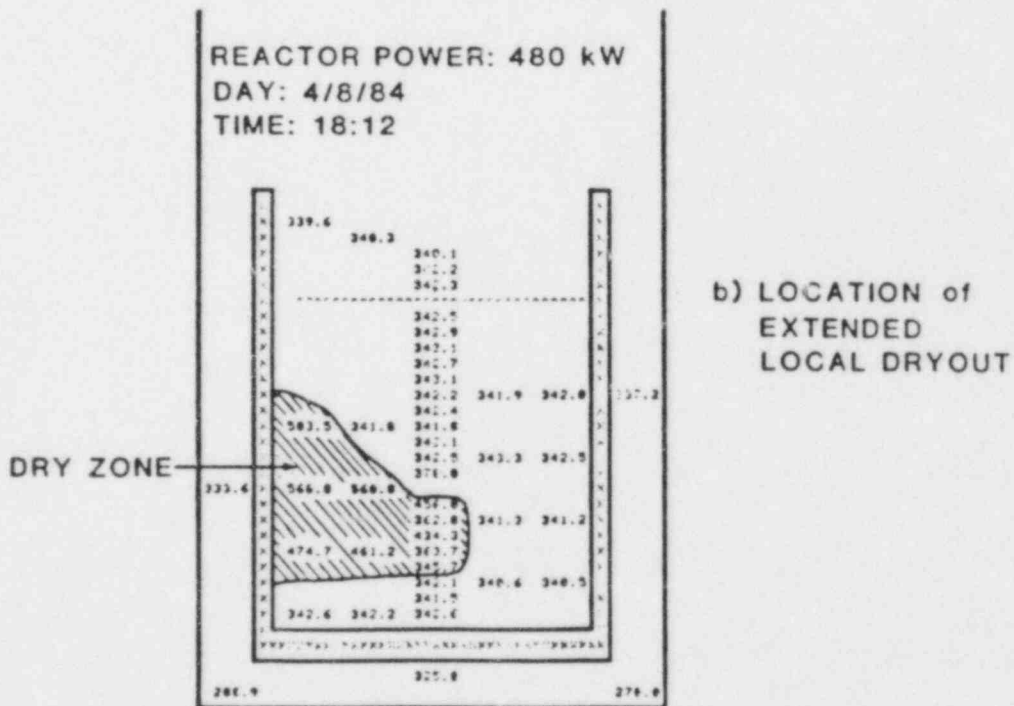
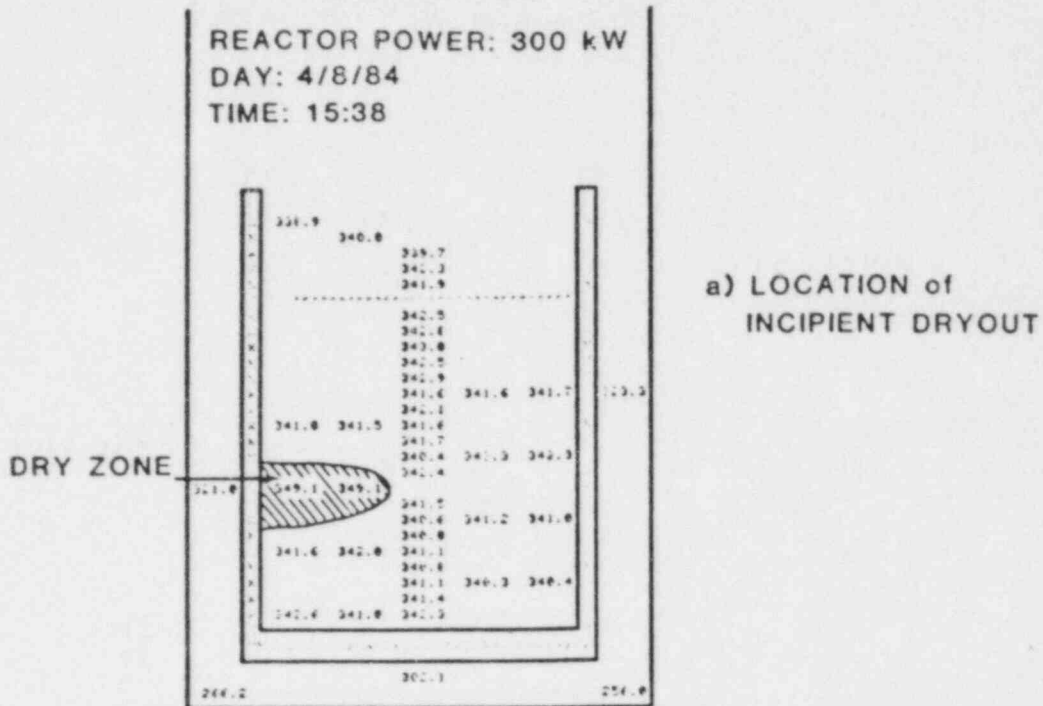


Figure 3.12 Location and Extent of Dryout #22 (DCC-2)

VAPOR PATH - - - - ->

LIQUID PATH - - - - ->

BED LEVEL ~~~~~

(NUMBERS ARE TEMPERATURE IN °C)

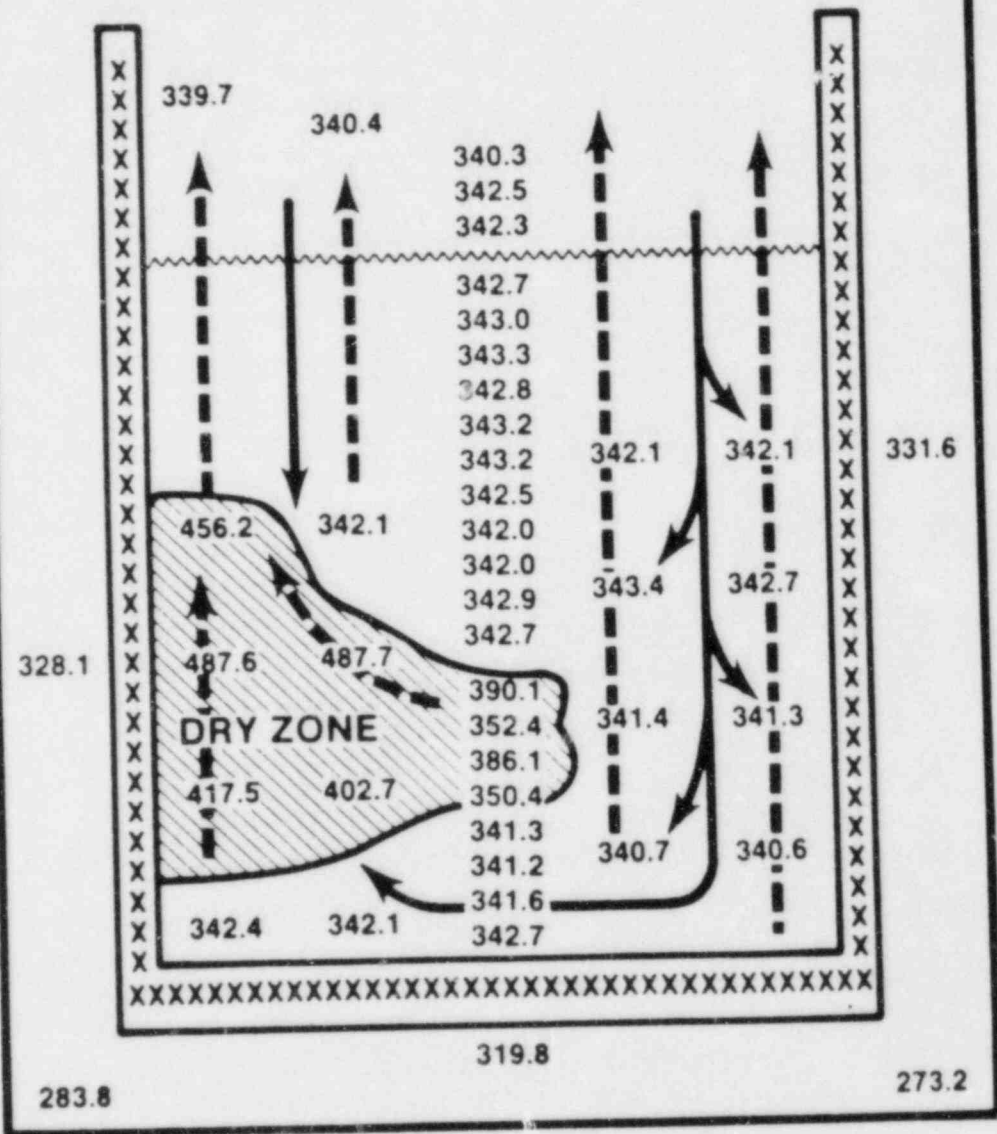


Figure 3.13 DCC-2 Local Dry Zones

On the beginning of the sixth day of operation, a second attempt was made to loosen the bed and make it more homogeneous. Two more disruptions were induced with 3 MW power steps. Pool thermocouples indicated that the bed level had not progressed to POOL-3. Subsequent local dryouts originated at the bottom at thermocouple OC if the steps in power were moderate. If the power steps were large, the dryout origin remained 4S. This was interpreted as a partial success in restructuring the bed, but the disparity in reactor power between local and global dryouts persisted.

At this time, it was noticed that the ratio between the incipient local and global dryout powers was approximately constant at 1.8. A new procedure for obtaining global dryouts was initiated. At a given pressure, the incipient dryout power was determined by gradually increasing reactor power. Once the local dryout was observed, the reactor power was increased in a large step, and the bed was examined for global dryout. The power was then reduced, and the dry zone was allowed to resaturate. If the first step in power had caused a global dryout, then a second power step, smaller than the first, was applied to the bed. Conversely, if the first step had not resulted in global dryout, the second step was made larger than the first. This procedure was repeated until the global power was bracketed to within about 10%. Data for both local and global dryouts was obtained through the eighth day of operation (Figs. 3.14-3.16).

At the beginning of the eighth day of operation, a single phase convection test was initiated. The reactor power was held at about 25 kW and the temperature distribution of the bed was examined. Fig. 3.17 shows that the temperatures in the region of OC and 4S were greater than those in the rest of the bed. This confirmed the hypothesis of a low permeability region, and showed that the disruptions were unsuccessful in eliminating it.

At the end of the eighth day, the temperature restrictions on the crucible wall were relaxed, and extended dryouts were conducted in which the fuel temperature was allowed to rise to 1050°C. This created a larger dry zone than in previous runs. The resulting quenches were thus extended, resulting in a better quench data base (Figures 3.18, 3.19, 3.20). At 15:10 on April 13, 1984, the final dryout was completed and the experiment concluded.

During the course of the experiment, the difference between the vessel pressure and the saturation pressure of the water increased. Most of the change occurred after the pre-disruption high-temperature dryouts. After this point, the minimum obtainable vessel pressure was about 4 bars. This meant that no post-disruption data for dryout could be obtained for saturation temperatures less than 145°C. It is speculated that

the source of the increased total pressure was due to the evolution of helium by the fuel. During the hot MAWP test in the experiment assembly, the fuel was exposed to 3000 psi helium at temperatures of about 250°C. This may have allowed helium to diffuse into the fuel along grain boundaries, and subsequently diffuse out of the fuel when sufficiently high temperatures were realized.

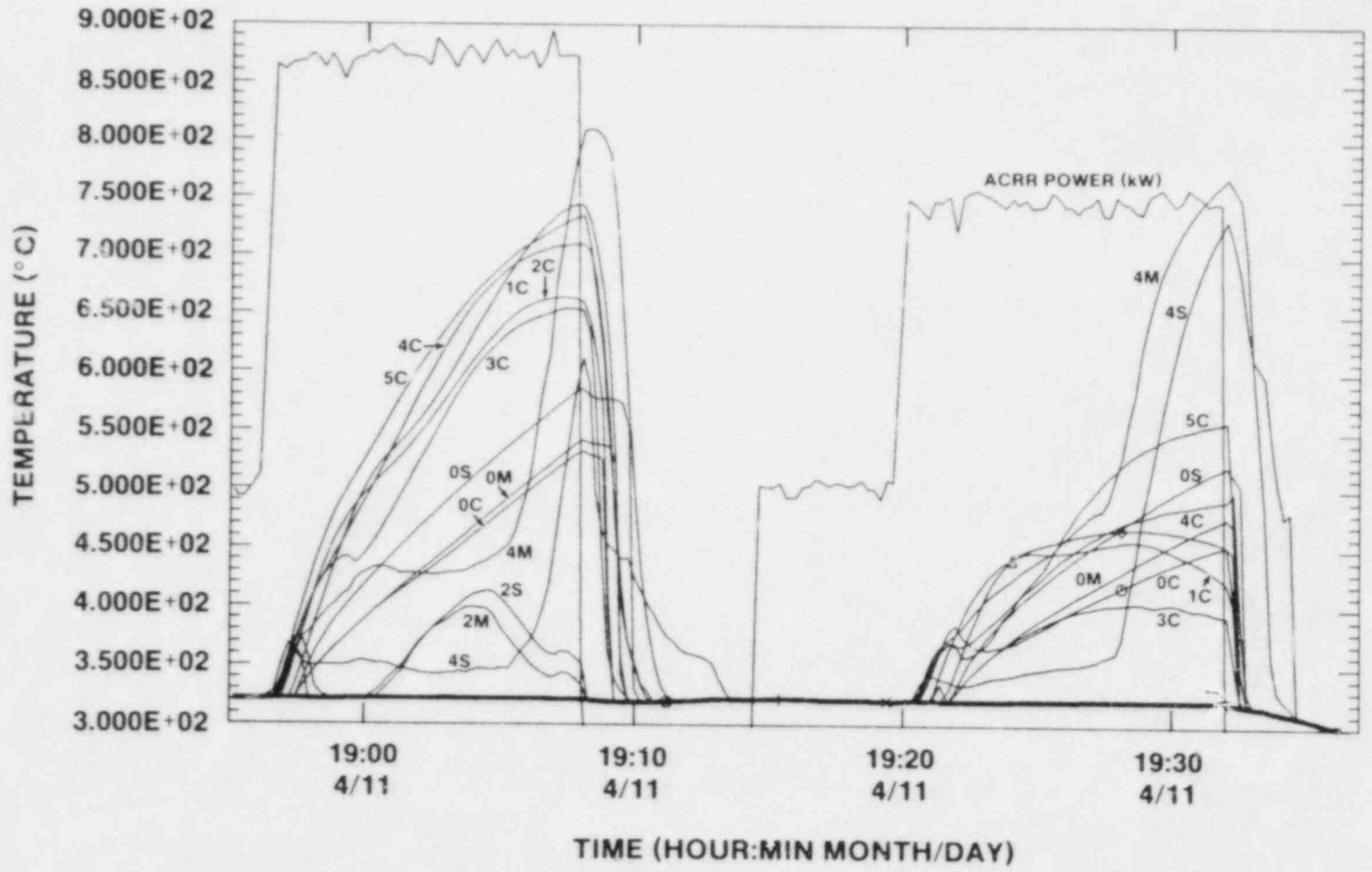


Figure 3.14 DCC-2 Dryouts #53/54, $T_{sat} = 321^{\circ}\text{C}$ (Global/Local)

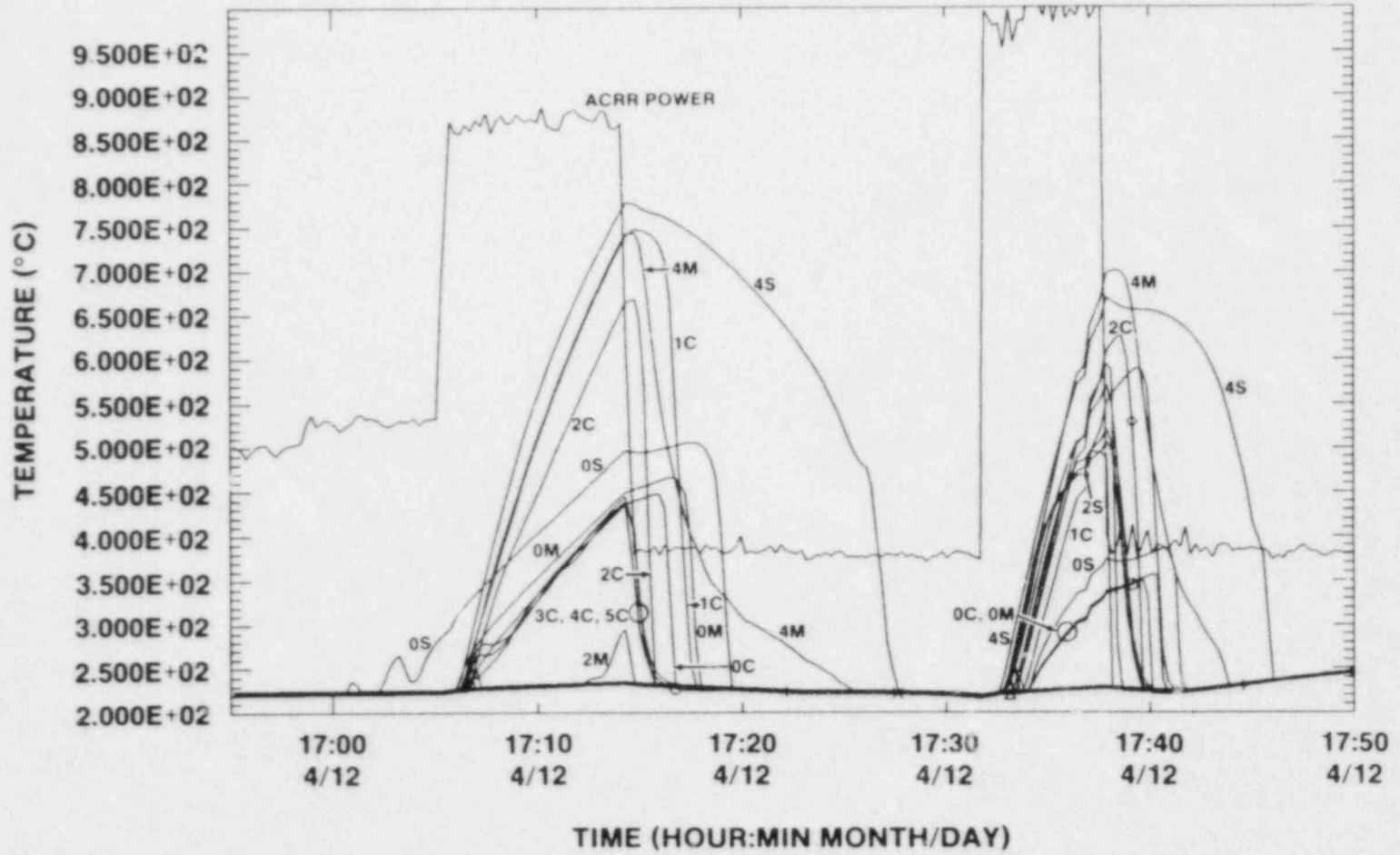


Figure 3.15 DCC-2 Dryouts #63/64, $T_{sat} = 222/221^{\circ}\text{C}$ (Local/Global)

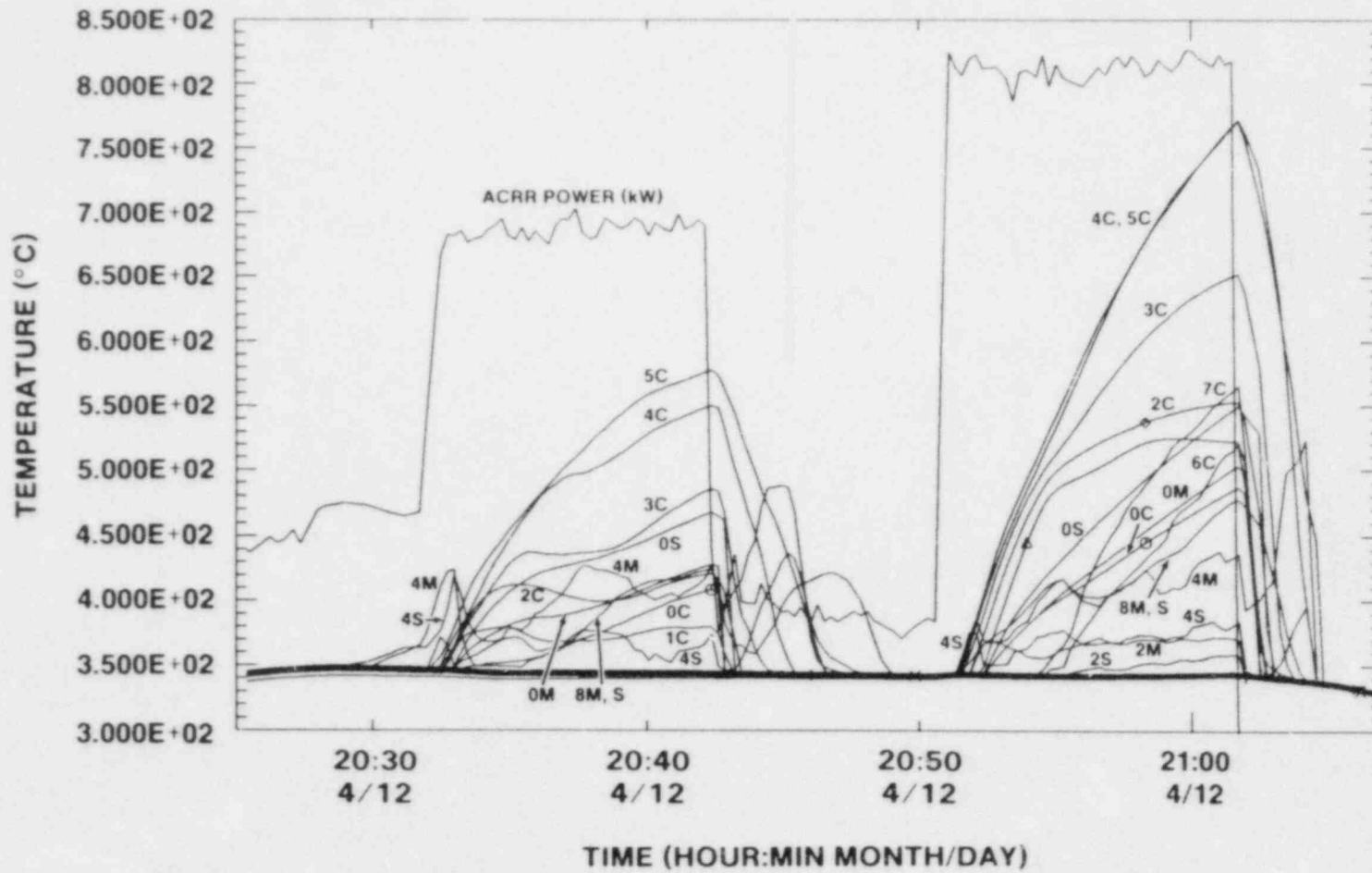


Figure 3.16 DCC-2 Dryouts #67/68, $T_{sat} = 343^{\circ}\text{C}$ (Local/Global)

REACTOR POWER : 10 kW

DAY: 4/13/84

TIME: 8:28

T_{sat} : 141 °C

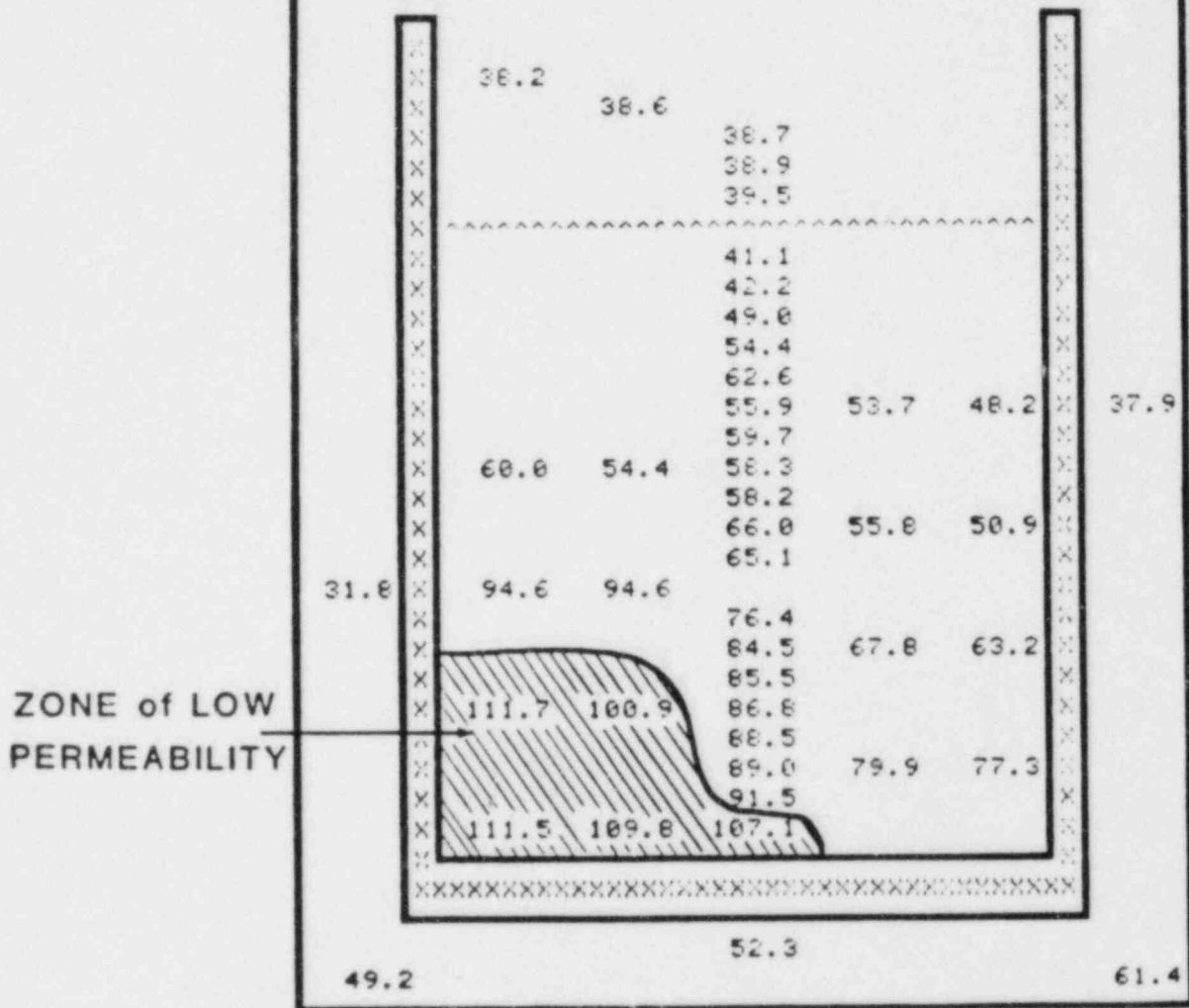


Figure 3.17 DCC-2 Natural Convection Experiment

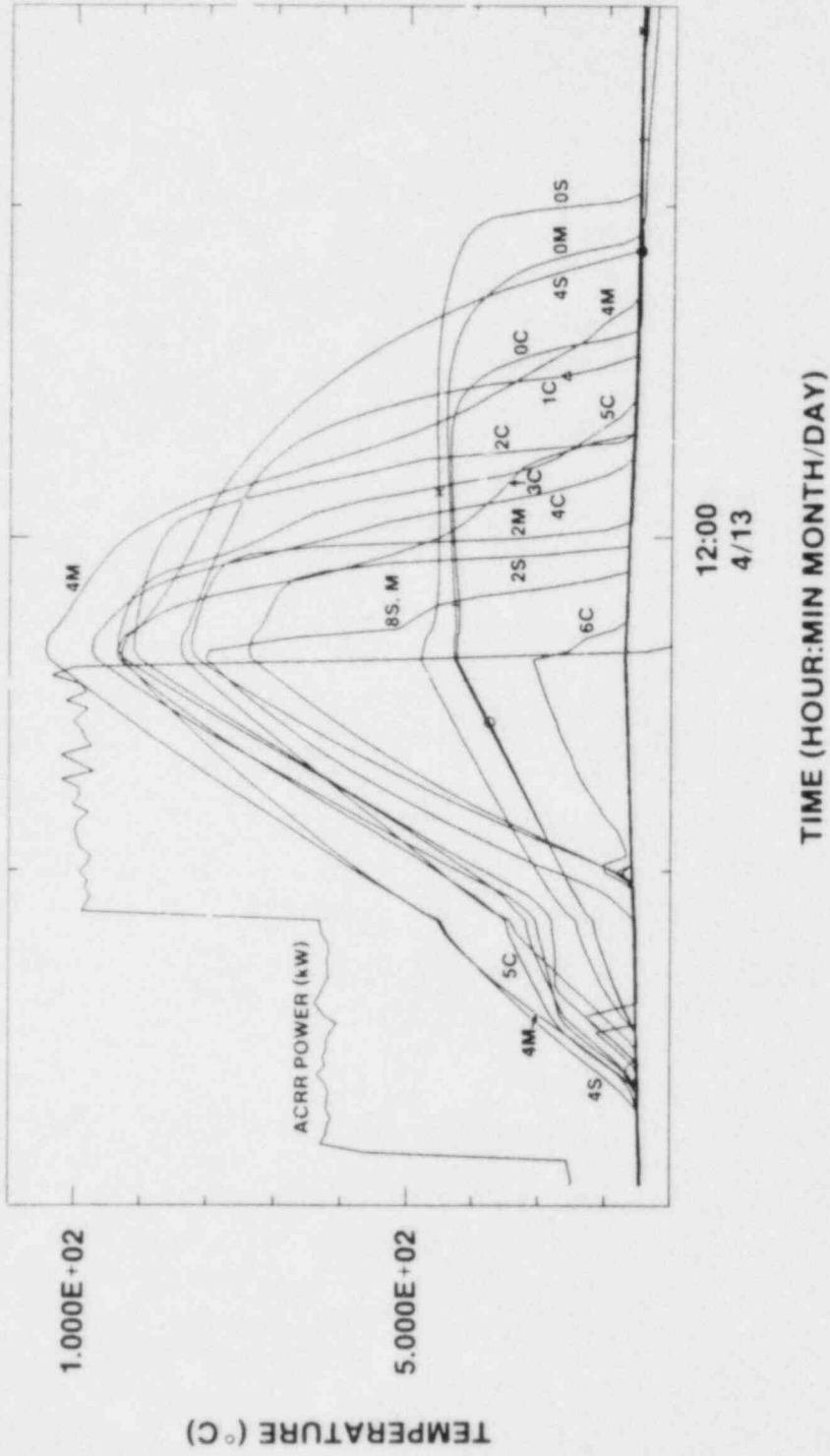


Figure 3.18 DCC-2 Dryout #70, $T_{sat} = 158^{\circ}\text{C}$ (Extended Global and Quench)

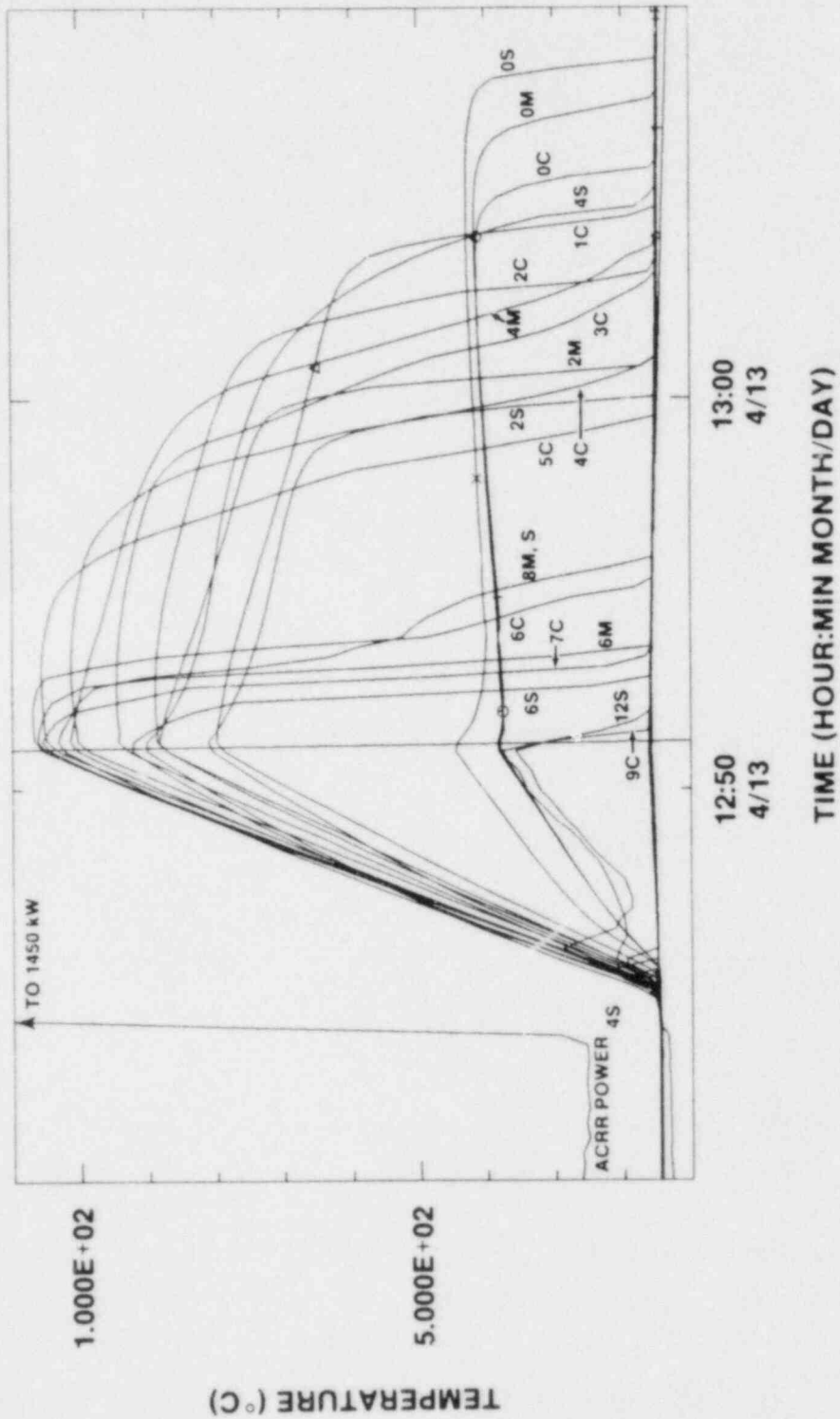


Figure 3.19 DCC-2 Dryout #71, $T_{sat} = 148^{\circ}\text{C}$ (Extended Global and Quench)

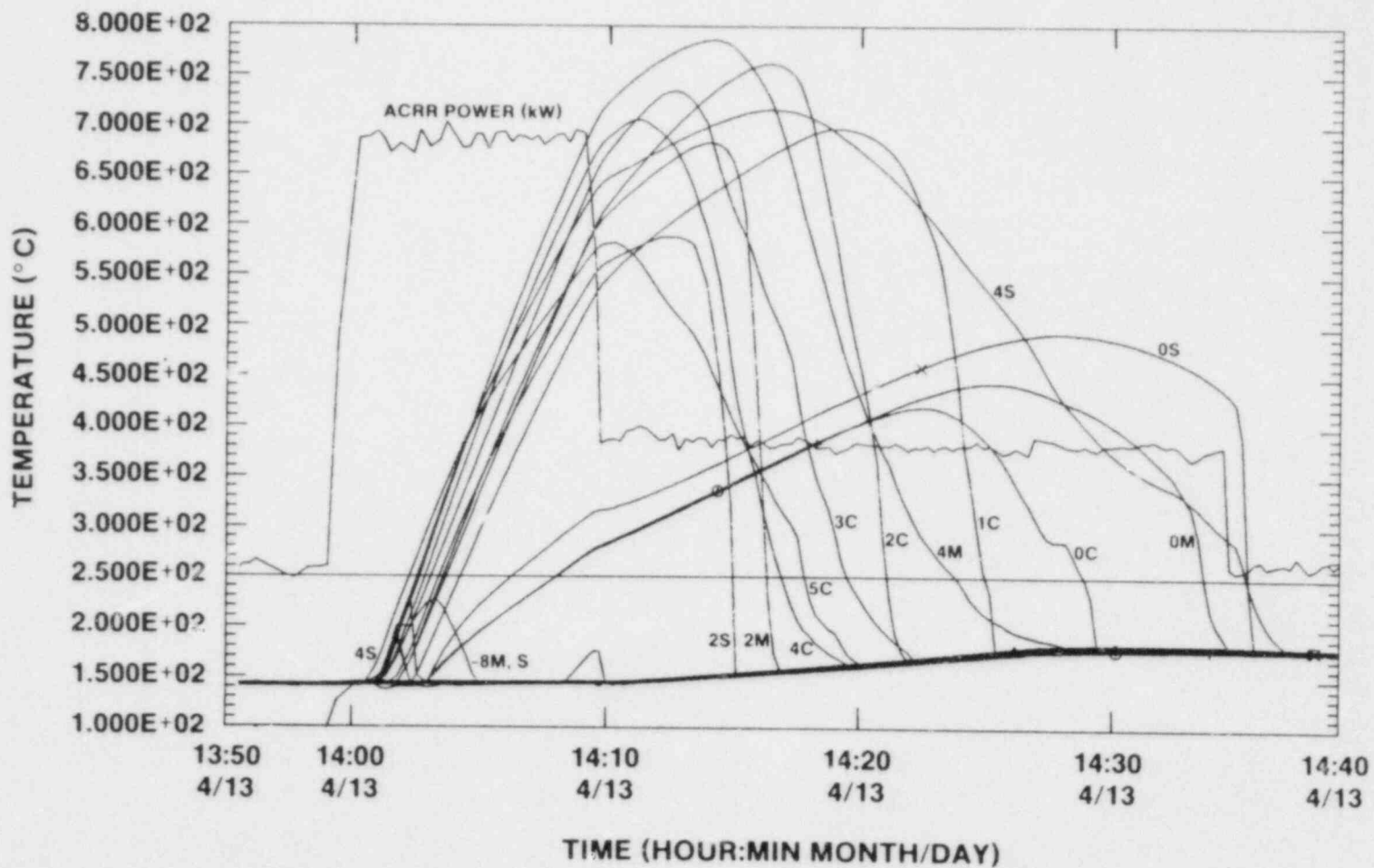


Figure 3.20 DCC-2 Dryout #72, $T_{sat} = 185^{\circ}\text{C}$ (Extended Global and Quench)

4. ANALYSIS

4.1 Bed Power Calibration

The local energy generation in the in-pile debris bed is not spatially uniform, but rather is a function of both position and saturation. (Saturation is the fraction of the bed void occupied by water.) The positional dependence stems from the axial bow in the neutron flux generated by the ACRR and the radial variation due to neutron capture. The dependence upon saturation is due to neutron moderation by the water.

The method used for bed power calibration is part experimental and part analytical. Experimentally, local power generation near a thermocouple can be measured via an adiabatic heatup. Starting from a steady state condition with constant reactor power, the reactor power is suddenly increased to a higher constant level and the thermocouple response is recorded. For a short period of time, radial conduction near the center and middle thermocouples is negligible, and the local temperature increases are adiabatic. The local power generation can then be calculated using the temperature history and material properties.

This technique is direct, but it has its limitations. There are a finite number of thermocouples in the bed, and only those sufficiently far from the outside perimeter can be used for calibration. For calibration of a dry bed, only the bottom of the bed can be dried, further limiting the number of local calibrations that can be made. For this reason, the measurements are supplemented by neutronics calculations.

Neutronics calculations of the power generation rate are made using the code TWOTRAN. [8] The accuracy of the predictions of the power level are, by themselves, not sufficient for these experiments. Table 4.1 contains the measured and predicted power generations for the centerline thermocouples in the totally saturated DCC-1 bed. While the measured specific powers are about 40% higher than those predicted by TWOTRAN, the ratio between prediction and measurement is reasonably constant except at the extreme ends of the bed. Thus, while the absolute values of power generation predicted by TWOTRAN are in error, the predicted spatial distribution of power appears to be adequate. To circumvent this problem, the predictions from the neutronics code are normalized with respect to the adiabatic heat measurements. In so doing, the accuracy of the measurements is combined with the spatial resolution of the neutronics calculations to obtain an acceptable description of the positional dependence of the power generation.

TABLE 4.1
 PREDICTED AND MEASURED SPECIFIC GENERATION
 FOR THE SATURATED DCC-1 DEBRIS BED

Thermocouple	Height (m)	Specific Power Generation (W/g/MW _{reactor})		Ratio
		Measured	Predicted	
19C	0.475	0.62	0.56	1.107
18C	0.450	0.66	0.46	1.435
17C	0.425	0.79	0.56	1.411
16C	0.400	0.87	0.64	1.359
15C	0.375	0.99	0.72	1.375
14C	0.350	1.07	0.78	1.372
13C	0.325	1.15	0.84	1.369
12C	0.300	1.22	0.88	1.386
11C	0.275	1.24	0.90	1.378
10C	0.250	1.27	0.92	1.380
9C	0.225	1.30	0.92	1.413
8C	0.200	1.30	0.82	1.413
7C	0.175	1.27	0.90	1.411
6C	0.150	1.24	0.86	1.442
5C	0.125	1.18	0.81	1.457
4C	0.100	1.10	0.74	1.486
3C	0.075	1.02	0.66	1.545
2C	0.050	0.90	0.58	1.552
1C	0.025	0.79	0.49	1.612
0C	0.0	0.36	0.38	0.947

For this analysis, the spatial description of the specific power generation, q , has been reduced from two dimensions (radial and axial) to one dimension (axial). This was accomplished by radially averaging the power generation using "first moment" integration. The resulting profile was then described using a truncated sine wave. The form of this equation is

$$\frac{q}{q_{\text{peak}}} = \sin \left[\pi \left(\frac{x + \frac{L_{\text{eff}} - L}{2}}{L_{\text{eff}}} \right) \right] \quad (4.1)$$

where L is the height of the bed, x is the distance from the bottom of the bed, and L_{eff} is the half-wavelength of the sine wave. The wavelength is calculated from the peak-to-average power ratio determined from the radially averaged neutronics calculations.

$$\frac{\bar{q}}{q_{\text{peak}}} = \frac{1}{\pi\psi} \left\{ \cos \left[\frac{\pi}{2} (\psi - 1) \right] - \cos \left[\frac{\pi}{2} (\psi + 1) \right] \right\} \quad (4.2)$$

where

$$\psi = \frac{L}{L_{\text{eff}}}$$

and \bar{q} is the bed average of the local energy generation.

For DCC-2 the peak-to-average ratio is 1.265, which yields a ψ of 0.73816. For DCC-1, the peak-to-average ratio is 1.269, which yields a ψ of 0.74286. The spatial distributions are similar because they are controlled primarily by the control rods in the ACRR.

The dependence of the power generation upon saturation is handled by assuming 1) separation of variables between position and saturation, and 2) that the local power generation is a function of the local saturation, and not the entire saturation profile. The first assumption is justified by the fact that the control rods in the ACRR control the neutron flux and that there is no feedback from the debris bed to the neutron source. The second assumption requires that the moderated neutron migration length be much smaller than the characteristic lengths of the saturation gradients in the bed. This may break down in regions where saturation gradients are large, but the assumption appears adequate for these calculations.

The saturation dependence is determined in a manner similar to that used to determine the positional dependence. During the course of the experiment, local measurements are made of the power generation at saturations of null and unity. Neutronics calculations are made for these bounding saturations and at intermediate saturations. The calculations are then normalized to the measured values. The saturation dependence of the bed average power generation is shown in Table 4.2.

TABLE 4.2
SATURATION DEPENDENCE OF BED POWER

Bed-Average Power Generation in Fuel (\bar{q})		
$\left(\frac{W/\epsilon_{\text{fuel}}}{\text{MW}_{\text{reactor}}} \right)$		
Saturation	DCC-1	DCC-2
0.0	0.585	0.530
0.2	0.684	0.648
0.4	0.779	0.755
0.6	0.872	0.846
0.8	0.963	0.914
1.0	1.043	0.960

These values have been fitted to facilitate their use in the data reduction program. For DCC-1

$$F_{\text{DCC-1}}(S) = \frac{\beta_0 + \beta_1 S}{1 + \beta_2 S} \quad (4.3)$$

where

$$F_{\text{DCC-1}}(S) = \frac{\bar{q} - 0.585}{1.043 - 0.585}$$

and the fitting coefficients (β) are:

$$\begin{aligned} \beta_0 &= 0. \\ \beta_1 &= 1.102360 \\ \beta_2 &= 0.09582610 \end{aligned}$$

For DCC-2,

$$F_{\text{DCC-2}}(S) = \frac{\beta_0 + \beta_1 S + \beta_2 S^2}{1 + \beta_3 S + \beta_4 S^2} \quad (4.4)$$

where

$$F_{\text{DCC-2}}(S) = \frac{\bar{q} - 0.530}{0.960 - 0.530}$$

and the fitting coefficients (β) are:

$$\beta_0 = 0.$$

$$\beta_1 = 1.37396$$

$$\beta_2 = -0.3103605$$

$$\beta_3 = -0.2183965$$

$$\beta_4 = 0.2834590$$

Details of the reactor calibration procedure are found in references [8,9].

4.2 Effect of Saturation-Dependent Power Generation on Bed Dryout Power

The first problem to be addressed in the reduction of the DCC-1/DCC-2 data is that of the impact of the power saturation dependence upon the bed dryout heat flux. Tables 4.3 and 4.4 contain predictions of the dryout flux using the standard Lipinski model using constant power generation. Also shown are the predictions of dryout flux made using an extended version of the Lipinski model which incorporates the information on positional and saturation dependent local power generation. Examination of the table shows little difference between the predictions; for the DCC-1 and DCC-2 configurations, the incipient dryout behavior is nearly the same as that of debris beds having a uniform power generation.

An examination of the predicted saturation profiles within a debris bed helps to explain this effect. Figure 4.1 shows several saturation profiles corresponding to several bed powers for a DCC-2 bed with uniform power generation. The saturation profiles preceding dryout share common characteristics. From the base of the channels, a large saturation gradient leads to a minimum saturation. From this point, the saturation recovers with depth in the bed. At a heat flux just above the dryout heat flux, the saturation changes radically. The region below the minimum saturation point becomes totally unsaturated; the region above remains partially saturated. Further increases in bed power result in an increase in the extent of the dry region.

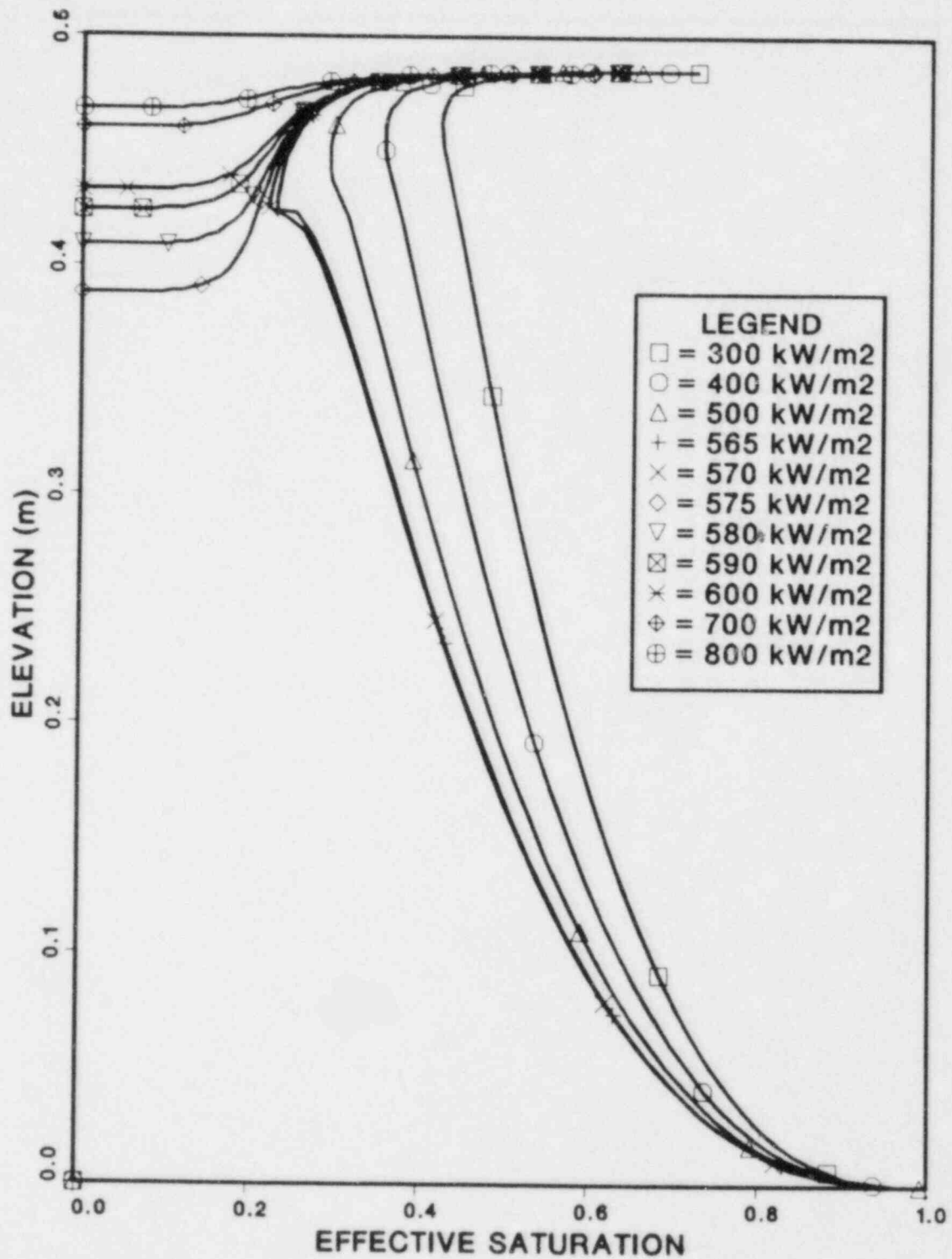


Figure 4.1 Predicted Saturation Profiles for DCC-2 at 100°C: Flat Power Profile

TABLE 4.3
DCC-1 PREDICTIONS

Saturation Temperature (°C)	DRYOUT HEAT FLUX / REACTOR POWER / (RATIO)			
	Lipinski 1-D Flat Power Profile	Lipinski 1-D DCC-1 Power Profile	Lipinski 1-D New Rel Perm	Lipinski 1-D Linearized New Rel Perm
100	36.8	35.7 / 13.1 (2.71)	25.6 / 8.68 (2.95)	39.4 / 15.0 (2.62)
120	57.3	52.0/19.0 (2.74)	37.5 / 12.6 (2.97)	52.3 / 19.6 (2.67)
140	73.5	69.9 / 25.2 (2.77)	51.7 / 17.3 (2.98)	65.3 / 24.2 (2.70)
160	94.0	90.4 / 32.6 (2.77)	66.6 / 22.2 (3.00)	78.1 / 28.1 (2.64)
180	116.5	110.4 / 39.8 (2.78)	82.4 / 27.5 (3.00)	92.4 / 35.1 (2.64)
200	137.5	130.2 / 46.9 (2.81)	98.9 / 33.0 (2.99)	104.0 / 36.8 (2.83)
220	157.3	149.0 / 52.6 (2.83)	113.4 / 37.9 (2.97)	116.8 / 40.7 (2.87)
240	174.0	166.1 / 58.8 (2.82)	126.7 / 42.6 (2.88)	128.9 / 46.1 (2.96)
260	185.5	176.7 / 62.6 (2.82)	135.2 / 47.0 (2.93)	135.3 / 45.8 (2.96)
280	185.2	176.0 / 62.5 (2.82)	136.5 / 46.6 (2.93)	136.1 / 46.4 (2.96)
300	175.1	166.3 / 59.5 (2.80)	127.6 / 43.9 (2.90)	127.1 / 43.7 (2.91)
320	149.5	143.4 / 51.6 (2.78)	110.9 / 38.6 (2.87)	110.1 / 38.3 (2.87)
340	120.0	115.8 / 42.1 (2.75)	88.1 / 42.1 (2.83)	88.5 / 31.3 (2.83)
350	103.9	99.7 / 36.5 (2.73)	76.1 / 27.2 (2.79)	77.0 / 27.6 (2.79)

TABLE 4.4
DCC-2 PREDICTIONS

Saturation Temperature (°C)	DRYOUT HEAT FLUX / REACTOR POWER / (RATIO)		
	Lipinski 1-D Flat Power Profile (kW/m ²)	Lipinski 1-D DCC-2 Power Profile (kW)	Lipinski 1-D New Rel. Perm (RATIO)
100.	575.1	552.0 / 230.5 (2.39)	545.1 / 219.7 (2.48)
120.	756.7	726.2 / 301.3 (2.41)	728.3 / 292.1 (2.49)
140.	936.0	908.0 / 375.2 (2.42)	919.0 / 371.9 (2.47)
160.	1118.	1077. / 443.5 (2.43)	1116. / 445.6 (2.50)
180.	1280.	1236. / 507.6 (2.43)	1299. / 518.6 (2.50)
200.	1433.	1388. / 570.7 (2.43)	1471. / 587.8 (2.50)
220.	1544.	1505. / 619.1 (2.43)	1622. / 649.9 (2.50)
240.	1651.	1600. / 660.5 (2.42)	1720. / 691.0 (2.49)
260.	1678.	1632. / 675.4 (2.42)	1782. / 729.7 (2.44)
280.	1651.	1621. / 675.0 (2.40)	1792. / 728.8 (2.46)
300.	1571.	1552. / 650.7 (2.39)	1712 / 701.6 (2.44)
320.	1435.	1395. / 589.6 (2.37)	1546. / 639.9 (2.42)
340.	1191.	1169. / 499.2 (2.34)	1296. / 543.3 (2.39)
350.	1046.	1026. / 440.4 (2.33)	1149. / 485.3 (2.37)

This behavior suggests that the critical condition for dryout is located at the point of minimum saturation. Through this "throat" passes the liquid which cools the lower portion of the bed and the vapor which is produced there. Dryout occurs when the liquid and vapor fluxes required to cool the lower portion of the bed can no longer satisfy the momentum equation. This explains why the dryout heat flux for deep beds is independent of bed depth. The maximum permitted liquid and vapor fluxes in the throat are integral quantities of the bed below the throat. As long as the throat is sufficiently far from the bottom, these maximum quantities represent constraints that are local in nature, and are independent of the region below the bed.

The same argument that explains the independence of deep bed dryout power to bed depth applies to the problem of saturation dependence. Since, for deep beds, the constraints at the throat are local conditions, the form of the power profile below the throat is relatively unimportant. All that counts is the integral of that profile over the distance between the bottom and the throat. Fig. 4.2 shows that the saturation profiles predicted for the DCC-2 power profile are about the same as those for the flat power profile. The location of the throat and the saturation in the throat are about the same. The dryout power appears unaffected by the power profile.

Because of the increased importance of capillarity, the saturation profiles for DCC-1 are more complicated than for DCC-2. For flat power profiles and bed powers below about 30 kW/m^2 , the throat remains in the upper third of the bed (Fig. 4.3). However, beyond about 80% of dryout power, the throat migrates into the lower half of the bed. This same behavior is predicted for the DCC-1 power profile (Fig 4.4). This suggests a potential dependence upon power profile in the dryout powers which is not observed in the experimental data. The reason for the lack of dependence can be found in the nature of the power profile. In the spatial component of the power, the peak power is about twice the value of the power at the ends. The saturation at the ends, however, is about twice that near the middle. The enhancement of the power near the ends due to the higher saturation offsets the variation in the spatial component. The net effect is a reasonably flat power profile. Thus, the total dryout power in DCC-1 is unaffected by the power profile, even though the throat migrates.

One interesting aspect of saturation dependence in the power generation is that there is a range of reactor powers beyond incipient dryout for which there is no one-dimensional steady state solution to the momentum/energy equations for a debris bed. The reason for this can be seen by examining the variation of the saturation profiles with reactor power (Figs. 4.2, 4.4). Up until incipient dryout is reached, the bed power

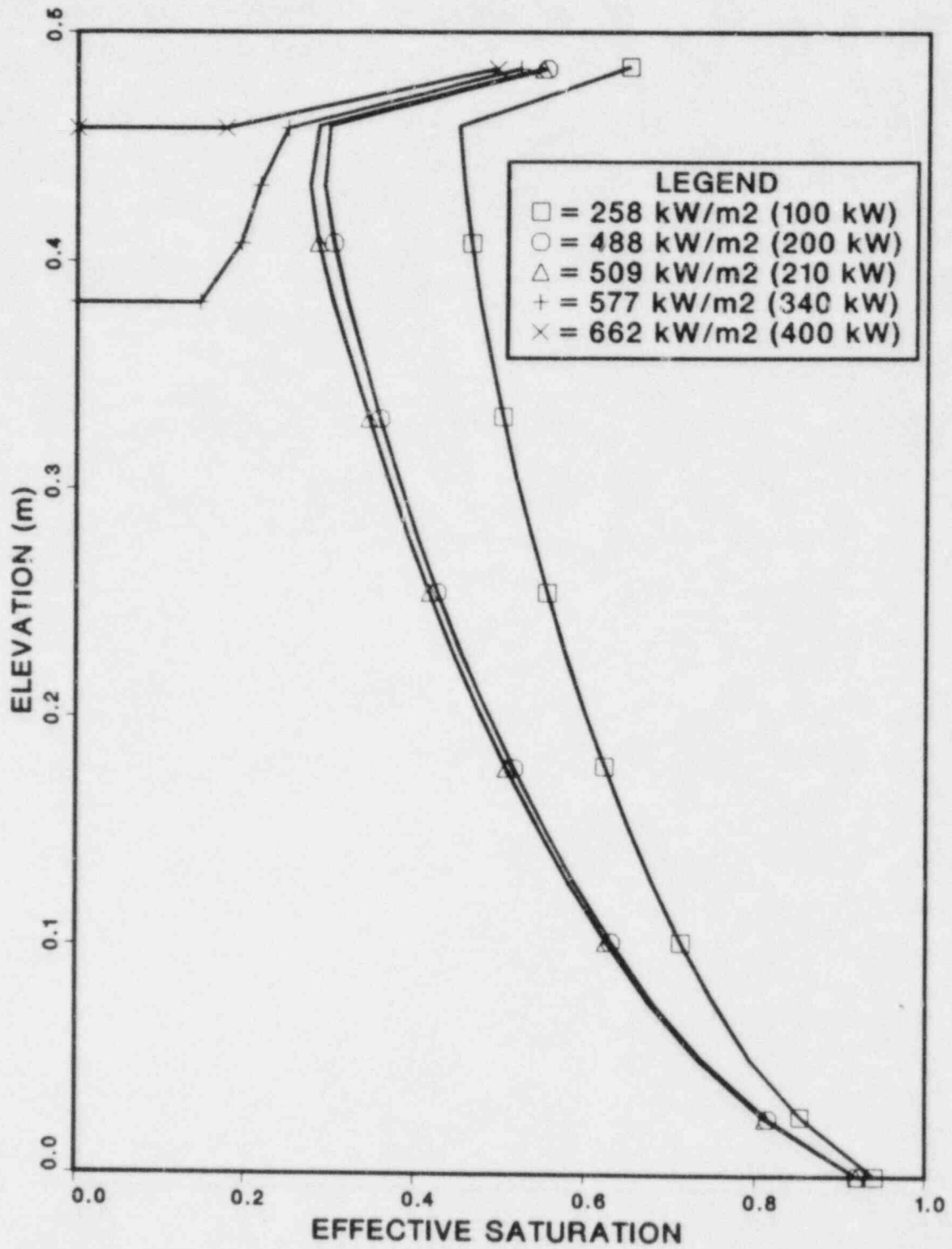


Figure 4.2 Predicted Saturation Profiles for DCC-2 at 100°C: DCC-2 Power Profile

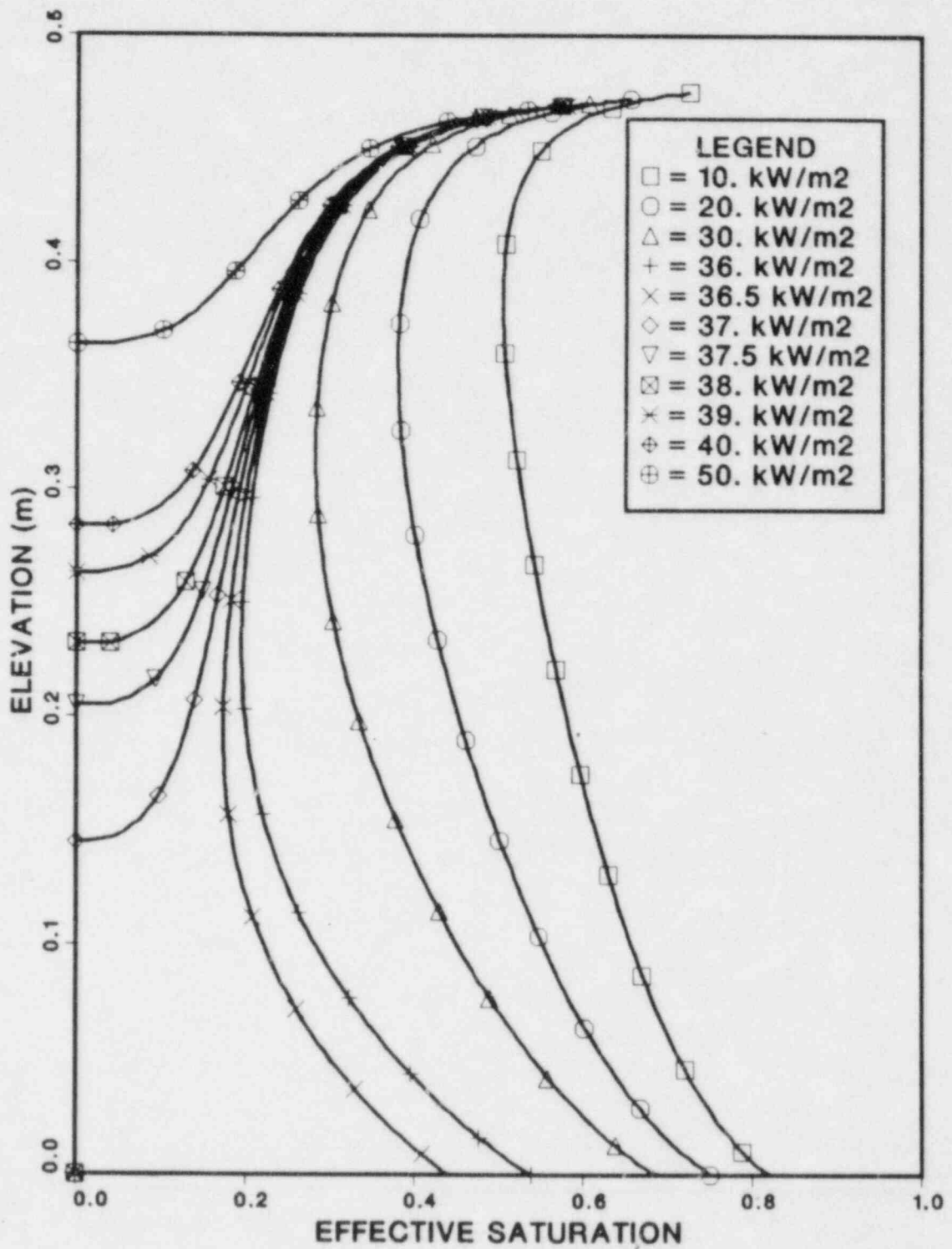


Figure 4.3 Predicted Saturation Profiles for DCC-1
(at 100°C: Flat Power Profile)

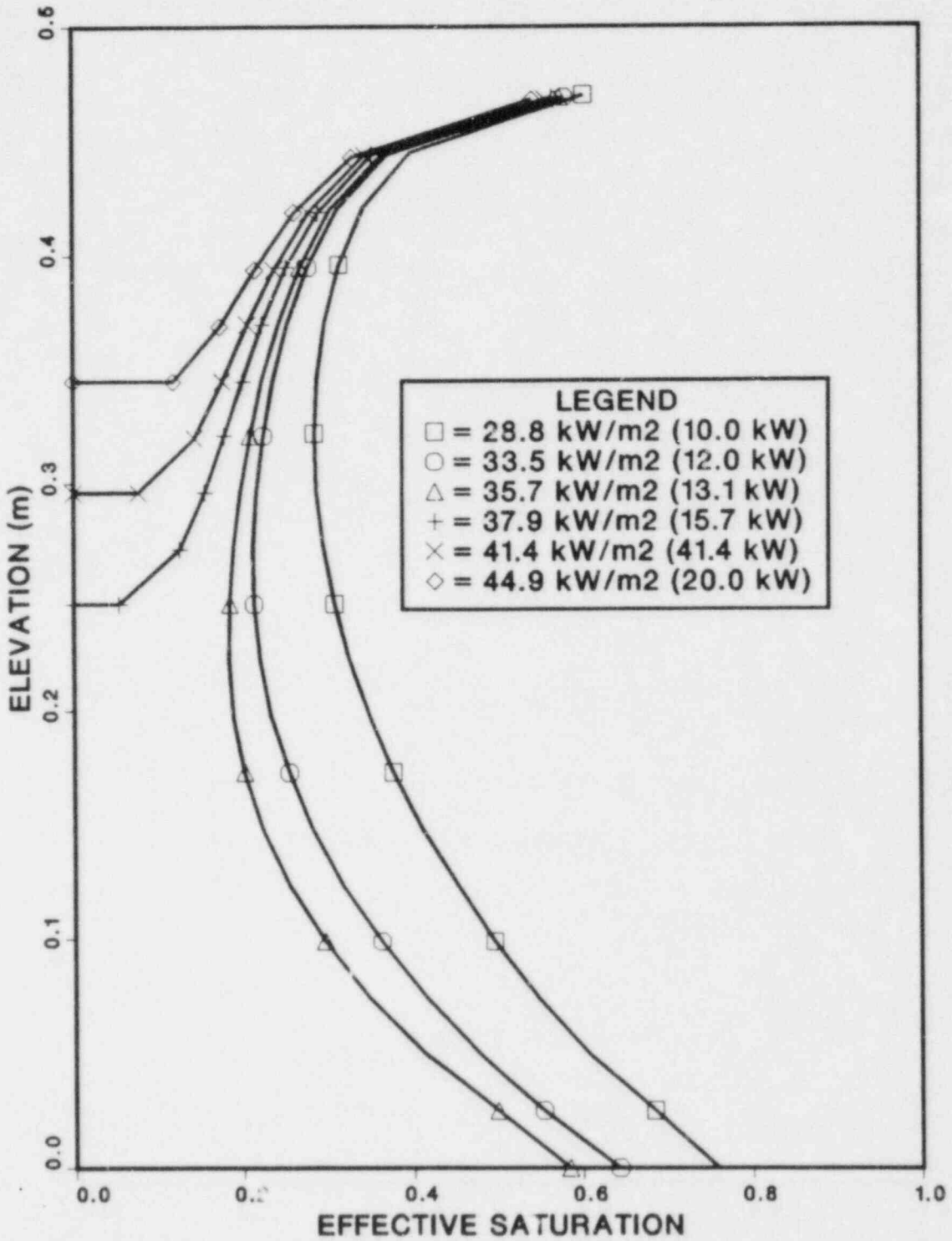


Figure 4.4 Predicted Saturation Profiles for DCC-1 at 100°C: DCC-1 Power Profile

varies smoothly with reactor power. Because the average saturation of the bed decreases with increasing bed power, the relationship between reactor and bed powers is not quite linear (Fig. 4.5).

As for a bed with uniform power generation, the saturation profile changes drastically when the bed power is increased slightly above the incipient dryout level. Because the region below the throat is now dry, the reactor power corresponding to this slight increase in bed power must be substantially larger than the reactor power at incipient dryout (Fig. 4.5). The amount of this jump in reactor power is dependent upon the magnitude of the saturation dependence and the relative effect of capillarity upon saturation profiles. Attempts to determine the saturation profile at intermediate reactor powers result in an inability to satisfy both the energy and the momentum equations simultaneously. From this, one can conclude that no steady-state one-dimensional solution to the cooling equations exists. This means that the flow must either have a periodic solution or be two-dimensional for these intermediate reactor powers. The question is somewhat academic to the experiments at hand. None of the post incipient dryout conditions experimentally achieved are ever steady. For the purpose of this analysis, the reactor powers at incipient dryout are those which will be used for comparison against the experimental data.

4.3 Data Reduction

Because the power generation is partially dependent upon the local saturation, the conversion from reactor power to total bed power is, to some extent, dependent upon the model used to describe boiling in debris beds. Three potential methods of data reduction are described here. The choice of method is based upon mathematical validity and minimization of the dependence of the result upon the model.

The first possibility is simply to input the measured reactor power into the debris code to determine the corresponding bed power. The problem with this is that the saturation profile would be obviously wrong. Consider the plot of predicted saturation profile for different reactor powers (Figs. 4.2, 4.4). If the measured reactor power were less than the predicted incipient dryout power, the code would predict a saturation profile inconsistent with dryout. The higher saturations would result in an overprediction of bed power. If the measured reactor power were greater than the predicted dryout power, the problem would be worse. Spanning the region of reactor power without a steady state one-dimensional solution (Fig. 4.5, Section B), a large change in reactor power results in a small change in bed power. This is strictly a result of the predicted post dryout saturation profile, which is not

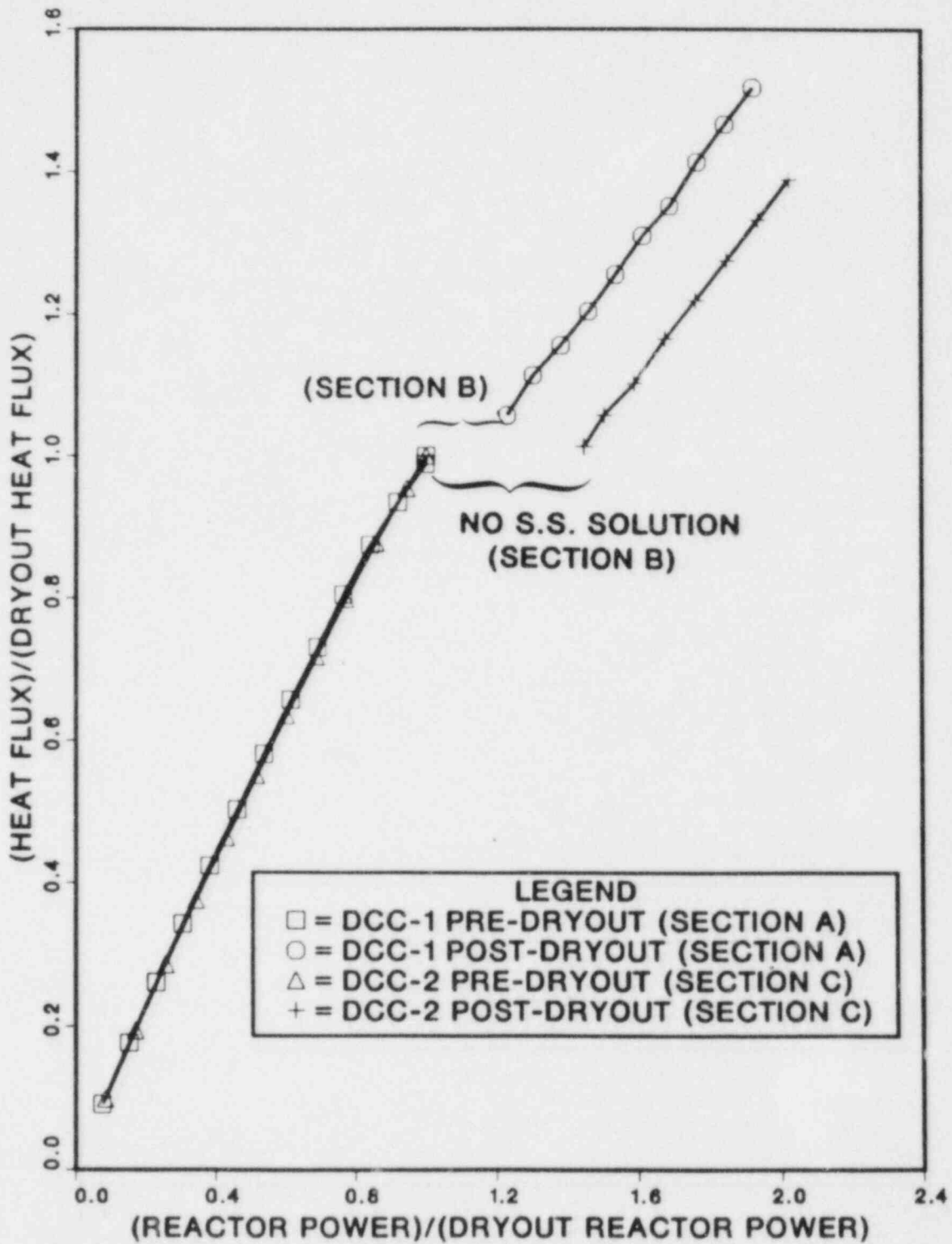


Figure 4.5 Non-dimensional Bed Power Calibration at 100°C

actually realized in the experiment. The result would be that the reduced bed power corresponding to the measured reactor power would be unrealistically close to the bed power predicted by the model. This procedure would make the reduced bed powers too dependent upon the model.

The second technique is to use the code to compute an average saturation, and then to use the reactor calibration (Fig. 4.5, Section A) to compute total bed power. Unfortunately, this cannot be justified mathematically. The total bed power can be written as the spatial integral of the product of the spatial component and the saturation component. This is not equal to the product of the average spatial component and the average saturation component. This is because the bed power is dependent upon the saturation distribution, and not just the average saturation.

The third technique is to assume that the predicted saturation profile at incipient dryout is that which actually occurs in the experiment. Under this assumption, the conversion from reactor power becomes a simple one of ratios:

$$\frac{Q_{DO}}{P_{\text{reactor}}} \Big|_{\text{exp}} = \frac{Q_{DO}}{P_{\text{reactor}}} \Big|_{\text{pred}} \quad (4.5)$$

This technique avoids the problem of data compression associated with the first option and circumvents the averaging problem of the second option. There is, nevertheless, an obvious error associated with it. The actual saturation profile must be different than the predicted profile if the measured reactor power is different than the predicted reactor power. In the absence of measured saturation profiles, this problem cannot be avoided. In spite of the problem, this method provides a reasonable and consistent method of interpolating between the limiting bounds corresponding to totally saturated and totally unsaturated beds.

There are two interesting aspects associated with this last data reduction technique. The first is that the ratio of predicted bed dryout power and predicted reactor dryout power is very nearly constant over the entire temperature range of the experiment (Tables 4.2, 4.3). This can be explained as the result of two compensating effects. As the temperature increases, the density of the liquid decreases, and the corresponding thermalization of neutrons decreases because of the lower hydrogen density. By itself, this would predict a

decrease in the bed power/reactor power ratio. Countering this trend is the hydrodynamic prediction that the average saturation at dryout increases with increasing saturation temperature. These two competing effects are sufficiently well balanced in DCC-1 and DCC-2 that the predicted bed power/reactor power ratio is almost constant.

The second aspect of the reduction technique is that, for the range of variation in models examined, the ratio between bed power and reactor power varies by at most 13%, even though the predicted dryout powers vary by 50% (Table 4.2). This suggests that the data reduction technique is not very sensitive to the model itself, and adds credence to the claim that the reduced bed powers are reasonable.

4.4 DCC-1 Dryout Data

Reduced dryout powers for DCC-1 are contained in Table 4.5. The pressure dependence of the DCC-1 dryout heat flux data is shown in Fig. 4.6. Near one atmosphere pressure, the dryout heat fluxes are best predicted by the Lipinski [6] and Henry [17] models. At higher pressures, the Jones [13,14], Dhir-Catton [11], and Lipinski [6] models work best. With the exception of the Theofanous-Saito model [10], all the models overpredict the dependence on pressure. The variable power Lipinski model predicted a ratio between the maximum dryout flux and the dryout flux at one atmosphere of about 5, compared to the measured value of 1.9. While the Theofanous-Saito model comes closer to predicting the pressure dependence, it overpredicts the dryout fluxes by an order of magnitude. This is because it is based on flooding data, and is therefore inappropriate for small particle beds.

Figure 4.6 shows the difference between the Lipinski 0-D model for uniform heat generation and the one-dimensional calculation which includes the spatial and saturation dependencies of the heat production. The 1-D prediction is slightly greater than the 0-D prediction and has a slightly different pressure dependence, but the net result is a disparity in the pressure dependence.

The probable cause of the disparity between the predictions and the measurements is the breadth of the particle size distribution coupled with the depth of the bed. Most of the world data are based upon beds composed of narrow particle size distributions. It is therefore consistent to expect predictive models to work better for narrow distributions than for broad distributions.

TABLE 4.5
 REDUCED DCC-1 INCIPIENT DRYOUT POWERS

Dryout Number	Saturation Temperature (°C)	Reactor Power (kW)	Bed Power (kW/m ²)
2	101	15-16	40.8-43.6
4	107	14-16	38.4-43.9
5	122	16-17	43.8-46.6
6	141	15-17	41.4-47.0
7	160	17-19	47.1-52.7
8	180	18-20	50.6-56.2
9	202	21-24	59.0-67.4
11	222	24-25.5	67.9-72.2
12	240	27-28.5	76.3-80.6
13	261	27-28.5	76.2-80.4
14	280	25.5-27	71.8-76.0
15	300	25.5-27	71.3-75.5
16	323	24-25.5	66.6-70.8
17	342	24-25.5	65.9-70.0
18	353	24-25.5	65.5-69.6
21	151	14-16	38.8-44.4
23	220	24-25.5	67.9-72.2
24	303	27-28.5	75.5-79.7
25	322	25.5-27	70.8-75.0
26	342	24-25.5	65.9-70.0
28	224	24-25.5	67.8-72.1
30	133	14-16	38.7-44.2
31	104	14-16	38.5-44.0
32	122	15-16	41.1-43.8
33	141	16-17	44.2-47.0
36	141	15-17	41.4-47.0
38	223	25.5-27	71.9-76.2

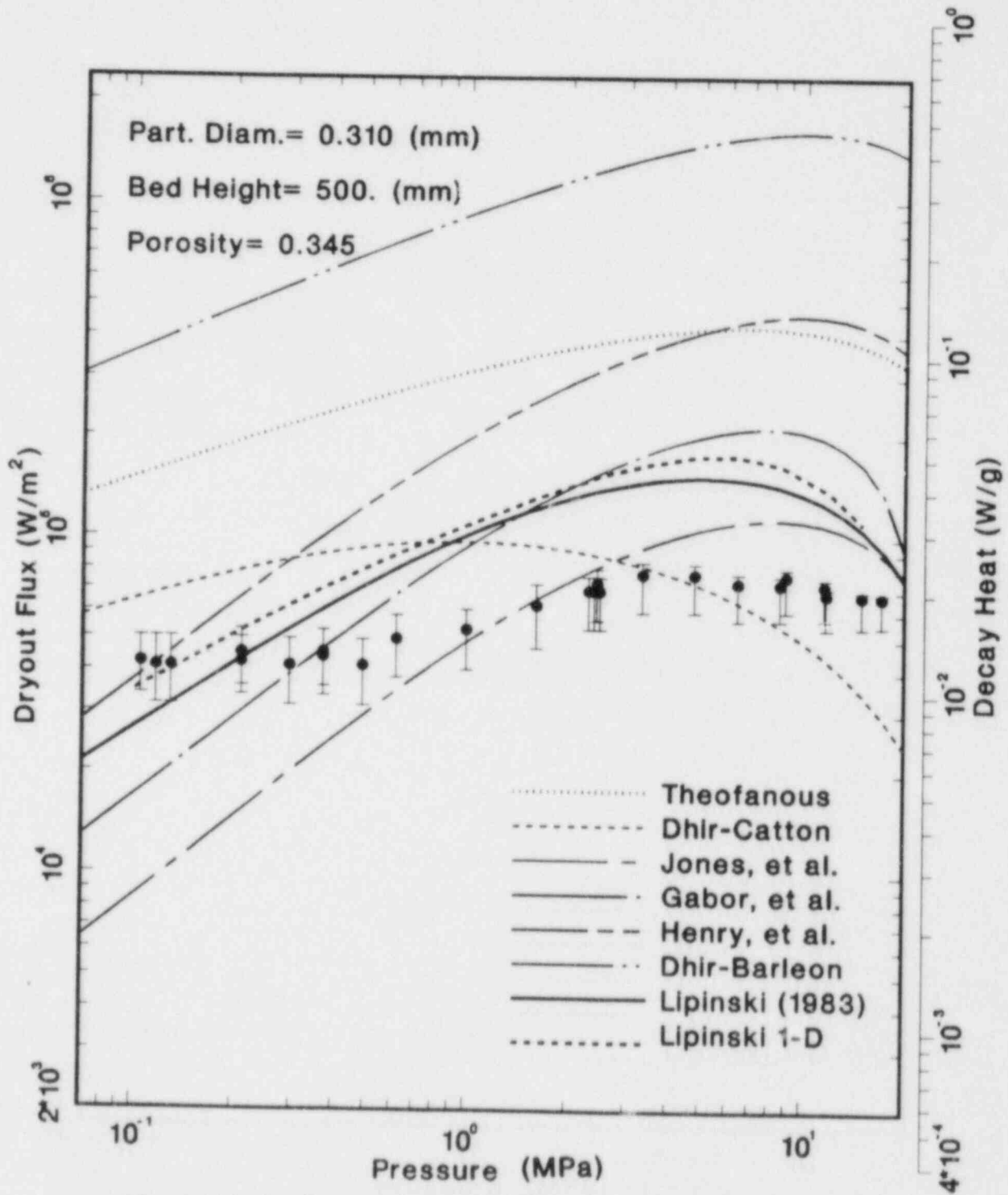


Figure 4.6 Comparison of DCC-1 Dryout Data with Predictive Models

A limited amount of dryout data has been obtained for beds with broad size distributions, but these have involved beds less than 16 cm high cooled with sodium. [19] In these tests, the effect of channels and capillary pressure greatly influence the dryout phenomena. In beds such as DCC-1, the capillary pressure does not dominate the boiling phenomena and the effect of channels is insignificant. Instead, the dryout phenomena is dominated by the momentum transport in each phase, as described by the relative permeability curve.

Ideally, one would measure directly the relative permeabilities of a simulated DCC-1 bed as well as on a bed having the same effective particle diameter, but having a narrow distribution. The results of each could then be used in a 1-D model to assess expected differences in the dryout behavior. Unfortunately, such measurements are difficult to conduct, and are beyond the scope of the present study.

What is accessible is to assess the validity of the approach which led to the currently used models for relative permeability, and to look for expected differences between DCC-1 and more common bed configurations. The currently used relative permeabilities were deduced using the Brooks and Corey correlation [4,5] and Leverett's data [20] for capillary pressure in sands. The Brooks and Corey correlation relates the liquid and vapor laminar relative permeabilities to the capillary pressure/saturation behavior of a porous material. This approach was extended by Reed [21] to describe turbulent relative permeabilities. Leverett's capillary pressure correlation was based on data for fairly narrow distributions of sand having diameters less than 200 microns. The results of these calculations were then fitted with a power law to make the O-D model more manageable. The final result was:

$$\begin{aligned}
 k_l &= S_{eff}^3 \\
 k_v &= (1-S_{eff})^3 \\
 \kappa_l &= S_{eff}^5 \\
 \kappa_v &= (1-S_{eff})^5
 \end{aligned}
 \tag{4.6}$$

In order to obtain some idea of the applicability of the Leverett correlation to UO₂/water systems, measurements were made of the capillary pressure of several UO₂/water beds in which particle size and size distribution were varied. [22] Figure 4.7 shows a comparison of the measured non-dimensional capillary pressures for narrow particle size distributions and the Leverett correlation. The agreement between the two is good, even though the data base has been expanded to diameters in excess of 1 mm.

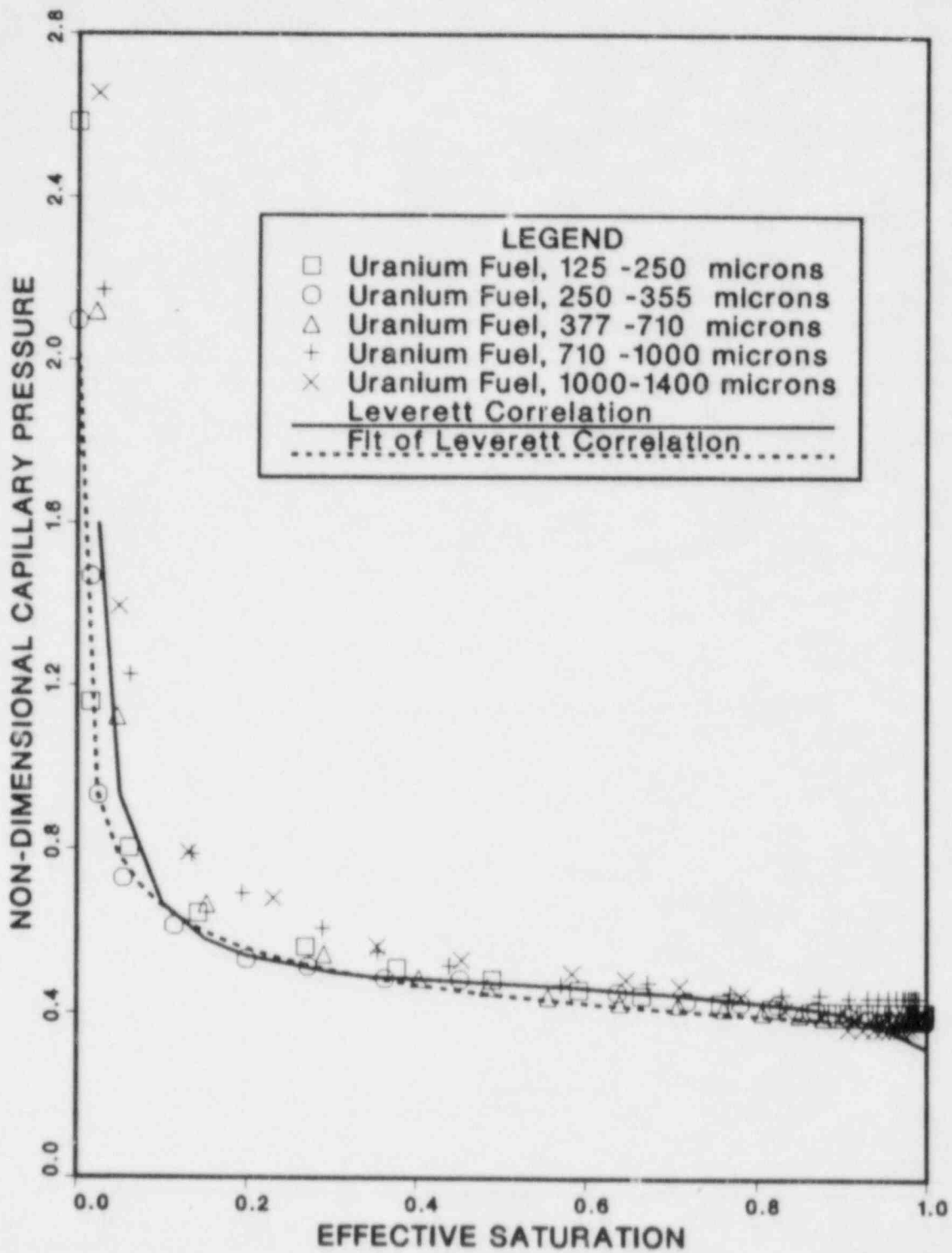


Figure 4.7 Non-dimensional Capillary Pressure for Narrow Size Distributions

The agreement does not extend to the capillary pressure measured for DCC-1 (Fig. 4.8). The difference between the Leverett correlation and the DCC-1 data sheds light on differences in microscopic geometry. The Leverett function is relatively flat over a wide range of saturation, and rises only at small saturations. This means that the pores within the media are reasonably uniform in size, with a comparatively small population of small pores. Because the water is the wetting phase, it preferentially occupies the smaller pores. The uniformity of the pore size distribution implies that there should be little difference in the hydraulic diameters of the liquid and vapor phases. This is reflected in the symmetry of the relative permeabilities of the wetting and non-wetting phases.

The DCC-1 data demonstrates a shape very different than that of the Leverett correlation. The non-dimensional breakthrough pressure is 2-3 times lower than that for uniform particles, but the capillary pressure increases constantly as the saturation is decreased. This means that the pore size distribution is comparatively broad, and that, for a given saturation, the hydraulic diameter for the liquid phase will be less than that of the vapor phase. This should result in an asymmetry in the wetting and non-wetting permeabilities.

These rudimentary concepts of preferential phase occupation and pore diameter are the basis of Brooks and Corey's semi-empirical correlation for laminar relative permeability. The relationships they derived are:

$$k_l = S_{eff}^{3+2b}$$

$$k_v = (1 - S_{eff})^2 (1 - S_{eff}^{1+2b}), \quad (4.7)$$

where the capillary pressure has the form

$$p_c = a S_{eff}^{-b} . \quad (4.8)$$

The extension derived by Reed for turbulent relative permeability is:

$$\kappa_l = S_{eff}^{5+b}$$

$$\kappa_v = (1 - S_{eff})^3 (1 - S_{eff}^{1+b/2}) \quad (4.9)$$

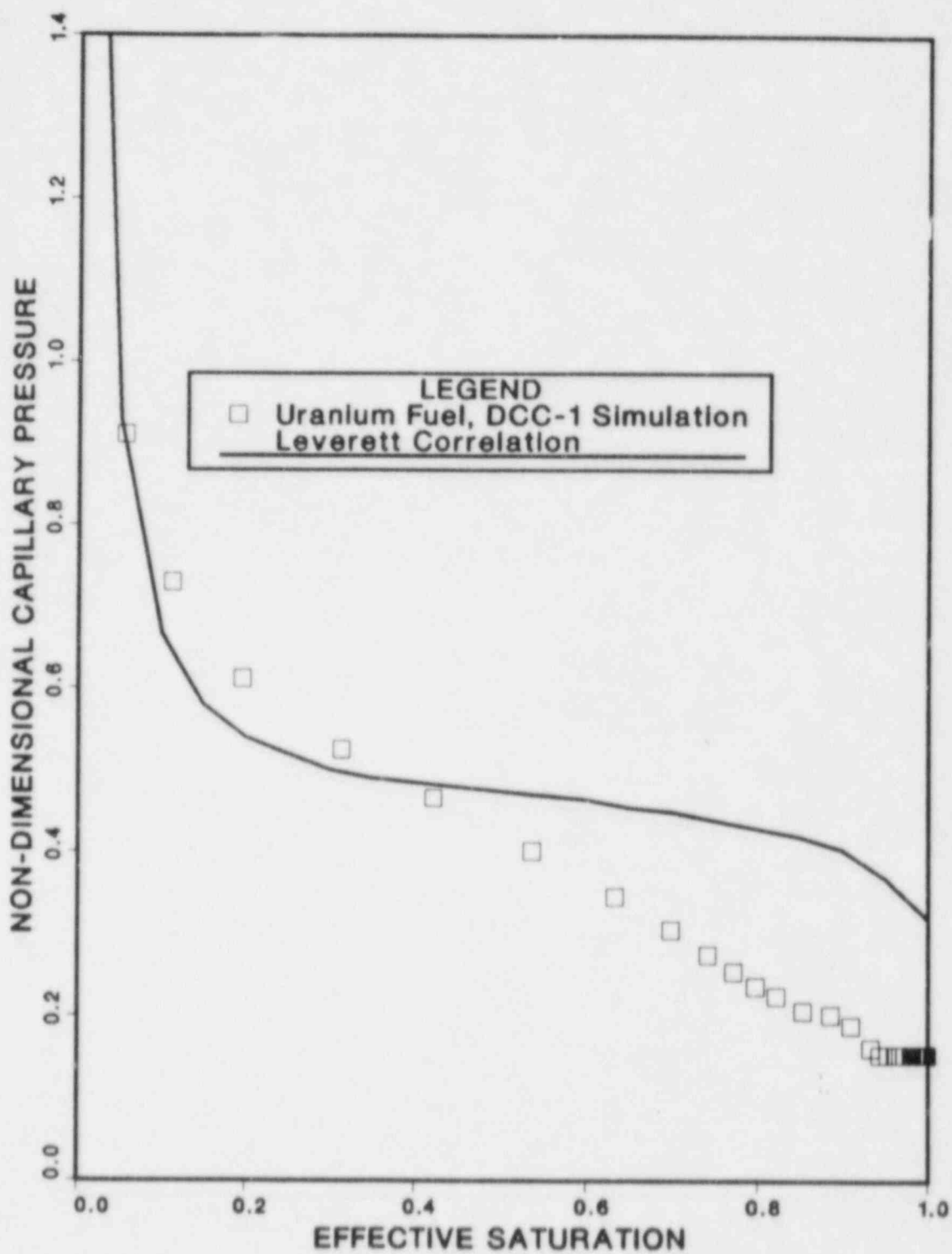


Figure 4.8 Non-dimensional Capillary Pressure for DCC-1 Bed

The application of these formulae to the measured capillary pressure data is seen in Figures 4.9 and 4.10. The solid lines are the models currently used in the Lipinski model (Equation 4.6). The relationships closest to those are derived from the Brooks and Corey formula and a curve fit of the Leverett correlation

$$J(S) = 0.3771 S_{eff}^{-0.243} \quad (4.10)$$

There is little difference between these two models for relative permeability.

The third set of curves were derived by using the measured DCC-1 capillary pressure data in the Brooks and Corey relationships. The data was used without fitting and the integrations were executed numerically. The laminar relative permeabilities derived in this manner display significant differences from the currently used models. While the vapor laminar permeability appears to increase by about 30%, the major difference seems to lie in the liquid laminar permeability, which drops by more than half. The variation in the models of turbulent relative permeability is comparatively small. The total elimination of the turbulent term for DCC-1 results in an increase of about 20% in the predicted dryout fluxes with little change in the pressure dependence. This suggests that the attention should be concentrated on the laminar terms.

The effect that these alternate relative permeabilities have on the predicted dryout heat flux is seen in Figure 4.11 (also Table 4.2). The net effect is to shift the prediction downward without modifying the pressure dependence significantly. This model, however, displays an interesting sensitivity which is not present in the Lipinski values. The liquid laminar relative permeability is small between the effective saturations of 0.0 and 0.4 (Fig. 4.9). If the liquid permeability is made to vary linearly between these two saturations, the predicted pressure dependence decreases (Fig. 4.11). While this is still greater than the effect observed in the data, it does suggest the observed trend.

The legitimacy of the suggested change in liquid relative permeability must be considered with reference to the data base of the Brooks and Corey correlation. In their work, the capillary pressure data was fitted with the equation form

$$\frac{P_c}{P_{c,b}} = S_{eff}^{-b} \quad (4.11)$$

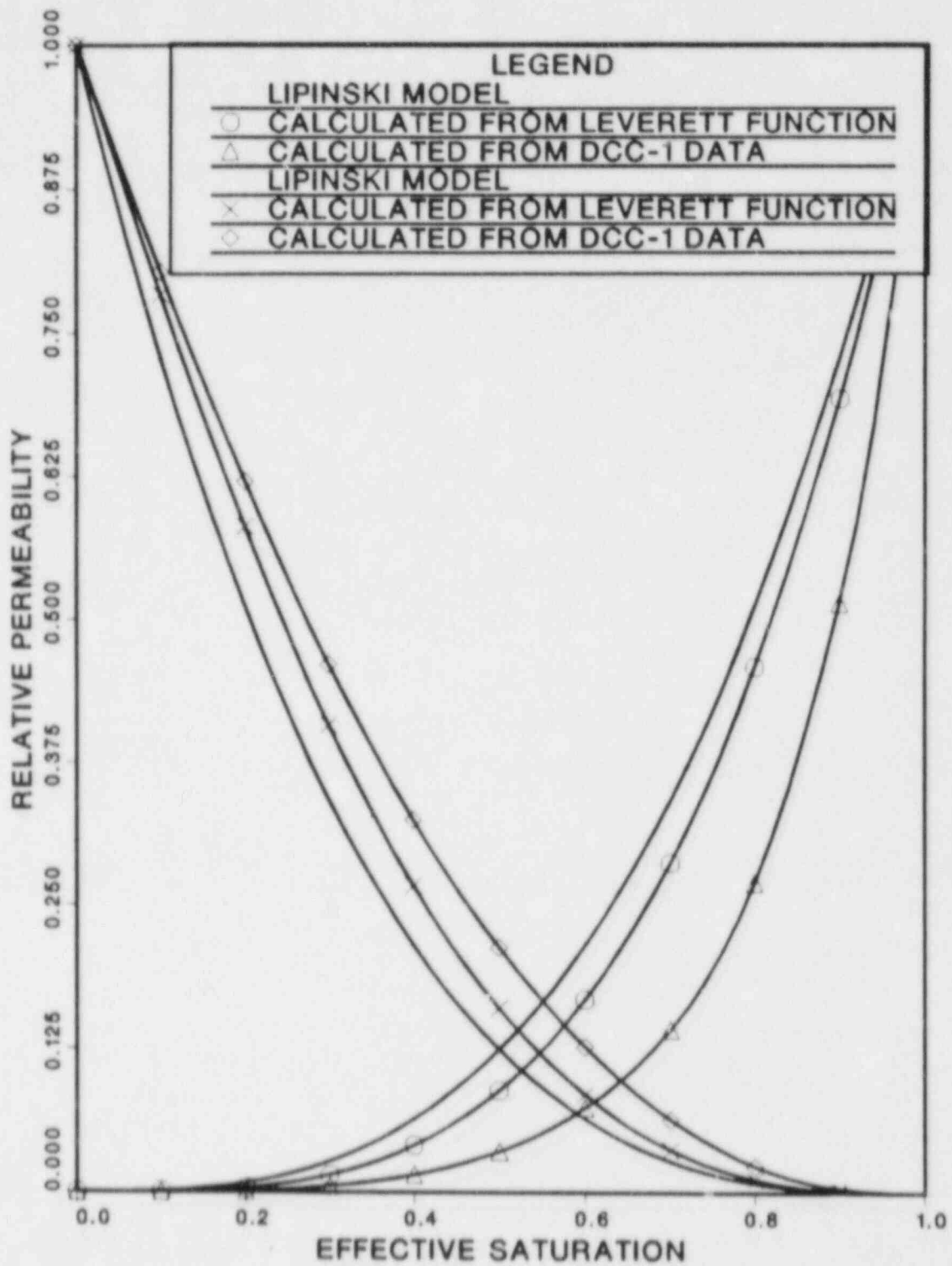


Figure 4.9 DCC-1 Laminar Relative Permeabilities

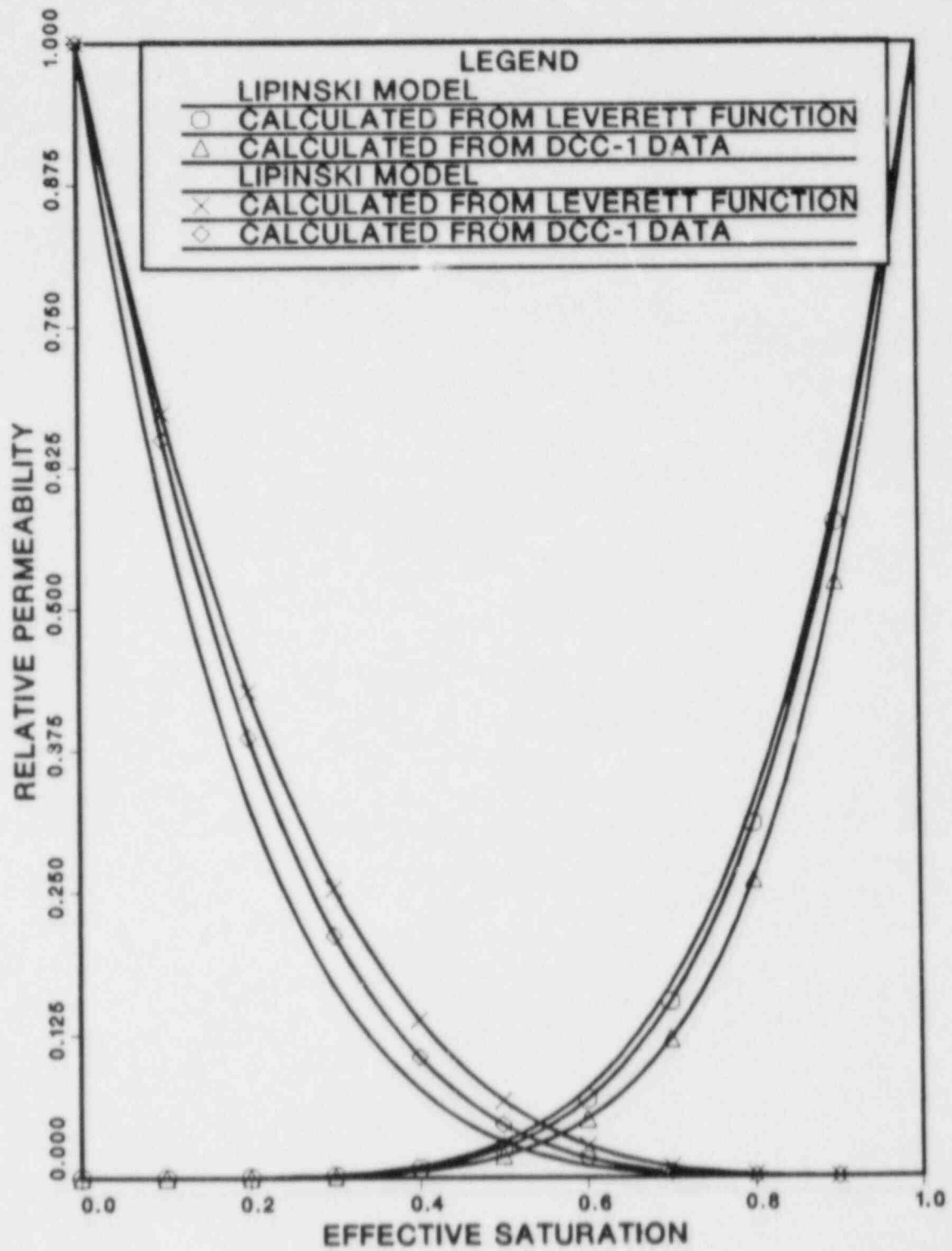


Figure 4.10 DCC-1 Turbulent Relative Permeabilities

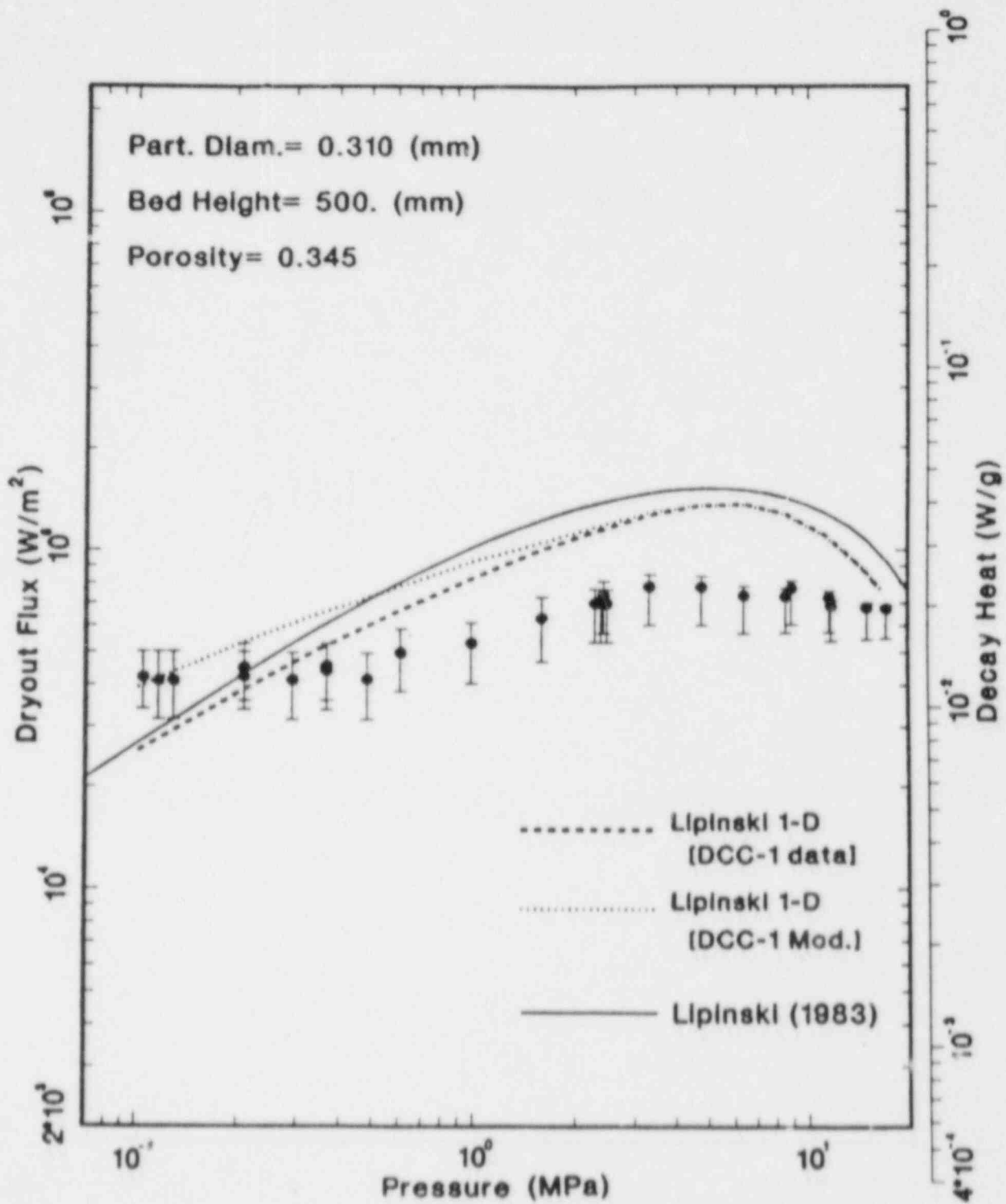


Figure 4.11 Comparison of DCC-1 Dryout Data with Modified Lipinski Model

This allowed them to carry out the integrations analytically. The capillary pressure data for DCC-1 cannot be fit by the equation form proposed by Brooks and Corey. This implies a violation of a microscopic geometric requirement for similarity, and that a correlation for the relative permeability of broad particle distributions might take on a slightly different form.

It is not the intent of this exercise to deduce a relative permeability function appropriate to DCC-1. What has been shown is that the current data base in the field of two phase porous flow suggests that a difference exists between broad and narrow size distributions. The DCC-1 data suggests that this difference results in different pressure dependencies in dryout heat flux. This does not detract from the utility of the currently used Lipinski model. At the worst, the model is off by a factor of 2.5. To the field of LWR safety, the difference is academic; under any circumstances, a DCC-1 configuration is uncoolable. It does, however, provide some concern about the impact of broad particle distributions on other bed configurations.

4.5 DCC-2 Dryout Data

Reduced dryout powers for DCC-2 are contained in Table 4.6. Figure 4.12 shows the reduced post-disruption global dryout data as a function of pressure. Plotted on the same figure is the post-disruption local dryout data. The conversion from reactor power to heat flux for local dryouts was accomplished by assuming that the saturation profile for incipient local dryout was the same as that for incipient global profile; i.e., the ratio between bed power and reactor power is the same for local and global dryouts. The error in this assumption results in at most an underprediction in the average saturation of about 30% at one atmosphere, which would result in bed powers about 15% too low. This error should decrease with increasing pressure.

The effect of local dryouts on the global dryout data is believed to be small because of the manner in which the data was obtained. Because large steps in reactor power were used to bound the global dryout power, the local dry zones did not have an opportunity to fully develop. This limited their effect on the total bed power when global dryout was achieved.

Of the models shown, the Theofanous-Saito^[10], Lipinski^[6], and Dhir-Barleon^[18] models predict the dryout levels and the pressure dependence well. The Henry^[17] and Gabor^[16] models predict the dryout levels adequately, but do not track the pressure dependence. The predictions of the Lipinski 1-D model are extremely close to those of the 0-D model, and have been omitted from the figure for the sake of

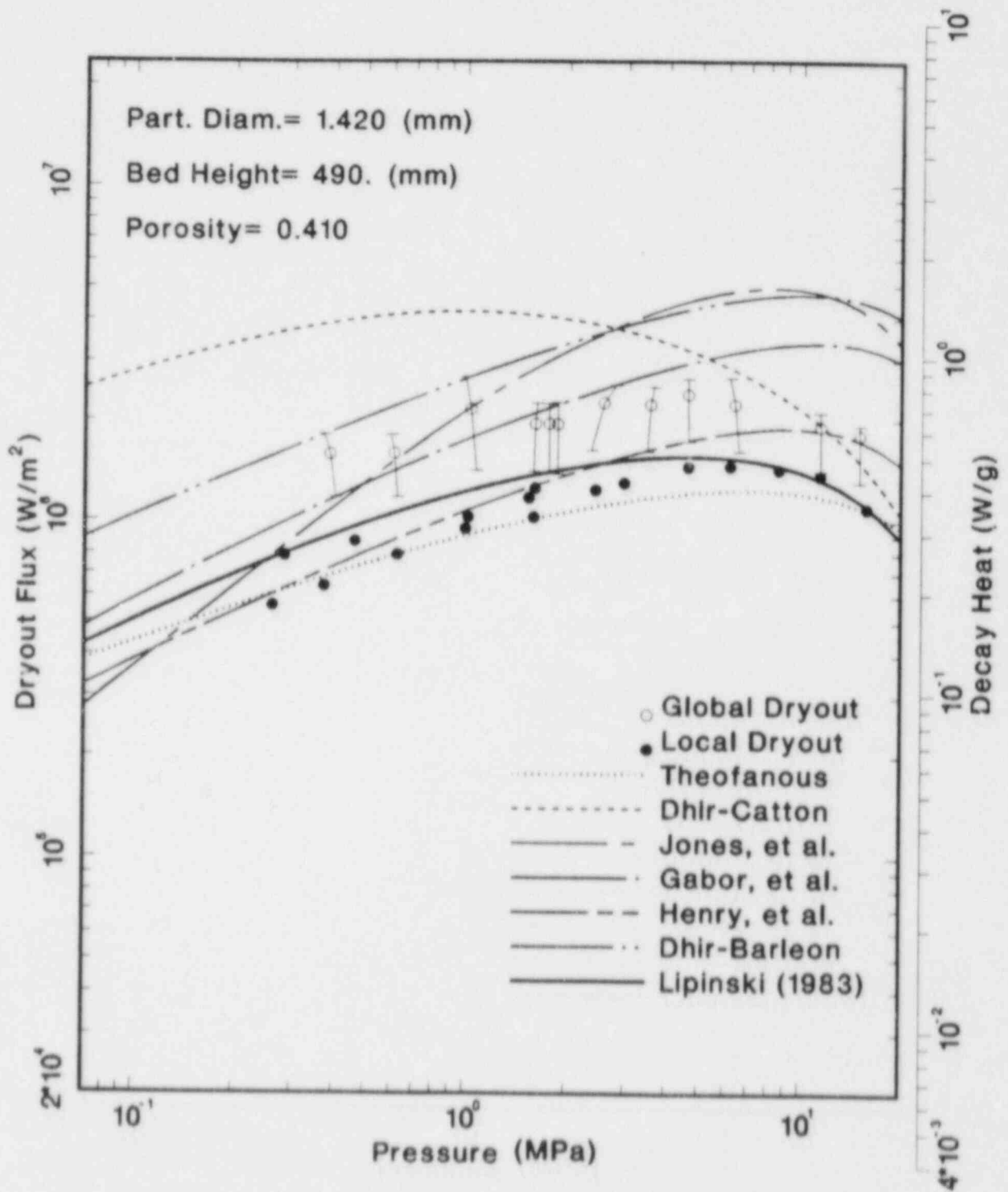


Figure 4.12 Comparison of DCC-2 Dryout Data with Predictive Models

legibility. Predictions using the Leverett correlation and the relative permeabilities derived from it (previous section) yield only very minor deviations from the currently used Lipinski models (Table 4.4), and have also been omitted.

TABLE 4.6
REDUCED DCC-2 INCIPIENT GLOBAL DRYOUT POWERS

Dryout Number	Saturation Temperature (°C)	Reactor Power (kW)	Bed Power (MW/m ²)
44	207	750-865	1.82-2.10
45	209	740-870	1.80-2.11
46/47	245/242	865-985	2.09-2.38
49/50	277/282	865-985	2.09-2.38
52/53	321	750-870	1.78-2.06
56/57	141/144	625-685	1.51-1.66
60/61	203/202	750-865	1.82-2.10
63/64	230/221	870-990	2.11-2.41
66/65	259	930-1050	2.25-2.54
67/68	343	685-815	1.66-1.97
70/58	159/160	625-685	1.52-1.66
59/73	180/184	755-1030	1.83-2.50

4.6 Error Analysis

4.6.1 Drift in Saturation Temperature

One quantity which could affect the reduction of dryout data is the drift in the saturation temperature. Control of the system pressure was accomplished by controlling the temperature of the overlying pool with an internal heater and the external coolant flow. Since this was operated manually, a small drift in the system pressure existed in the search for dryout. This drift modifies the bed power in two ways. First, the particles in the bed drift in temperature, and the corresponding change in sensible heat is

$$Q_{d,1} = -M_s C_s \dot{T} \quad (4.12)$$

Second, drift in system pressure can cause evaporation or condensation within the bed. The change in bed power that this corresponds to is

$$Q_{d,2} = \frac{-M_w h_{lv}}{s_{lv}} \left[(1 - \psi) \frac{ds_l}{dT} + \psi \frac{ds_v}{dT} \right] \quad (4.13)$$

While the amount of condensation/evaporation that occurs is dependent upon the saturation within the bed, bounds can be calculated by assuming the extremes in saturation of zero and unity.

The drift rate for each dryout in DCC-1 and DCC-2 was measured, and is shown in Tables 4.7 and 4.8. Also tabulated are the calculated effects the drifts rates have on the bed power. Comparison of the dryout powers and the drift effects show that drift in saturation temperature has little effect on the dryout data.

4.6.2 Saturation Prediction

The major component in the uncertainty of the dryout data is the saturation of the bed at the time of dryout. The magnitude of this uncertainty can be bounded by considering the extremes in saturation of zero and unity. For a uniform saturation profile, the ratio between the total bed heat flux and the reactor is

$$\frac{Q_b}{P_{\text{reactor}}} = \bar{q}(S_{\text{corr}})M_{\text{fuel}} \quad (4.14)$$

where the specific power density (Table 4.1) is adjusted for the water density

$$S_{\text{corr}} = \frac{S\rho_l(T) + (1 - S)\rho_v(T)}{\rho_l(T = 20^\circ\text{C})} \quad (4.15)$$

This correction accounts for the decrease in neutron moderation with the decrease in water density that accompanies increasing saturation temperature. The resulting ratios for saturations of 0 and 1 are then applied to the lower and upper bounds of the dryout reactor power. The results of this calculation are presented in tables 4.9 and 4.10.

TABLE 4.7
DCC-1 DRIFT RATES

Dryout Number	Drift Rate (°C/min)	Solid Correction (kW/m ²)	Water Correction (kW/m ²)	
			S=1	S=0
1	0.015	-0.198	-0.174	0
2	0.010	-0.132	-0.116	0
3	0.050	-0.662	-0.289	0
4	0.025	-0.331	-0.289	0
5	0.020	-0.267	-0.230	0
6	-0.055	0.741	0.628	-1
7	-0.090	1.223	1.019	-2
8	0.015	-0.205	-0.168	0
9	0.0	0.0	0.0	0
10	0.030	-0.417	-0.330	2
11	-0.030	0.417	0.330	-2
12	0.010	-0.140	-0.110	1
13	0.010	-0.140	-0.110	1
14	-0.050	0.708	0.551	-10
15	0.030	-0.427	-0.334	9
16	-0.030	0.430	0.343	-16
17	0.0	0.0	0.0	0
18	0.030	-0.433	-0.403	49
21	0.035	-0.474	-0.398	0
23	0.030	-0.417	-0.330	2
24	0.030	-0.427	-0.335	10
25	0.020	-0.286	-0.228	10
26	0.010	-0.144	-0.122	10
28	-0.020	0.278	0.220	-1
31	0.010	-0.132	-0.116	0
32	0.065	-0.868	-0.747	0
33	0.040	-0.539	-0.456	0
36	0.0	0.0	0.0	0
38	0.010	-0.139	-0.110	1
42	0.010	-0.135	-0.114	0
44	0.020	-0.273	-0.225	0
46	-0.010	0.139	0.110	-1
48	0.040	-0.539	-0.457	0
49	-0.065	0.903	0.716	-4

TABLE 4.8
DCC-2 POST-DISRUPTION DRIFT RATES

Dryout Number	Drift Rate (°C/min)	Solid Correction (kW/m ²)	Water Correction (kW/m ²)	
			S=1	S=0
44	0.510	-7.03	-6.71	27
44	0.880	-12.13	-11.58	47
45	0.020	-0.28	-0.26	1
45	0.600	-8.28	-7.88	34
46	0.035	-0.49	-0.46	4
47	0.295	-4.10	-3.85	32
47	0.620	-8.62	-8.08	67
49	-0.050	0.70	0.65	-11
49	-0.080	1.12	1.05	-18
50	-0.055	0.77	0.72	-13
50	-0.095	1.33	1.25	-23
53	0.020	-0.28	-0.27	12
56	-0.040	0.54	0.54	0
56	-0.760	-10.31	-10.30	10
57	-0.140	1.90	1.90	-2
57	0.620	-8.42	-8.40	9
58	-0.065	0.89	0.87	-1
58	-0.090	1.23	1.21	-2
59	0.080	-1.10	-1.07	2
59	0.355	-4.86	-4.73	11
60	0.110	-1.51	-1.45	6
60	0.275	-3.79	-3.62	14
61	-0.145	2.00	1.91	-7
61	0.130	-1.79	-1.71	
63	0.120	-1.66	-1.57	10
63	0.800	-11.09	-10.45	68
64	-0.500	6.92	6.54	-36
64	1.340	-18.53	-17.5	95
65	0.150	-2.09	-1.96	23
65	0.400	-5.58	-5.22	60
66	-0.235	3.28	3.06	-35
66	0.075	-1.05	-0.98	11.3
67	-0.500	7.09	6.83	-332
67	-1.340	19.09	19.55	-1611
68	-0.235	3.35	3.42	-279
68	-0.310	4.41	4.51	-368
70	0.0	0.0	0.0	0
70	0.980	-13.35	-13.19	20
70	1.750	-23.84	-23.56	35
71	2.380	-32.34	-32.18	38
72	-0.280	3.84	3.72	-10
72	1.670	-22.89	-22.20	57

TABLE 4.9
DCC-1 BED DRYOUT HEAT FLUX BOUNDS BASED ON S=0,1

Dryout Number	Saturation Temperature (°C)	Ratio S=0,1 (m ⁻²)	Reactor Power (kW)	Bed Power (kW/m ²)
2	101	1.950/3.423	15-16	29.2-54.8
4	107	1.950/3.416	14-16	27.3-54.7
5	122	1.950/3.416	16-17	31.2-57.8
6	141	1.951/3.376	15-17	29.3-57.4
7	160	1.953/3.351	17-19	33.2-63.7
8	180	1.956/3.322	18-20	35.2-66.5
9	202	1.961/3.287	21-24	41.2-78.9
11	222	1.968/3.252	24-25.5	47.2-82.9
12	240	1.977/3.217	27-28.5	53.4-91.7
13	261	1.988/3.171	27-28.5	53.7-90.4
14	280	2.003/3.126	25.5-27	51.1-84.4
15	300	2.025/3.069	25.5-27	51.6-82.9
16	323	2.062/2.992	24-25.5	49.5-76.3
17	342	2.108/2.908	24-25.5	50.6-74.2
18	353	2.149/2.845	24-25.5	51.6-72.5
21	151	1.953/3.364	14-16	27.3-53.8
23	220	1.968/3.255	24-25.5	47.2-83.0
24	303	2.028/3.060	27-28.5	54.8-87.2
25	322	2.060/2.995	25.5-27	52.5-80.9
26	342	2.108/2.908	24-25.5	50.6-74.2
28	224	1.970/3.248	24-25.5	47.3-82.8
30	133	1.951/3.386	14-16	27.3-54.2
31	104	1.950/3.419	14-16	27.3-54.7
32	122	1.950/3.399	15-16	29.2-54.4
33	141	1.951/3.376	16-17	31.2-57.4
36	141	1.951/3.376	15-17	29.2-57.4
38	223	1.968/3.249	25.5-27	50.2-87.7

TABLE 4.10^b
DCC-2 BED DRYOUT HEAT FLUX BOUNDS BASED ON S=0,1

Dryout Number	Saturation Temperature (°C)	Ratio S=0,1 (m ⁻²)	Reactor Power (MW)	Bed Power (MW/m ²)
44	207	1.584/2.750	.750-.865	1.19-2.38
45	209	1.584/2.749	.740-.870	1.17-2.39
46/47	245/242	1.599/2.715	.865-.985	1.38-2.67
49/50	277/282	1.624/2.659	.865-.985	2.40-2.62
52/53	321	1.683/2.576	.750-.870	1.26-2.24
56/57	141/144	1.572/2.796	.625-.685	0.98-1.92
60/61	203/202	1.582/2.754	.750-.865	1.19-2.38
63/64	230/221	1.592/2.737	.870-.990	1.39-2.71
66/65	259	1.608/2.694	.930-1.050	1.50-2.83
67/68	343	1.739/2.502	.685-.815	1.19-2.04
70/58	159/160	1.573/2.786	.625-.685	0.98-1.91
59/73	180/184	1.577/2.769	.755-1.030	1.19-2.85

While the saturation limits of 0 and 1 do produce absolute limits on the bed powers, the limits are unnecessarily wide. More reasonable limits on average saturation are 0.2 and 0.8. To use these values, one must prove that the bed power can be approximated by the product of the averages of the spatial and saturation terms, i.e., that

$$\bar{p} \frac{Q_b}{\text{reactor}} = \bar{q}(\bar{S}_{\text{corr}})M_{\text{fuel}} \quad (4.16)$$

where \bar{S}_{corr} is the average bed saturation corrected for water density. To check this, the average saturations computed by the Lipinski 1-D model were used to compute power ratios using equations 4.15 and 4.16. These power ratios are shown in tables 4.11 and 4.12 along with the power ratios computed by the 1-D model. As seen in the tables, the two ratios are close at all pressures. This indicates that the use of an average saturation in the calculation of bed powers is a reasonable approximation.

Using equation 4.16 and saturation limits of 0.2 and 0.8, error limits for the dryout data were computed. These are presented in tables 4.13 and 4.14. These are the error bounds shown in Figures 4.6, 4.11 and 4.12.

TABLE 4.11
POWER RATIOS FOR DCC-1 CONFIGURATION

Temperature (°C)	Lipinski 1-D Model		Power Ratio from Average Saturation [Equation 4.16] (m ⁻²)
	Average Saturation	Power Ratio (m ⁻²)	
100	0.433	2.71	2.72
120	0.433	2.74	2.61
140	0.433	2.77	2.60
160	0.461	2.77	2.63
180	0.447	2.78	2.59
200	0.473	2.81	2.62
220	0.507	2.83	2.65
240	0.503	2.82	2.63
260	0.559	2.82	2.67
280	0.560	2.82	2.65
300	0.609	2.80	2.68
320	0.641	2.78	2.67
340	0.647	2.75	2.64
350	0.697	2.73	2.65

TABLE 4.12
POWER RATIOS FOR DCC-2 CONFIGURATION

Temperature (°C)	Lipinski 1-D Model		Power Ratio from Average Saturation [Equation 4.16] (m ⁻²)
	Average Saturation	Power Ratio (m ⁻²)	
100	0.488	2.39	2.33
120	0.501	2.41	2.34
140	0.544	2.42	2.38
160	0.558	2.43	2.38
180	0.570	2.42	2.38
200	0.582	2.43	2.38
220	0.593	2.43	2.37
240	0.603	2.42	2.36
260	0.614	2.42	2.35
280	0.625	2.40	2.33
300	0.637	2.39	2.31
320	0.648	2.37	2.28
340	0.660	2.34	2.27
350	0.666	2.33	2.21

TABLE 4.13
DCC-1 BED DRYOUT HEAT FLUX BOUNDS BASED ON S=0.2,0.8

Dryout Number	Saturation Temperature (°C)	Ratio S=0.2, 0.8 (m ⁻²)	Reactor Power (kW)	Bed Power (kW/m ²)
2	101	2.266/3.149	15-16	34.0-50.4
4	107	2.264/3.143	14-16	31.7-50.3
5	122	2.259/3.129	16-17	36.1-53.2
6	141	2.256/3.110	15-17	33.8-52.9
7	160	2.252/3.089	17-19	38.3-58.7
8	180	2.248/3.067	18-20	40.5-61.3
9	202	2.244/3.038	21-24	47.1-72.9
11	222	2.241/3.011	24-25.5	53.8-76.8
12	240	2.240/2.984	27-28.5	60.5-85.0
13	261	2.238/2.947	27-28.5	60.4-84.0
14	280	2.240/2.913	25.5-27	57.1-78.7
15	300	2.244/2.870	25.5-27	57.2-77.5
16	323	2.256/2.804	24-25.5	54.1-71.5
17	342	2.274/2.754	24-25.5	54.6-70.2
18	353	2.293/2.710	24-25.5	55.0-69.1
21	151	2.255/3.100	14-16	31.6-49.6
23	220	2.242/3.013	24-25.5	53.8-76.8
24	303	2.245/2.863	27-28.5	60.6-81.6
25	322	2.255/2.816	25.5-27	57.5-76.0
26	342	2.274/2.754	24-25.5	54.6-70.2
28	224	2.241/3.007	24-25.5	53.8-76.7
30	133	2.258/3.119	14-16	31.6-49.9
31	104	2.265/3.145	14-16	31.7-50.3
32	122	2.260/3.129	15-16	33.9-50.1
33	141	2.256/3.110	16-17	36.1-52.9
36	141	2.256/3.110	15-17	33.8-52.9
38	223	2.240/3.008	25.5-27	57.1-81.2

TABLE 4.14
DCC-2 BED DRYOUT HEAT FLUX BOUNDS BASED ON S=0.2,0.8

Dryout Number	Saturation Temperature (°C)	Ratio S=0.2, 0.8 (m ⁻²)	Reactor Power (MW)	Bed Power (MW/m ²)
44	207	1.876/2.599	.750-.865	1.41-2.25
45	209	1.876/2.597	.740-.870	1.39-2.26
46/47	245/242	1.872/2.562	.865-.985	1.62-2.52
49/50	277/282	1.874/2.507	.865-.985	1.62-2.47
52/53	321	1.889/2.434	.750-.870	1.42-2.18
56/57	141/144	1.890/2.651	.625-.685	1.18-1.82
60/61	203/202	1.877/2.603	.750-.865	1.41-2.25
63/64	230/221	1.873/2.585	.870-.990	1.63-2.56
66/65	259	1.872/2.541	.930-1.050	1.74-2.67
67/68	343	1.910/2.374	.685-.815	1.31-2.93
70/58	159/160	1.886/2.639	.625-.685	1.18-1.81
59/73	180/184	1.882/2.620	.755-1.030	1.42-2.70

5. QUENCH BEHAVIOR

Several out-of-pile experiments have investigated the quenching of heated particulate beds. These experiments have been of two types. In the first variety, [23,24] a bed composed of large (>1 mm) particles is heated to a preset temperature. Water is then poured on the top of the bed, and allowed to percolate throughout the bed. These experiments have two common features. First, the flow pattern of the quench is two-dimensional, i.e., a uniform saturation front moving downward into the dry portion of the bed is not observed. Instead, a "finger" of liquid forms which penetrates the dry portion of the bed until it reaches the bottom. The remainder of the dry bed is saturated from the bottom. The second point is that the rate of cooling throughout this process is nearly constant in time, and is approximately equal to the dryout heat flux.

These observations do not hold for smaller particles. [25] In such beds, the quench front tends to be horizontal while progressing uniformly downward. More importantly, the bed power at which quenching will take place is less than half of the dryout power.

This dichotomy of behavior was observed in the DCC-1 and DCC-2 experiments. In DCC-1, the quench front progressed downward uniformly, corresponding with the reported small particle behavior. Rough estimates of the cooling rate were obtained from the temperature data and are presented in Table 5.1. The average bed temperatures presented represent volume averages over the entire bed, including both saturated and unsaturated sections. The average particulate heat capacity used in the calculation is 300 W/kg-K.

TABLE 5.1
DCC-1 QUENCH COOLING RATES

Dryout Number	Time		Average Bed Temperature (C)		Average Cooling Rate (kW/m ²)	Measured Dryout Heat Flux (kW/m ²)
	Start	Stop	Start	Stop		
35	19:50:02	22:00:01	224	143	9.6	44
41	15:50:00	16:29:57	551	383	64	70
42	14:22:03	15:12:00	165	140	7.7	44

Of the three extended dryouts, only number 41 has a cooling rate in the vicinity of the dryout heat flux. The other two have cooling rates a factor of 4 to 5 lower than the dryout fluxes. The calculation for DO 41 involved only a portion of the quench in which the dry bed temperatures were significantly larger than the saturation temperature. The calculation for the remaining two quenches used a much longer portion of the quench and the dry bed temperatures were much closer to the saturation temperature. This suggests that the quench cooling rate is not constant, but decreases with time. This is supported by a more careful examination of each quench.

The DCC-2 quench behavior is much different than that of DCC-1. At the initiation of quench, a liquid finger penetrated the high-permeability side and traveled to the bottom. The low-permeability region then quenched, filling both from above and below. This fingering appears to be similar to that described in the large particle tests, although the large horizontal temperature gradient present at the cessation of power could have influenced its formation.

Table 5.2 contains estimated cooling rates for two of the extended dryouts. As in DCC-1, the cooling rates are significantly lower than the dryout flux. Part of this may be due to the low permeability zone. This was always the region which was to quench.

TABLE 5.2
DCC-2 QUENCH COOLING RATES

Dryout Number	Time Start	Average Bed Temperature (°C)		Average Cooling Rate (kW/m ²)	Measured Dryout Heat Flux (kW/m ²)
		Start	Stop		
70	11:57:59	292	167	167	1600
71	12:57:58	445	160	258	1600

The calculation of average cooling rate during the quench is necessarily approximate; the limited number of thermocouples and the three dimensional nature of the temperature field cause some uncertainty in the average bed temperature. Nevertheless, the calculation is adequate for comparing quench cooling rate to dryout heat flux.

6. CONCLUSIONS

The DCC-1 and DCC-2 experiments were designed to examine LWR debris bed dryout in the laminar and transition flow regimes respectively. Each has produced data on the dependence of dryout on pressure over a wide range of pressure.

The DCC-1 experiment provided an unexpectedly low pressure dependence in the dryout data. While the measured dryout data was close to predictions, the dryout heat flux did not increase with pressure as strongly as anticipated. The measured ratio of peak dryout heat flux to the dryout flux at one atmosphere was about 1.9. The one-dimensional Lipinski model modified for varying power predicted a ratio of about 5.

The pressure anomaly in DCC-1 led to a measurement of the capillary pressure curve of the DCC-1 particle bed. This measurement demonstrated that the pore size distributed for DCC-1, as well as for other broad particle size distributions, was significantly different than that of narrow particle size distributions. This suggested that the relative permeabilities for broad distributions might be different than for narrow distributions.

The Brooks and Corey correlation was used with the measured DCC-1 capillary pressure data to calculate new relative permeabilities. When substituted into the Lipinski model, the predicted value of dryout heat flux dropped, but the pressure dependence remained about the same. The pressure dependence of the new calculation did display some sensitivity to the new permeabilities which was not formerly present. An examination of the Brooks and Corey data base suggested that the correlation may not be good for broad particle distributions. Data on the relative permeabilities for such distributions is needed before the pressure anomaly can be definitely attributed to the size distribution.

Of the available models, the Lipinski, Henry, and Hardee-Nilson models best predicted the DCC-1 data at lower pressures. At higher pressures, the Dhir-Catton, Jones, and Lipinski models have the greatest success. With the exception of the Theofanous model, none of the models predict the measured pressure dependence. Unfortunately, the Theofanous model predicts dryout heat fluxes an order of magnitude larger than those measured.

In DCC-2, "local" dryouts were observed. These are dry zones which, because they do not extend across the width of the debris bed, remain thermally stable. These zones are believed to have been caused by a local concentration of "fines" which dropped the local permeability. If such zones were to form in a debris bed during a reactor accident, sufficient temperature

might be achieved to generate hydrogen in an otherwise coolable configuration.

The DCC-2 "global" dryout data behaved as predicted both in magnitude and pressure dependence. A number of the models adequately predicted the data. The Theofanous, Lipinski, and Dhir-Barleon models predicted both magnitude and pressure dependence. The Henry and Gabor models predicted dryout fluxes adequately, but did not do as well with pressure dependence.

7. REFERENCES

1. E. S. Sowa, J. C. Hesson, R. H. Gebner, and G. T. Goldfuss, "Heat Transfer Experiments through Beds of UO_2 in Boiling Sodium," Trans. Amer. Nuc. Soc., 14, 2, 725 (November, 1971).
2. E. D. Bergeron, K. R. Boldt, R. J. Lipinski, and P. A. Kuenstler, LWR Severe Core Damage Phenomenology Program Plan, Vol. 2, LWR Degraded Core Coolability Program, SAND82-1115 (2 of 2), NUGRE/CR-2725 (2 of 2), Sandia National Laboratories, Albuquerque, NM (November, 1982).
3. G. G. Brown and Associates, Unit Operations, John Wiley and Sons, Inc., New York, (1950).
4. R. H. Brooks and A. T. Corey, "Hydraulic Properties of Porous Media," Hydrology Papers, Colorado State University, No. 3 (March, 1964).
5. R. H. Brooks and A. T. Corey, "Properties of Porous Media Affecting Fluid Flow," Journal of the Irrigation and Drainage Division, Proceedings of the ASCE, IR2, pp. 61-88 (June, 196).
6. R. J. Lipinski, A Model for Boiling and Dryout in Particle Beds, NUREG/CR-2646, SAND82-0765, Sandia National Laboratories, Albuquerque, NM (June, 1982).
7. K. D. Lathrop and F. W. Brinkley, Theory and Use of the General-Geometry TWOTRAN Program, Los Alamos Scientific Laboratory Report No. LA-4432, (April, 1970).
8. K. R. Boldt, E. D. Bergeron, P. A. Kuenstler, and T. R. Schmidt, DCC-1 Experiment Report, Sandia National Laboratories (in preparation).
9. K. R. Boldt, E. D. Bergeron, A. W. Reed, and T. R. Schmidt, DCC-2 Experiment Report, Sandia National Laboratories (in preparation).
10. T. G. Theofanous and M. Saito, "An Assessment of Class-9 (Core-Melt) Accidents for PWR Dry-Containment Systems," Nuclear Engineering and Design, 66, 301-332 (1981).
11. V. K. Dhir and I. Catton, Study of Dryout Fluxes in Bed on Inductively Heated Particles, NUREG-0252 USNRC, Los Angeles, CA (June, 1977).
12. H. C. Hardee and R. H. Nilson, "Natural Convection in Porous Media With Heat Generation," Nuclear Science and Engineering, 63, 119-132 (July, 1977).

13. J. D. Gabor, M. Epstein, S. W. Jones, and J. C. Cassulo, Status Report on Limiting Heat Fluxes in Debris Beds, NS/RAS80-21, Argonne National Laboratory, Argonne, IL (September, 1980).
14. S. W. Jones, M. Epstein, J. D. Gabor, J. C. Cassulo, and S. G. Bankoff, "Investigation of Limiting Boiling Heat Fluxes From Debris Beds," Trans. Amer. Nucl. Soc., 35, 361-363 (November, 1980).
15. J. D. Gabor and J. C. Cassulo, "Induction Heated Simulant Materials," reported by J. D. Gabor et. al., Status Report on Debris Accommodation Technology for LBRs, ANL/RAS 81-19, Argonne National Laboratory, 34-59 (May, 1981).
16. J. D. Gabor, J. C. Cassulo, S. W. Jones, and D. R. Pedersen, "Studies on Heat Removal from Fuel Debris," Trans. Amer. Nucl. Soc., 39, 642-642 (November, 1981).
17. R. E. Henry and H. K. Fauske, "Core Melt Progression and the Attainment of a Permanently Coolable State," Meeting on Light Water Reactor Safety, Sun Valley, ID (August, 1981).
18. V. K. Dhir and L. Barleon, "Dryout Heat Flux in a Bottom-Heated Porous Layer," Trans. Amer. Nucl. Soc, 38, 385-386 (June, 1981).
19. J. B. Rivard, "In-Reactor Experiments on the Cooling of Fast Reactor Debris," Nuclear Technology, 46, 344-349 (December, 1979).
20. M. C. Leverett, "Capillary Behavior in Porous Solids," Trans. AIME, 142, 152-169 (1941).
21. A. W. Reed, The Effect of Channeling on the Dryout of Heated Particulate Beds Immersed in a Liquid Pool, Ph.D. Thesis, Mass. Inst. of Technology, Cambridge, MA (February, 1982).
22. A. W. Reed, H. Meister, and D.J. Sasmor, "Measurements of Capillary Pressure in Uranium Debris Beds," Sandia National Laboratories, Albuquerque (in preparation).
23. T. Ginsberg, J. Klein, J. Kages, C. E. Schwarz, and J. C. Chen, LWR Steam Spike Phenomenology: Debris Bed Quenching Experiments, NUREG/CR-2857, BNL-NUREG-51571, Brookhaven National Laboratory, Upton, New York (June, 1982).
24. D. H. Cho, D. R. Armstrong II, and S. H. Chan, "On the Pattern of Water Penetration into a Hot Particle Bed," Nuclear Technology, 65, pp. 23-31 (April, 1984).
25. L. Barleon, K. Thomauske, and H. Werle, "Extended Dryout and Rewetting of Small-Particle Core Debris," Proceedings of the Sixth Information Exchange Meeting on Debris Coolability, November 7-9, 1984, University of California at Los Angeles.

APPENDIX

TABLE A1

TABLE A1
DCC-1 Experiment Log

Date-Time	Event	Saturation Temp (°C)	Press (MPa)	Reactor Power (kW)	Dryout* Heat Flux (W/cm ²)	Remarks
8/23 20:48	Adiabatic Heatup #1	Subcooled	~0.075	15kW	--	Maximum $\Delta T=5.2^{\circ}\text{C}$
21:31	Adiabatic Heatup #2	Subcooled	~0.075	for 100 sec	--	Maximum $\Delta T=23^{\circ}\text{C}$
23:15	Initial Bed Boiling	98	0.094	5 kW	--	All temps in bed at saturation $\pm 0.5^{\circ}\text{C}$
8/24 01:52	Dryout #1 (Incipient)	100	0.101	16 - 18	5.3 - 6.0	Subcooled Pool
03:36	Dryout #2 (Incipient)	101	0.105	15 - 16	5.0 - 5.3	Saturation Temp Increasing
04:45	Dryout #3 (Incipient)	104	0.117	10 - 15	3.3 - 5.0	Saturation Temp Increasing
06:18	Dryout #4 (Incipient)	107	0.129	14 - 16	4.7 - 5.3	
07:57	Dryout #5 (Incipient)	122	0.211	16 - 17	5.3 - 5.7	
10:16	Dryout #6 (Incipient)	141	0.372	15 - 17	5.0 - 5.7	
13:04	Dryout #7 (Incipient)	160	0.618	17 - 19	5.7 - 6.3	
15:37	Dryout #8 (Incipient)	180	1.002	18 - 20	6.0 - 6.7	

*Based on a preliminary coupling factor of 1.0 W/g/MW-ACRR.

TABLE A1
DOC-1 Experiment Log (cont'd)

Date-Time	Event	Temp (°C)	Saturation Press (MPa)	Reactor Power (kW)	Dryout* Heat Flux (W/cm ²)	Remarks
8/24 18:03	Dryout #9 (Incipient)	202	1.620	21 - 24	7.0 - 8.0	
19:57	Dryout #10 (Incipient)	222	2.408	24 - 27	8.0 - 9.0	Dryout occurred too soon after power step
20:45	Dryout #11 (Incipient)	222	2.408	24 - 25.5	8.0 - 8.5	
22:47	Dryout #12 (Incipient)	240	3.344	27 - 28.5	9.0 - 9.5	
8/25 00:22	Dryout #13 (Incipient)	261	4.765	27 - 28.5	9.0 - 9.5	
02:02	Dryout #14 (Incipient)	280	6.412	25.5 - 27	8.5 - 9.0	
04:02	Dryout #15 (Incipient)	300	8.581	25.5 - 27	8.5 - 9.0	
06:48	Dryout #16 (Incipient)	323	11.729	24 - 25.5	8.0 - 8.5	
08:58	Dryout #17 (Incipient)	342	14.956	24 - 25.5	8.0 - 8.5	
11:08	Dryout #18 (Incipient)	353	17.132	24 - 25.5	8.0 - 8.5	Bed not completely at saturation

*Based on a preliminary coupling factor of 1.0 W/g/MW-ACRR.

TABLE A1
DCC-1 Experiment Log (cont'd)

Date-Time	Event	Saturation Temp (°C)	Press (MPa)	Reactor Power (kW)	Dryout* Heat Flux (W/cm ²)	Remarks
8/25 16:00	Dryout #19 (Forced)	222	2.408	15 - 18	5.0 - 6.0	Dryout caused by pressure drop Could not reproduce Dryout #19
17:00	Stable Boiling	222	2.408	20	> 6.6	
18:39	Dryout #20 (Forced)	190	1.254	1.0	--	Dryout caused by pressure drop
20:27	Dryout #21 (Incipient)	151	0.489	14 - 16	4.7 - 5.3	
-87- 8/26 00:00	Dryout #22 (Forced)	150	0.618	15 - 18	5.0 - 6.0	Inadvertent dryout during pressure increase
03:21	Dryout #23 (Incipient)	220	2.318	24 - 25.5	8.0 - 8.5	
06:46	Dryout #24 (Incipient)	303	8.949	27 - 28.5	9.0 - 9.5	
08:47	Dryout #25 (Incipient)	322	11.575	25.5 - 27	8.5 - 9.0	
12:37	Dryout #26 (Incipient)	342	3.463	24 - 25.5	8.0 - 8.5	
13.46	Dryout #27 (Forced)	250	3.973	1.0	--	Dryout caused by pressure drop

*Based on a preliminary coupling factor of 1.0 W/g/MW-ACRR.

TABLE A1
DCC-1 Experiment Log (cont'd)

Date-Time	Event	Saturation Temp (°C)	Press (MPa)	Reactor Power (kW)	Dryout* Heat Flux (W/cm ²)	Remarks
8/26 15:33	Dryout #28 (Incipient)	224	2.500	24 - 25.5	8.0 - 8.5	Low temperature gradient across crucible wall
17:26	Dryout #29 (Forced)	150	0.476	1.0	--	Dryout caused by pressure drop
19:17	Dryout #30 (Incipient)	133	0.295	14 - 16	4.7 - 5.3	Low temperature gradient across crucible wall
8/29 10:22	Adiabatic Heatup #3	Subcooled	~0.110	50 kW for 200 sec	--	Maximum $\Delta T=30^{\circ}\text{C}$
12:03	Superheat Flash #1	Superheat	~0.110	14	--	~4°C Superheat
12:04	Stable Bed Boiling	103	0.113	14	--	2.7 psi rise in primary pressure
13:17	Dryout #31 (Incipient)	104	0.117	14 - 16	4.7 - 5.3	
15:05	Dryout #32 (Incipient)	122	0.211	15 - 16	5.0 - 5.3	
16:28	Dryout #33 (Incipient)	141	0.372	16 - 17	5.3 - 5.7	
17:22	Dryout #34 (Forced)	142	0.382	15 - 24	--	Check location of dryout at 1.5 x dryout power

*Based on a preliminary coupling factor of 1.0 W/g/MW-ACRR.

TABLE A1
DCC-1 Experiment Log (cont'd)

Date-Time	Event	Saturation Temp (°C)	Press (MPa)	Reactor Power (kW)	Dryout* Heat Flux (W/cm ²)	Remarks
8/29 18:43	Dryout #35 (Forced & Extended)	142	0.382	15 - 33	--	Location check at 2.0 x Dryout Power, extend to 330°C Maximum Temperature
8/30 10:30	Superheat Flash #2	Superheat	~0.138	10	--	~5°C Superheat
10:40	Stable Bed Boiling	109	0.139	10	--	6.5 psi total rise in primary pressure
8/30 12:22	Power Calibration	141	0.372	14	--	Calibrate bed power versus electric heater power
13:34	Dryout #36 (Incipient)	141	0.372	15 - 17	5.0 - 5.7	
14:37	Dryout #37 (Forced)	142	0.382	15 - 48	--	Location check at 3.0 dryout power, extend to 810°C Maximum Temp
8/31 08:56	Adiabatic Heatup #4	Subcooled	~2.413	100 kW for 200 sec	--	Start with bed at 80° Maximum ΔT=55°C
10:08	Adiabatic Heatup #5	Subcooled	~2.413	200 kW for 200 sec	--	Start with bed at 130° Maximum ΔT=52°C
10:37	Superheat Flash #3	Superheat	~2.413	20	--	~1°C Superheat
12:46	Dryout #38 (Incipient)	223	2.454	25.5 - 27	8.5 - 9.0	

*Based on a preliminary coupling factor of 1.0 W/g/MW-ACRR.

-68-

TABLE A1
DCC-1 Experiment Log (cont'd)

Date-Time	Event	Saturation Temp (°C)	Press (MPa)	Reactor Power (kW)	Dryout* Heat Flux (W/cm ²)	Remarks
8/31 13:26	Dryout #39 (Forced)	223	2.454	24 - 36	--	Location check at 1.4 x Dryout Power
13:56	Dryout #40 (Forced)	221	2.362	24 - 51	--	Location check at 2.0 x Dryout Power
14:24	Dryout #41 (Forced & Extended)	222	2.408	24 - 76	--	Location check at 3.0 x Dryout Power, Extended to maximum Temperature = 850°C
-06-9/1 10:32	Superheat Flash #4	Superheat	~	15	--	~3°C Superheat
10:35	Stable Boiling	116	0.175	15	--	10.8 psi total pressure rise in primary
12:13	Dryout #42 (Incipient & Extended)	141	0.372	17 - 18	5.7 - 6.0	Dryout extended to evaluate quench rate as function of power
15:36	Dryout #43 (Forced)	Subcooled	0.618	1 - 300	--	Attempt to disrupt the bed with prototypic decay power step
16:57	Dryout #44 (Incipient)	169	0.773	20 - 24	6.7 - 8.0	Check incipient dryout to see if bed changed
17:26	Dryout #45 (Forced)	Subcooled	0.869	1 - 1000	--	Attempt to disrupt the bed with prototypic decay power step

*Based on a preliminary coupling factor of 1.0 W/g/MW-ACRR.

TABLE A1
DCC-1 Experiment Log (cont'd)

Date-Time	Event	Saturation Temp (°C)	Press (MPa)	Reactor Power (kW)	Dryout* Heat Flux (W/cm ²)	Remarks
9/1 19:53	Dryout #46 (Incipient)	219	2.274	27 - 30	9.0 - 10.0	Check incipient dryout to see if bed changed
9/2 09:22	Dryout #47 (Forced)	Subcooled	0.199	1 - 1000	--	Attempt to disrupt the bed with prototype decay power step
13:12	Dryout #48 (Incipient)	140	0.361	22 - 24	7.1 - 8.0	Check incipient dryout to see if bed changed
14:32	Dryout #49 (Incipient)	221	2.362	27 - 33	9.0 - 11.0	
15:20	-----DCC-1 Experiment Terminated-----					

*Based on a preliminary coupling factor of 1.0 W/g/MW-ACRR.

TABLE A2

TABLE A2
DOC-2 Experiment Logs

Date-Time	Event	Temp (°C)	Saturation Press (MPa)	Reactor Power (kW)	Dryout* Heat Flux (W/cm ²)	Remarks
4/6 13:54	Heatup #1		Subcooled	15 for 100s		Wet Calibration
14:10	Heatup #2		Subcooled	150 for 100s		Wet Calibration
14:14	Heatup #3		Subcooled	150 for 50s		Wet Calibration
14:17	Stable Boiling	95.0	0.885	60		Subcooled Pool
15:52	Dryout #1	100.0	0.101	150 - 180	33 - 40	Local
16:46	Dryout #2	101.0	0.105	150 - 160	33 - 35	Local
19:12	Dryout #3	122.0	0.211	200 - 210	44 - 46	Local
20:26	Dryout #4	142.1	0.382	240 - 255	53 - 56	Local
21:30	Dryout #5	160.0	0.618	285 - 300	63 - 66	Local
22:11	Dryout #6	180.9	1.025	270 - 320	60 - 71	Local
23:01	Dryout #7	199.8 202.4	1.554 1.620	335 - 350 - 365	74 - 77 - 80	Local Extended Local
23:57	Dryout #8	218.8 222.4	2.274 2.408	300 - 340 400 - 455	66 - 75 88 - 100	Local Global
4/7 09:00	Package Rotated 180°					
12:23	Heatup #4		Subcooled	300 for 50s		Wet Calibration

*Based on a preliminary coupling factor of 0.746 W/g/MW-ACRR.

TABLE A2
DCC-2 Experiment Logs

Date-Time	Event	Saturation Temp (°C)	Press (MPa)	Reactor Power (kW)	Dryout* Heat Flux (W/cm ²)	Remarks
4/7 12:29	Heatup #5	Subcooled		300 for 50 s		Wet Calibration
12:56	Dryout #9	177.1	0.935	240 - 300	53 - 66	Local
13:51	Dryout #10	183.2	1.073	270 - 280	60 - 62	Local
		182.9	1.073	- 320	- 71	Extended Local
14:52	Dryout #11	198.2	1.490	150 - 290	33 - 64	Local
15:12	Dryout #12	199.2	1.522	210 - 275	46 - 61	Local
		201.1	1.587	- 335	- 74	Extended Local
17:02	Dryout #13	219.3	2.274	285 - 310	63 - 68	Local
				- 380	- 84	Extended Local
18:44	Dryout #14	221.8	2.362	150 - 380	33 - 84	Local
				- 400	- 88	Extended Local
19:56	Dryout #15	240.4	3.344	305 - 335	67 - 74	Local
				- 425	- 94	Extended Local
21:14	Dryout #16	260.3	4.688	300 - 335	66 - 74	Local
				- 365	- 80	Extended Local
22:05	Dryout #17	280.9	6.509	325 - 335	72 - 74	Local
				- 350	- 77	Extended Local
23:34	Dryout #18	301.0	8.702	330 - 350	73 - 77	Local
				- 600	- 132	Local

- 94 -

*Based on a preliminary coupling factor of 0.746 W/g/MW-ACRR.

TABLE A2
DOC-2 Experiment Logs

Date-Time	Event	Temp (°C)	Saturation Press (MPa)	Reactor Power (kW)	Dryout* Heat Flux (W/cm ²)	Remarks
4/8 07:00	Package turned back to original position					
11:25	Dryout #19	299.2	8.461	330 - 350 - 360	73 - 77 - 79	Local Extended Local
13:16	Dryout #20	323.2	11.729	400? - 455 - 550	88 - 100 - 121	Local Extended Local
15:00	Dryout #21	329.0	12.682	305 - 320	67 - 71	Local
15:38	Dryout #22	341.0	14.771	290 - 305 - 540	64 - 67 - 119	Local Extended Local
18:42	Dryout #23	341.4	14.771	290 - 310	64 - 68	Local
19:28	Dryout #24	350.4	16.513	250 - 275 - 335	55 - 61 - 74	Local Extended Local
21:32	Dryout #25	283.2	6.707	325 - 345 -390	72 - 76 -86	Local Extended Local
22:41	Dryout #26	284.6	6.909	290 - 700	64 - 154	Global
23:05	Dryout #27	283.7	6.807	280 - 595	62 - 131	Local
23:36	Dryout #28	283.6	6.807	280 - 995	62 - 219	Dry Calibration

*Based on a preliminary coupling factor of 0.746 W/g/MW-ACRR.

TABLE A2
DCC-2 Experiment Logs

Date-Time	Event	Temp (°C)	Saturation Press (MPa)	Reactor Power (kW)	Dryout* Heat Flux (W/cm ²)	Remarks
4/9 10:36	Dryout #29	Subcooled	~0.2	2000		Disruption
11:10	Stable Boiling	125.5	0.239	120		Subcooled Pool
11:50	DrouT #30	129.3 129.4	0.262 0.262	200 - 215 275 - 300	44 - 47 61 - 66	Local Global
14:25	Dryout #31			2000		Disruption
16:07	Dryout #32	129.2	0.262	210 - 225	46 - 50	Local
4/10 10:00	DrouT #33	125.5	0.232	3000		Subcooled, Disruption
10:05	Stable Boiling	125.8	0.239	190		Subcooled Pool
12:24	Dryout #34	131.8 135.4	0.287 0.313	315 - 340 - 415	69 - 75 - 92	Local Extended Local
14:42	Dryout #35	149.2	0.463	340 - 380 - 440	75 - 84 - 97	Local Extended Local
15:57	Dryout #36	159.7	0.618	260 - 375 - 510	57 - 83 - 112	Local Extended Local
17:28	Dryout #37	158.2	0.587	345 - 495	76 - 109	Local
17:47	Dryout #38	162.2	0.650	350 - 620	77 - 137	Local
18:33	Dryout #39	181.0	1.025	410 - 440	90 - 97	Local
19:29	Dryout #40	200.0	1.554	470 - 500	104 - 110	Local

*Based on a preliminary coupling factor of 0.746 W/g/MW-ACRR.

TABLE A2
DOC-2 Experiment Logs

Date-Time	Event	Saturation Temp (°C)	Saturation Press (MPa)	Reactor Power (kW)	Dryout* Heat Flux (W/cm ²)	Remarks
4/11 08:54	Dryout #41	133.0	0.295 2.9	3000		Subcooled, Disruption
10:10	Drouit #42	195.0	1.398	3000		Subcooled, Disruption
11:06	Dryout #43	202.0	1.620	500 - 535 - 595	110 - 118 - 131	Local Extended Local
12:11	Dryout #44	204.5 206.6	1.688 1.795	265 - 490 750 - 865	58 - 108 165 - 191	Local Global
12:48	Dryout #45	209.4	1.868	740 - 870	163 - 192	Global
13:38	Dryout #46	244.8	3.648	375 - 865	83 - 191	Local
13:58	Dryout #47	242.3	3.463	380 - 985	87 - 217	Global
15:02	Dryout #48	233.3	2.952	525 - 555	116 - 122	Local
16:13	Dryout #49	277.3	6.126	590 - 620 - 865	130 - 137 - 191	Local Extended Local
16:37	Dryout #50	281.5	6.607	505 - 985	111 - 217	Global
17:26	Dryout #51	300.1	8.581	590 - 615	130 - 136	Local
18:14	Dryout #52	320.9	11.424	565 - 590 - 685	125 - 130 - 151	Local Extended Local
18:56	Dryout #53	321.3	11.424	505 - 870	111 - 192	Global
19:20	Dryout #54	321.1	11.424	500 - 750	110 - 165	Local

*Based on a preliminary coupling factor of 0.746 W/g/MW-ACRR.

TABLE A2
DCC-2 Experiment Logs

Date-Time	Event	Temp (°C)	Saturation Press (MPa)	Reactor Power (kW)	Dryout* Heat Flux (W/cm ²)	Remarks
4/12 08:20	Heatup #6		Subcooled	250		Wet Calibration
08:26	Stable Boiling	138.6	0.351	250		Subcooled Pool
09:03	Dryout #55	144.2	0.404	250 - 530 - 625	55 - 117 - 138	Local Extended Local
09:59	Dryout #56	141.4	0.372	250 - 280 - 625	55 - 62 - 138	Local Extended Local
10:46	Dryout #57	144.2	0.404	255 - 685	56 - 151	Global
11:37	Dryout #58	160.5	0.618	315 - 340 340 - 685	69 - 75 75 - 151	Local Global
12:44	Dryout #59	180.2	1.002	380 - 405 - 755	84 - 89 - 167	Local Extended Local
13:37	Dryout #60	202.6	1.654	415 - 750	92 - 165	Local
14:43	Dryout #61	201.6	1.620	410 - 440 440 - 865	90 - 97 97 - 191	Local Global
15:22	Dryout #62	208.0	1.831	380 - 2050	84 - 451	Dry Calibration
17:00	Dryout #63	222.5 230.0	2.408 2.795	495 - 530 -870	109 - 117 - 192	Local Extended Local
17:32	Dryout #64	220.9	2.362	380 - 990	84 - 218	Global

*Based on a preliminary coupling factor of 0.746 W/g/MW-ACRR.

TABLE A2
DCC-2 Experiment Logs

Date-Time	Event	Temp (°C)	Saturation Press (MPa)	Reactor Power (kW)	Dryout* Heat Flux (W/cm ²)	Remarks
4/12 19:04	Dryout #65	259.0	4.613	590 - 615 615 - 1050	130 - 136 136 - 232	Local Global
19:24	Dryout #66	258.8	4.613	560 - 930	124 - 205	Local
20:30	Dryout #67	346.5 342.8	15.718 15.144	440 - 465 465 - 685	97 - 103 103 - 151	Local Extended Local
20:51	Dryout #68	342.5	14.956	385 - 815	85 - 180	Global
4/13 08:15	Liquid Convection			10		Subcooled Pool
08:18	Stable Boiling	141.5	0.372	250		Subcooled Pool
10:38	Dryout #69	142.0	0.382	250 - 560	55 - 124	Local
11:42	Dryout #70	158.3	0.587	255 - 625 625 - 990	56 - 138 138 - 218	Local Extended Global
12:44	Dryout #71	148.2	0.451	260 - 1450	57 - 320	Extended Global
14:00	Dryout #72	143.6	0.404	260 - 690	57 - 152	Global
14:40	Dryout #73	183.5	1.098	265 - 1030	58 - 227	Extended Global
15:00	-----DCC-2 Experiment Terminated-----					

*Based on a preliminary coupling factor of 0.746 W/g/MW-ACRR.

DISTRIBUTION

U. S. Government Printing Office
Receiving Branch (Attn: NRC Stock)
8610 Cherry Lane
Laurel, MD 20707
275 copies for R3

U. S. Nuclear Regulatory Commission (18)
Office of Nuclear Regulatory Research
Mail Stop 1130 SS
Washington, DC 20555
Attn: D. F. Ross
L. S. Tong
O. E. Bassett
C. N. Kelber
M. Silberberg
R. W. Wright (5)
G. Marino
R. VanHouten
J. Walker
R. T. Curtis
J. Larkins
H. Scott
M. Jankowski
L. Chan

U.S. Nuclear Regulatory Commission
Office of Nuclear Reactor Regulation
Washington, DC 20555
Attn: Z. R. Rosztoczy

U. S. Department of Energy (2)
Albuquerque Operations Office
P. O. Box 5400
Albuquerque, NM 87185
Attn: C. E. Garcia, Director, Operational Safety Division
R. Y. Lowrey, Director, Energy Technologies Division

Advisory Committee on Reactor Safeguards (4)
H Street Building
1717 H Street NW
Washington, DC 20015
Attn: W. Kerr
D. Okrent
P. Shewmon
J. Ray

Argonne National Laboratory (5)
Reactor Analysis and Safety Division
9700 South Cass Avenue
Argonne, IL 60439
Attn: L. Baker, Jr.
 J. C. Cassulo
 J. D. Gabor
 R. D. Pedersen
 E. S. Sowa

Battelle Columbus Laboratory
505 King Avenue
Columbus, OH 43201
Attn: R. Denning

Battelle Pacific Northwest Laboratories (2)
Battelle Boulevard
Richland, WA 99352
Attn: E. Courtwright
 C. Mohr

Brookhaven National Laboratory
Fast Reactor Safety
Upton, Long Island, NY 11973
Attn: R. Bari

Centre D'Etudes Nucleaires de Grenoble
85X 34041 Grenoble Cedex
France
Attn: Jean-Claude Janvier
Culham Laboratory (3)
Culham
Abingdon
Oxfordshire OX14 3DB
United Kingdom
Attn: F. Briscoe
 B. Turland
 K. Moore

EG&G Idaho, Inc. (5)
P.O. Box 1625
Idaho Falls, ID 83401
Attn: R. W. Miller
 T. M. Howe
 R. K. McCardell
 C. Allison
 M. Gasparini

Electric Power Research Institute (8)
3412 Hillview Avenue
Palo Alto, CA 94304
Attn: D. Rossin
I. Wall
E. Fuller
G. Thomas
R. Sehgal
J. Carey
D. Squarer
M. Leverett

Fauske and Associates (2)
631 Executive Drive
Willowbrook, IL 60521
Attn: M. Epstein
R. Henry

Director - IDCOR
Technology for Energy Inc.
P. O. Box 29996
10720 Dutchtown Road
Knoxville, TN 37922
Attn: M. Fontana

Japan Atomic Energy Research Institute (3)
Tokai-Muri Naka-Gun
Ibaraki-Ken 319-11
Japan
Attn: S. Katsuragi
M. Ishikawa
K. Muramatsu

Joint Research Center (7)
Ispra Establishment
21020 Ispra (Varese)
Italy
Attn: R. Klersy
H. Holtbecker
D. Schwalm
K. Mehr
P. F. Stella
H. Meister
O. Simoni

Kernforschungszentrum Karlsruhe (9)
Postfach 3640
75 Karlsruhe
Federal Republic of Germany
Attn: A. Rininsland
A. Fiege
S. Hagen
P. Hofmann
H. Werle
L. Barleon
K. Thomaske
U. Muller
G. Hofmann

Los Alamos National Laboratory (3)
P. O. Box 1663
Los Alamos, NM 87545
Attn: M. L. Stevenson
R. Henninger
J. Scott

Oak Ridge National Laboratory (3)
Oak Ridge, TN 37830
Attn: T. Kress
A. Malinauskas
R. Chapman

UKAEA (4)
Reactor Development Division
Winfrith, Dorchester
Dorset DT2 8DH
United Kingdom
Attn: R. G. Tyror
R. Potter
R. V. Macbeth
G. L. Shires

UKAEA (3)
Safety and Reliability Directorate
Rigshaw Lane
Culcheth
Warrington WA3 4NE
United Kingdom
Attn: H. J. Teague
M. Hayns
R. S. Peckover

University of California (2)
Energy and Kinetics Department
Room 5405 Bolter Hall
Los Angeles, CA 90024
Attn: I. Catton
V. K. Dhir

University of California at Santa Barbara
Chemical and Nuclear Engineering Department
Santa Barbara, CA 93107
Attn: T. Theofanous

University of New Mexico
Nuclear Engineering Department
Albuquerque, NM 87131
Attn: M. El-Gerk

University of Wisconsin
Department of Nuclear Engineering
Madison, WI 53706
Attn: M. Corradini

Westinghouse Electric Corp.
Power Systems
P. O. Box 355
Pittsburgh, PA 15230
Attn: L. Hochreiter

Westinghouse Research and Development Center
Pittsburgh, PA 15235
Attn: A. Pieczynski

1271 R. J. Lipinski
1513 R. K. Wilson
1512 G. R. Hadley
3141 S. A. Landenberger (5)
3151 W. L. Garner
6258 E. D. Gorham-Bergeron
6400 A. W. Snyder
6411 A. S. Benjamin
6412 J. W. Hickman
6415 F. E. Haskin
6420 J. V. Walker
6421 T. R. Schmidt (9)
6421 K. R. Boldt (4)
6421 P. S. Pickard
6422 D. A. Powers
6422 J. R. Gronager
6422 W. W. Tarbell
6425 W. J. Camp
6425 J. E. Kelly
6425 W. J. Camp
6425 M. Pilch
6425 A. W. Reed (8)
6427 M. Berman
6427 J. T. Hitchcock
6440 D. A. Dahlgren
6444 R. M. Summers
6450 J. A. Reuscher
8024 P. W. Dean

NRC FORM 336 (2-84) NRCM 1102, 3201, 3207 BIBLIOGRAPHIC DATA SHEET		U.S. NUCLEAR REGULATORY COMMISSION 1 REPORT NUMBER (Assigned by TADC, add Vol. No., if any) NUREG/CR-4390 SAND85-1867	
2 TITLE AND SUBTITLE DCC-1/DCC-2 DEGRADED CORE COOLABILITY ANALYSIS REPORT		3 LEAVE BLANK	
5 AUTHOR(S) A. W. Reed, K. R. Boldt, E. D. Gorham-Bergeron, R. J. Lipinski, T. R. Schmidt		4 DATE REPORT COMPLETED MONTH YEAR May 1985	
7 PERFORMING ORGANIZATION NAME AND MAILING ADDRESS (Include Zip Code) Degraded Core Coolability Studies Division 6421 Sandia National Laboratories P.O. Box 5800 Albuquerque, NM 87185		6 DATE REPORT ISSUED MONTH YEAR October 1985	
10 SPONSORING ORGANIZATION NAME AND MAILING ADDRESS (Include Zip Code) Division of Accident Evaluation Fuel Systems Research Branch Office of Nuclear Regulatory Research U.S. Nuclear Regulatory Commission Washington, DC 20555		8 PROJECT/TASK/WORK UNIT NUMBER A-1340	
12 SUPPLEMENTARY NOTES		11a TYPE OF REPORT Final Report	
13 ABSTRACT (200 words) <p>The DCC-1 and DCC-2 experiments provided the first data on dryout and quench behavior of internally heated UO₂ debris in water. The pressure range of this data extends from 1 to 170 atmospheres. Both of the experiments used the Annular Core Research Reactor (ACRR) at Sandia National Laboratories to simulate the effects of radioactive decay heating.</p> <p>The debris in DCC-1 ranged from 75 microns to 10 mm in diameter, with a mean diameter of 0.75 mm. The bed depth was 0.5 m and the porosity was 0.345. Dryout heat fluxes ranged from about 41 kW/m² (0.012 W/g) at a saturation temperature of 100°C to about 69 kW/m² (0.021 W/g) at 340°C. This measured pressure dependence is a factor of two to three lower than predicted by the analytical models. This is believed to be due to the breadth of the debris distribution, but the evidence is inconclusive. Quenches of dried debris took hours to complete. Quench fronts progressed uniformly without the liquid fingers observed in large particle tests.</p> <p>The debris distribution in DCC-2 was much narrower than in DCC 1, with the majority of particles having diameters between 0.5 and 8 mm. A small amount of "fines" was added to the mixture. In DCC-2, thermally stable local dry zones were observed at bed powers below the conventional dryout point. These are caused by the concentration of fines creating a low permeability zone. Data on global dryout, in which the bed bottom can dry out, agree well with analytical predictions. Quenches of dry zones took about 10 minutes to complete. The quench fronts were not uniform, having a liquid finger which penetrated to the bottom of the bed before the quench was complete.</p>		11b PERIOD COVERED (Inclusive dates)	
14 DOCUMENT ANALYSIS - KEYWORDS/DESCRIPTORS Debris Coolability, Light Water Reactor (LWR), Porous Flow, Pressure Dependence, Dryout Heat Flux.		15 AVAILABILITY STATEMENT NTIS GPO Sales	
6 IDENTIFIERS/OPEN ENDED TERMS		16 SECURITY CLASSIFICATION (If on page) Unclassified (If on page 11) Unclassified	
		17 NUMBER OF PAGES 114	
		18 PRICE	

120555078877 1 1A1R3
US NRC
ADM-DIV OF TIDC
POLICY & PUB MGT BR-PDR NUREG
W-501
WASHINGTON DC 20555